

Process Diagnostics of Industrial Plasma Systems

A thesis for the degree of

PHILOSOPHIAE DOCTOR

Presented to

Dublin City University

By

Niall Mac Gearailt B.Eng.

Faculty of Engineering and Computing

Dublin City University

Research supervisor:

Dr. Stephen Daniels

Declaration

I hereby certify that this material, which I now submit for assessment on the programme of study leading to the award of Doctor of Philosophy, Ph.D, is entirely my own work, that I have exercised reasonable care to ensure that the work is original, and does not to the best of my knowledge breach any law of copyright, and has not been taken from the work of others save and to the extent that such work has been cited and acknowledged within the text of my work

Signed:

A handwritten signature in blue ink, appearing to read "Chait Anand".

ID Number: 56103760

Date: 20 March 2015

Acknowledgments

Firstly I would like to express my sincerest gratitude to my PhD supervisor Dr. Stephen Daniels for his tireless support and patience and inspiring me to undertake this study in the first place.

I've also benefited greatly from my collaborations with NCPST in Dublin City University from which I have learned a great deal. Interacting with students and academia has been a huge source of inspiration and knowledge.

I would like to thank Dr. Shane Lynn and Dave Kavanagh with whom I spent many a late night running experiments on LRC 421.

I also wish to thank Dr. Eugene Tuv for introducing me to machine learning and statistics.

I'd like to thank my family, my wife Anne for generosity and patience, and finally I'd like to thank my parents for having me in first place and inspiring me to aim high in life.

Abstract

This thesis presents new techniques to investigate and understand the source of process variability in plasma etching. In a semiconductor factory thousands of wafers are processed every month in multiple chambers. While great effort is made to create reproducible process conditions, common and special cause variation remain a big challenge for the semiconductor industry. Process conditions are never identical from wafer to wafer and chamber to chamber. When high-frequency RF power, employed to create a plasma, is coupled into a chamber, the electrical characteristics of each chamber assembly is different. This electrical difference is as a result of mechanical differences of chamber components and how they are assembled. RF losses of the current affect the power deposition in the plasma and affect the process outcome. As each chamber processes more and more wafers, by-products buildup on the chamber walls impacting the process repeatability and influencing the processing chemistry. The surface roughness of the electrode and other chamber materials impact the rate at which the by-products deposit, which may also affect the process repeatability both chemically and electrically. These sources of variation contribute to inconsistent processing conditions experienced by the wafers. The work in this thesis focuses on the measurement of this process variability using intrusive and nonintrusive sensors to measure the plasma parameters as accurately as possible. Statistical approaches are used to build correlations between etch rate variability and the sensor measurements. The main finding of the thesis concludes that the combination of appropriate process measurement with sensors and

statistical algorithms provide a very powerful tool to a process engineer in diagnosing process variability.

Contents

1	Chapter 1 Introduction.....	1
1.1	Motivation.....	1
1.2	Contributions of this thesis	3
1.3	Structure of the thesis.....	4
2	Chapter 2 Industrial RF Plasma processing	6
2.1	Introduction	6
2.2	RF discharges	7
2.2.1	Plasma generation	12
2.2.2	The capacitive RF sheath	13
2.2.3	Ion Energy Distribution.....	14
2.2.4	Electron heating	16
2.2.5	Electron – Ion collisions:	17
2.2.6	Collisional Cross Sections.	18
2.2.7	The electron energy distribution function (EEDF)	20

2.3	Plasma etching	20
2.3.1	Processing requirements.....	21
2.3.2	Plasma etching fundamentals.....	22
2.3.3	Other considerations for plasma etching.....	26

3 Chapter 3 Process Equipment, Sensors and Statistics.....34

3.1	Introduction	34
3.2	Electron Cyclotron Resonance plasma sources.....	34
3.2.1	Microwave tuner controller.....	36
3.2.2	Electron cyclotron resonance.	37
3.3	Measurement techniques	40
3.3.1	Optical emission spectroscopy.....	41
3.3.2	Current voltage probes	42
3.3.3	Hairpin probe	43
3.4	Statistical analysis techniques	45
3.4.1	Summarisation of time series data	47
3.4.2	Principal Components Analysis	49
3.4.3	Gradient Boosting Trees	52

4 Chapter 4 Case Study One - Virtual metrology of a Plasma Etch Process54

4.1	Introduction	54
-----	--------------------	----

4.1.1	The etch process	55
4.1.2	Recipe structure.....	56
4.1.3	In situ plasma chamber cleaning	57
4.1.4	Sensor process measurement and data collection	58
4.1.5	Post etch metrology.....	59
4.1.6	Automated Process Control.....	60
4.1.7	The dataset	60
4.2	The analysis of time series OES spectra of a production recipe	61
4.2.1	Analysis of time series OES spectra	63
4.2.2	Approach for atomic and molecular species identification.....	67
4.2.3	Principal component analysis of time series OES spectra	72
4.2.4	Spectral clustering.....	76
4.3	Virtual metrology - etch rate estimation from sensor data.....	78
4.3.1	Data reduction and modelling approaches	79
4.3.2	Gradient boosting trees results	82
4.3.3	Analysis of the first wafer effect.....	88
4.3.4	Excursion investigation.....	95
4.3.5	Discussion and Conclusion	103

5 Chapter 5 Virtual Metrology in Production

104

5.1	Introduction	104
5.2	Architecture.....	106

5.3	Workflow design.....	109
5.3.1	Outlier detection and metrology estimation.....	109
5.3.2	Model updating	111
5.4	Results.....	112
5.5	Discussion and conclusion	117

6 Chapter 6 Electrical characterization of a capacitively coupled plasma etcher.....121

6.1	Introduction.....	121
6.2	Experimental setup.....	126
6.3	The chamber.....	127
6.4	Sensor measurements	128
6.5	Variable ground unit	128
6.6	The process.....	130
6.7	The experiment.....	131
6.8	Results.....	132
6.8.1	Etch rate, electron density	132
6.8.2	Electrical behaviour of the confined plasma mode	137
6.8.3	Discussion on confined mode	143
6.8.4	Plasma expansion to the wall	146
6.9	Conclusion	153

7 Chapter 7 Conclusion and further work..155

7.1	Virtual metrology	155
-----	-------------------------	-----

7.2	Equipment hardware diagnostics	158
7.3	Process control- Further work.....	159

Figure 2-1: Plasma potentials $V_p(t)$ (solid curves) and excitation electrode voltage $V(t)$ (dashed curves), assuming purely capacitive RF sheath behavior, for three system geometries and for DC coupled and capacitively coupled excitation electrodes.[6]..... 11

Figure 2-2: Schematic representation of the voltages in an AC coupled asymmetric RF plasma. a). Maximum RF voltage condition, b) minimum RF voltage condition. V_p is the plasma potential [3]. 14

Figure 2-3: The schematic shows the relationship between the phase in the RF cycle that the ion enters the sheath and the resultant energy gained the ion as it accelerates crossing the sheath[3]..... 16

Figure 2-4: Total inelastic (σ_{inel}) and ionization (σ_i) cross sections for electrons in nitrogen [11]..... 19

Figure 2-5: Simplified schematic of isotropic etching of silicon surface in SF₆/He discharge. 23

Figure 2-6: The four fundamental etching mechanisms. I. Physical sputtering, II. Chemical, III. Ion Enhanced, IV. Ion enhanced inhibitor [17]. 25

Figure 2-7: Cross section of 45nm transistors showing details of the different profile of the etched structures..... 26

Figure 2-8: SEM cross sections of metal etch stack with photoresist and Si₃N₄ hard marks at 20 and 90 seconds into the etch process. SEMs show the height erosion of the photoresist mask showing the need for the hardmask 27

Figure 2-9: Metal interconnects structures providing inter wiring as well as metal contacts to metal plugs connecting the metal layer below using Cl₂ and BCl₃. 29

Figure 2-10: The evolution of the metal etch process. The endpoint signal on the left RF Voltage of the 2MHz RF bias displayed on the right the corresponding cross sections of the center and edge of the wafer dense and isolated structures. (scales removed for confidentiality) 32

Figure 2-11: Effect of wafer charging due to the different behaviour of the electrons and ions at the surface of a wafer. Charging causes sputtering of the passivation at the bottom of the structure allowing lateral etching of neutrals. 33

Figure 3-1: Schematic of an industrial ECR plasma etcher with a low frequency RF bias source..... 36

Figure 3-2; Magnetron Resonator. (<http://www.cpii.com/>) 36

Figure 3-3: Plasma modeling completed by Kushner et al[35]. The simulations show the power deposition, electron temperature and density in ECR reactor. 39

Figure 3-4 VI Probe sensor inserted between the match unit and the plasma chamber. [39] 43

Figure 3-5: The mean value of RF voltage measured at the bias electrode (RMS) for 3000 wafers. Large shifts due to maintenance activity. 47

Figure 3-6: The changes in the recipe step is a function of time and the corresponding change in pressure. 48

Figure 3-7: This two-dimensional representation of principal component 1 and 2 capturing most of the variability in the data set[42]. 49

Figure 3-8: The score for each observation is the distance to the PC (a). The loading for each PC is the angle each variables is from the PC[43]. 50

Figure 3-9: Shows a simple decision tree to predict the weather (Y) from temperature(X1), humidity (X2) and dew- point(X3)[45]..... 52

Figure 4-1. Transistor Gate (scales excluded)	56
Figure 4-2: Time evolution of the profile progressing through the etch process.....	57
Figure 4-3: Schematic of ECR plasma chamber with OES sensor measuring light from a window looking down into the plasma chamber.	59
Figure 4-4 Etch rate in $\text{Å}/\text{sec}$ performance of chamber of period of 4 months in which 6000 wafers were processed and 1700 of these wafers had metrology measurements.	61
Figure 4-5: Low (Red) verse High (Blue) resolution Spectrometer displaying resolved and unresolved lines for Cl, Br and H lines.....	63
Figure 4-6 displays the spectrum at 7 seconds and the temporal behavior of 550nm	64
Figure 4-7 The graph displays the temporal behavior of chlorine. The chlorine flow controller is turned on during the plasma. The dynamic behavior of the flow controller's response is displayed.	65
Figure 4-8: The change in spectrum across step 1 of the process shown in (a) and how this can be used to determine wavelengths increasing and decreasing within the recipe step (b).....	67
Figure 4-9: 837 nm Chlorine peak red (7 sec, blue17sec) in step1 of the recipe.....	68
Figure 4-10: shows the peak structure for 656 nm and 654 nm (a) and also the time series traces for the same wavelengths in (b).....	70
Figure 4-11. Individual spectra shapes structures of Cl_2 and HBr discharges run independently.	71
Figure 4-12. High and Low spectrum resolution spectra.	71
Figure 4-13 Three principal components of Step1 Time series data. Each point represents a time point in step 1 of the process.....	73

Figure 4-14 PCA of time Series spectral data for recipe step 1. Displayed is the scores (a, d) and loadings (b, e) for the 1st and 3rd components. The loadings help identify spectral lines patterns. Si and Cl lines are shown in the (c, f).	74
Figure 4-15 displays the principal components for 25 wafers. Wafers 1 and 2 are clearly distinguished from the rest of the wafers in the lot (red)	75
Figure 4-16. Six clusters per step one of the process. Oranges the centroid with members in blue. Correlation threshold set at 0.9.....	77
Figure 4-17: Exploration of the members of the cluster involve viewing where they appear on the spectrum. In this example clustering has identified a number of distinct peaks whose behavior across the step is depicted the bottom graph.....	78
Figure 4-18: Etch rate performance in A°/sec of chamber of period of 4 months in which 6000 wafers were processed and 1700 of these wafers had metrology measurements.....	80
Figure 4-19: Output from GBT model showing the test error, the variables importance and the performance of the prediction and residuals.(a) shows the variables of most importance in the prediction, (b) predicted verse observed, (c) and (d) shows the distribution of the residuals.	83
Figure 4-20: The relationship between the etch rate and 317.35 nm.	84
Figure 4-21: 317.3nm wavelength that the GBT Model classed as correlated variable to etch rate. Upper graph shows the temporal behavior of the wavelengths. Lower graph is the mean spectra from Step 1 and 2.	86
Figure 4-22: The output of the gradient boosting tree analysis. The algorithm ranked 709.45 nm in step 2 is one of the most important variables for determining etch rate.	88

Figure 4-23: A box plots of the etch rate in $\text{Å}/\text{sec}$ for each of the wafers grouped by slot.....	89
Figure 4-24: Graph displays the etch rate $\text{Å}/\text{sec}$ variability by lot. The colours represent the slot position in the cassette.	90
Figure 4-25: The variability graphs of the 318nm (a), 777nm (b) and 827nm (c) all which show to discriminate wafer 1 from the rest of the wafers in the lot.	91
Figure 4-26: The spectra lines identified that can descriminate wafer 1 in a lot from the rest of the wafers in the lot.	92
Figure 4-27: Graph of production wafer spectra where no in-situe wafer was processed. No Cl or Br is evident in step 1 of the process.....	94
Figure 4-28: The first two principal components plotted against each other.....	96
Figure 4-29: The results from the principal component analysis displaying the scores for each wafer in the loadings for each variable in the spectrum.....	97
Figure 4-30: Graph shows the key wavelengths internsities that represent the main etch activity and the difference between the excursion wafers and the normal production wafers.....	99
Figure 4-31: The intensity of chlorine outgassing from the chamber walls as a result of various pretreatment applied to the chamber before the wafer was processed....	100
Figure 4-32: A schematic of the principle of operation of a time of flight secondary ion mass spectrometer.	101
Figure 4-33: The results from the time of flight secondary ion mass spectrometer analysis of a sample taken from the chamber walls.	102
Figure 5-1. Real-time virtual metrology service orientated architecture. The schema enables real-time data collection and analysis and decision-making.....	107

Figure 5-2: Diagram of the workflow used to detect outliers and predict metrology.
..... 112

Figure 5-3 A Multivariate T^2 approach can easily pick up the etch depth deviations from the OES data. 113

Figure 5-4: The graph shows the actual etch rate, the predicted etch rate and the error in the prediction..... 114

Figure 5-5: The graph presents the etch rate results in colour by the score. The excursion has the highest score followed by the etch rate shift up at wafer 900. 115

Figure 5-6: The pareto chart for a wafer in the excursion lot shows the wavelengths that have contributed the highest score. 117

Figure 5-7: Time series of the spectral lines identified as the highest outlier score for the excursion wafer. 117

Figure 6-1: Etch rate performance of two ECR chambers EC1 and EC2. Significant etch rate shifts can be observed after preventive maintenance cycle (2) as observed in EC1_2..... 123

Figure 6-2: The position of the microwave tuning stub1 for 4000 wafers spanning multiple maintenance cycles is displayed. 124

Figure 6-3: This figure shows the correlation between etch rate in the tuning stub position over multiple PM cycles for etch chamber 1&2 (EC1, EC2) 125

Figure 6-4: Schematic diagram of experimental apparatus. 127

Figure 6-5: The electrical characteristics of the variable ground unit are displayed as the variable vane is moved from zero position to 90° 130

Figure 6-6: Etch rate results for polysilicon and silicon nitride etch rate versus lower ground impedance changes. 132

Figure 6-7: Electron density variation with grounding impedance changes for polysilicon and silicon nitride wafers.	133
Figure 6-8: Results from the powered electrode VI probe as a function of lower ground impedance.	134
Figure 6-9: Data from the lower electrode VI probe as a function of lower ground impedance.	135
Figure 6-10: Power delivery to the plasma measured at the input to the upper electrode for a RF setpoint of 300Watts to the RF generator with lower ground impedance changes.....	136
Figure 6-11: Equivalent circuit for simplified electrical model of RF discharge. ...	138
Figure 6-12: Cross section of the RF electrodes showing grounding surfaces and leakage paths. Cpu (parasitic capacitance upper electrode) and Cpl (lower electrode) are displayed. The actual current paths are not represented in the diagram but the capacitor show to represent the total losses.	140
Figure 6-13: The VI probe measurements presenting a detailed mapping of the 0- 25 Ω lower grounding impedance (confined mode).	141
Figure 6-14: Shows the relationship between the real and imaginary impedance. The lower ground impedance is displayed as numbers above each point.	143
Figure 6-15: DC bias readings for both upper powered electrode and ground electrode as function of ground impedance changes.....	146
Figure 6-16: The current voltage characteristics of the discharge as the ground path impedance is increased from 0 to 80 Ω and the plasma expands all the way to walls.	148

Figure 6-17: The current voltage characteristics of the discharge as the ground path impedance is increased all the way to 80 Ω , the plasma expands all the way to walls for RF power changes from 200-600Watts..... 149

Figure 6-18: The current voltage characteristics of the discharge as the ground path impedance is increased all the way to 80 Ω , the plasma expands all the way to walls for pressure setting 125-600mTorr. 150

Figure 6-19: The current voltage characteristics of the discharge as the ground path impedance is increased all the way to 80 Ω the plasma expands all the way to walls for different gas mixtures. 151

Figure 6-20: The current voltage characteristics of the discharge as the ground path impedance is increased all the way to 80 Ω as the plasma expands all the way to walls for gaps changes from 4-0.85 cm. 152

Chapter 1

Introduction

1.1 Motivation

Plasma processing is widely used in the manufacture of semiconductor devices. Its application to etching and deposition has enabled great advances in the type of materials that can be deposited on the silicon wafer and the type of structures that can be etched into those materials. With the pursuit of Moore's law, the industry has driven down the critical dimensions of high-volume manufacturing silicon structures to 14nm. The over smaller dimensions present challenges to process engineers in the development of process recipes that are capable of etching 14 nm structures. Even more challenging is the ability to reproduce these dimensions in a high-volume manufacturing environment. Variation in the processing conditions from wafer to wafer, within wafer, lot to lot and chamber to chamber result in a large variation in the final dimensions of the etched features. The variation in critical dimensions (CDs) of the physical device features has a negative impact on the electrical performance of the transistor. For example, the clocking speed of the transistor is determined by the time taken to turn on and off the transistors. The physical channel length under the gate and how fast electrons can travel from the source to the drain

determine the clocking frequency. If the gate length is too large, the device speed is reduced. If the gate length is too small, the device will leak. As a result, critical dimensions tolerances in the order of +/- 0.2nm are necessary to produce high yield, high-speed devices. The challenge for the process engineer in the etch modules is to achieve on target critical dimensions with minimal variation from the target.

The motivation for this thesis was to investigate the sources of variation in the plasma processing in the area of high-volume manufacturing of semiconductors which influence the critical dimensions of silicon devices. Firstly data was collected from a plasma etcher used in production using a spectrometer over a 3 month period. This optical emission spectra (OES) was combined with etch rate measurements from the production wafers and was analysed with a number of different statistical techniques to study the etch rate variation. The source of the etch rate variation was determined and validated experimentally and with composition analysis of the deposition on the process chamber walls. Secondly an experimental capacitively coupled 13.56 MHz plasma etch chamber was modified with a variable inductor (0-80 Ω) installed on the lower electrode ground path. This modification was done to simulate the effect that routine chamber maintenance has on the electrical characteristics of the chamber hardware as well as the chamber to chamber differences seen in a semiconductor factories. The electrical parameters of the chamber/plasma combination was measured with current-voltage probes. Electron density and etch rate measurements were taken to study the impact that changing the ground path impedances had on the plasma and process performance.

1.2 Contributions of this thesis

This thesis claims the following original contributions:

1. A comprehensive process diagnostic investigation of an industrial plasma etch process was completed using optical emission spectroscopy (OES) to measure process variability. The investigation studied etch-rate variability over a 6000 wafer dataset through the analysis of OES data collected for every wafer. Various statistical modelling techniques were employed and evaluated for their suitability in estimating etch rate and also for investigating the source of the common cause process variability and special cause variability. The source of the variation determined by the statistical approach was validated both experimentally and through the material analysis of the deposition of the film on the plasma chamber walls.
2. Virtual metrology predicting etch rate was designed and implemented in a high-volume manufacturing fab. A novel workflow was developed to detect outliers and predict etch rate real-time using a gradient boosting trees algorithm. The data for each wafer process is first evaluated by an outlier detection algorithm which determines whether the wafer process is suitable for prediction or if a large excursion has occurred in the process. The model was continuously retrained when new metrology subsequently became available downstream in the process when the wafers are measured. To the best of the author's knowledge this research was the first application of multiple models predicting etch rate, in real time, using OES. The author had previously conducted internal research predicting etch rate using VI probe

data published in 2006 ISMI.

3. A patent (US 6677711 B2), granted to MacGearailt) describes how a variable ground matching unit that is used to automatically tune the electrical characteristics of the plasma apparatus to match the electrical behaviour of a fleet of chambers in a semiconductor factory. In this thesis an in-depth study is completed on how changing the electrical characteristics of the chamber can affect the plasma process. A variable inductor grounding match unit is designed and built which includes the ability to control the variable inductor in real time with feedback of the position of the tuning vane. VI probe, OES, electron density, and etch rate wafers are used to characterize the process under various ground impedances.

1.3 Structure of the thesis

The thesis is structured as follows. Chapter 2 gives an introduction to the fundamentals of industrial RF plasmas and the principals of plasma etching, chemistry and processing. Chapter 3 describes electron cyclotron resonance plasma systems and gives details of the measurement techniques used in the thesis as well as the statistical approaches and algorithms. Chapter 4 gives details on the process diagnostics completed on the data set from the high-volume manufacturing etch process. Statistical techniques are employed to determine the source of the variation observed in the etch rate using an OES sensor. Chapter 5 describes the development and deployment of real time etch rate prediction in a factory environment and the design of the workflow for the self-learning prediction algorithms. Chapter 6 details

the work on characterizing the electrical behaviour of the plasma process with varying ground impedance. Chapter 7, conclusions are drawn and further work proposed.

Chapter 2

Industrial RF Plasma processing

2.1 Introduction

RF plasmas have been widely adopted in semiconductor manufacturing due to their ability to create and control the complex plasma chemistry which is used to manipulate and modify surface properties of silicon wafers. This chapter examines the basic principles of plasmas and gives a background to the etching mechanisms used in industrial plasma processing tools.

The term plasma, coined by Irving Langmuir [1], is used to describe quasi-neutral gas containing equal numbers of positive and negatively charged particles. As a substance is heated to a sufficiently high temperature, the molecules in the gas decompose into atoms. As the temperature is further increased, the atoms ionize into freely moving charged particles as the gas transitions into a plasma state. The temperature required to form plasma is many thousands of kelvin. Direct heating on the gas is not a viable option and heating is typically done by electrical means or by electromagnetic wave as described in chapter 3.

Industrial plasma processing equipment primarily deal with weakly ionized plasma discharges which are driven by a radio frequency (RF) power supply that drives

current through a low-pressure gas. This applied power preferentially heats the mobile electrons relative to the heavy ions. The degree of ionization in a low pressure plasma is less than 10^{-4} leaving the gas consisting of mostly neutrals. As a result, the gas temperature remains very low (effectively room temperature) and high energy electrons, typically 1-20 eV, can be employed to dissociate the gases into chemically reactive radicals which can react with the surface of the wafers. The low gas temperature processing environment provides a controlled environment for low damage processing applications. For example, plasmas facilitate the use of photoresist as a mask in etch processes enabling accurate pattern transfer. Plasmas contain positive ions which can be accelerated through a potential gradient and impinge on the wafer surface enhancing the chemical reactions. The ability to control the ion flux and energy distribution as well as the creation of radicals, has revolutionized the ability of plasma process to etch nano scale features in wafers.

2.2 RF discharges

Industrial capacitively coupled RF plasma reactors are parallel plate systems driven at 13.56 MHz power supply. One electrode is grounded while the other is powered by the RF generator, delivering power through a matching network to the electrode. The wafer is placed on the lower electrode where it can be mechanically or electrostatically clamped. Helium backside cooling is delivered to the rear of the wafer to facilitate heat transfer to the water cooled electrode. The gap between the electrodes can be varied on some tool designs and controlled in the process recipe. Furthermore, the RF power delivery can be swapped between the upper and lower

electrodes. Delivering the power to the lower electrode will allow significant increase in ion bombardment to the wafer surface as a result of the large potential difference between the plasma and the powered electrode. This configuration is used in the etching of silicon nitride or silicon oxide which has high bond energies and energetic ion bombardment is required to break these bonds and allow chemical etching to occur.

In plasma processing reactors a wafer is normally placed on one of the electrodes. In the case where the wafer surface is a dielectric, it will inhibit the flow of current in the DC discharge resulting in the quenching of the plasma. In an RF discharge no net current is required to sustain a discharge, making it suitable for plasma processing of a wide range of materials including dielectric substrates.

In capacitively coupled RF systems the power is delivered from the generator through a matching network to the electrodes. A matching network provides a $50\ \Omega$ resistive load to the generator, facilitating maximum power transfer from the generator. The matching network also provides a variable inductance to resonance with the variable capacitance of the plasma chamber. The parallel plate configuration involves one electrode delivering RF power with the other grounded. Depending on the application for plasma processing, the RF power may be coupled through the wafer electrode or the upper electrode. In some designs the user can choose which electrode to deliver the power to in the process recipe configuration. The ratio between the area of the powered electrode and the grounding surfaces (ground electrode and chamber walls) and is shown in Figure 2-12[2] is a very

important factor for plasma processing tools as it impacts the ion energy distribution that bombard a wafer on an electrode. Two of factors that impact the energy of the ions are the plasma potential and any DC bias component of the plasma potential that develops. The capacitively coupled asymmetrical configuration that is the most widely used is displayed on the top right of Figure 2-1. The DC component of the plasma potential in this configuration is established due to the high electron mobility relative to the ions. The capacitor between RF generator and the powered electrode results in no net current flow and as result the plasma potential must approach the powered electrode potential for a brief period in the RF cycle to allow electrons to reach the powered electrode. Similarly the plasma potential must approach zero for a brief period in each cycle to balance the electrons that left the plasma reaching the power electrode. The plasma potential is always higher than the instantaneous electrode potential and is modulated by the RF power supply and the electrode and sheath potentials (see Figure 2-2)[3]. When the electrode areas are symmetrical no self-bias will be generated as the plasma potential will adjust itself so that there total net current is zero. Similarly when the powered electrode is larger than the grounding electrode a positive DC develops on the capacitively coupled configuration to keep the net current to zero.

In the work carried out in this thesis in Chapter 6, the power is delivered to the upper electrode whose area is 12% larger than the lower electrode which is grounded and upon which the 200 mm wafer is positioned. The chamber walls are somewhat protected by ceramics reducing the effective ground surface area, but none the less a significant area of the chamber wall is exposed giving the chamber an asymmetric

electrode configuration. This particular design is used to improve the uniformity of the etch process across the wafer. In particular, to achieve uniform processing in a commercial reactor, uniform ion bombardment as well as uniform neutral radicals fluxes need to be presented to the wafer surface. Careful consideration is paid in the design of the gas delivery to ensure uniform diffusion across the wafer surface, as well as the removal of the by-products. The gas is delivered through a hole in the centre of the upper electrode and then diffused through a series of baffle plates.

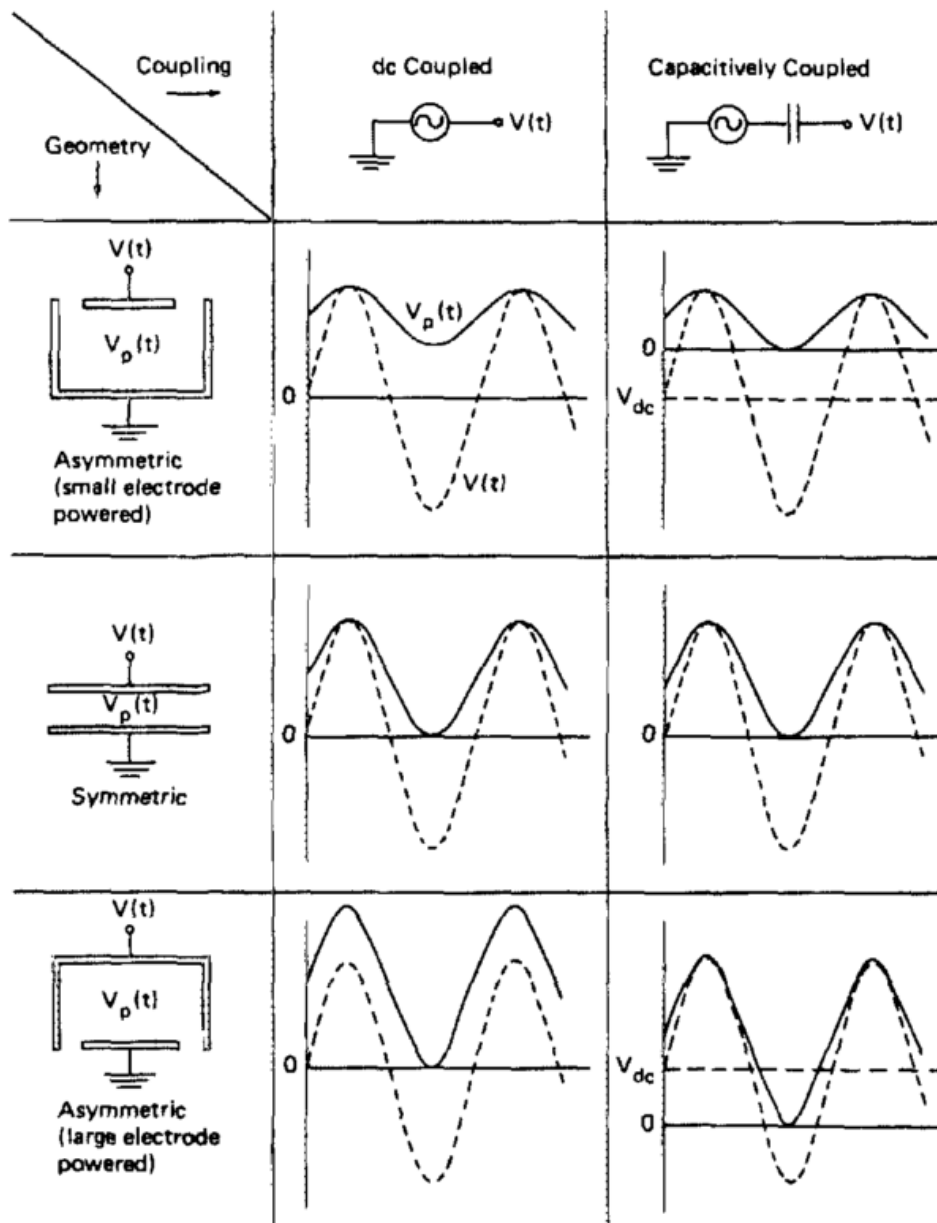


Figure 2-1: Plasma potentials $V_p(t)$ (solid curves) and excitation electrode voltage $V(t)$ (dashed curves), assuming purely capacitive RF sheath behavior, for three system geometries and for DC coupled and capacitively coupled excitation electrodes.[6]

2.2.1 Plasma generation

The electric field between the electrodes accelerates the free electrons which then collide with neutrals causing ionization creating additional electrons. Due to their high mobility the electrons are lost to the walls and to the grounded electrode charging them negatively relative to the plasma, and repelling additional electrons and stopping them from leaving the plasma. This results in an electric field between chamber surfaces and the plasma creating a sheath. As in the DC discharge, ions are accelerated by the negative potential relative to the plasma potential. This sheath edge is not static but oscillates back and forth with the sinusoidal driving voltage of the RF generator.

In commercial RF systems, a blocking capacitor is placed between the RF matching network and the powered electrode. This serves to allow the powered electrode to develop a self-DC bias which will increase the energy of the ions bombarding the electrode surface, thus enhancing the etch rate if the wafer is placed on the powered electrode. A DC bias can also develop on the wafer placed on the grounded electrode due to the fact that the wafer is often a dielectric and will appear as a blocking capacitor to the DC current. Similar to DC glow discharge, the self-bias that develops on the powered electrode acts to balance the difference in mobility between the electrons and the ions. However, since the RF systems has an oscillating electric field, the sheath potential is also modulated.

2.2.2 The capacitive RF sheath

The ion and electron plasma frequencies are given by [4]:

$$\omega_{pi} = \left(\frac{e^2 n_i}{\epsilon_0 m_i} \right)^{\frac{1}{2}} \quad 2.1$$

$$\omega_{pe} = \left(\frac{e^2 n_e}{\epsilon_0 m_e} \right)^{\frac{1}{2}} \quad 2.2$$

where n_i and n_e are the ion and electron densities and m_i and m_e are the masses of the ions and electrons respectively and ϵ_0 is the permittivity of vacuum. For normal plasma conditions where $n_i = n_e$ the ion and electron plasma frequency are in the order of 3 MHz and 300 MHz respectively. The electrons respond almost instantaneously to the oscillating electric field in the sheath, whereas the ions respond to the time averaged fields.

In Figure 2-2 is a schematic representation of the voltage experienced as a function of sinusoidal RF voltage is displayed. The sheath width expands and contracts on both electrodes within the RF cycle. The plasma potential also oscillates.

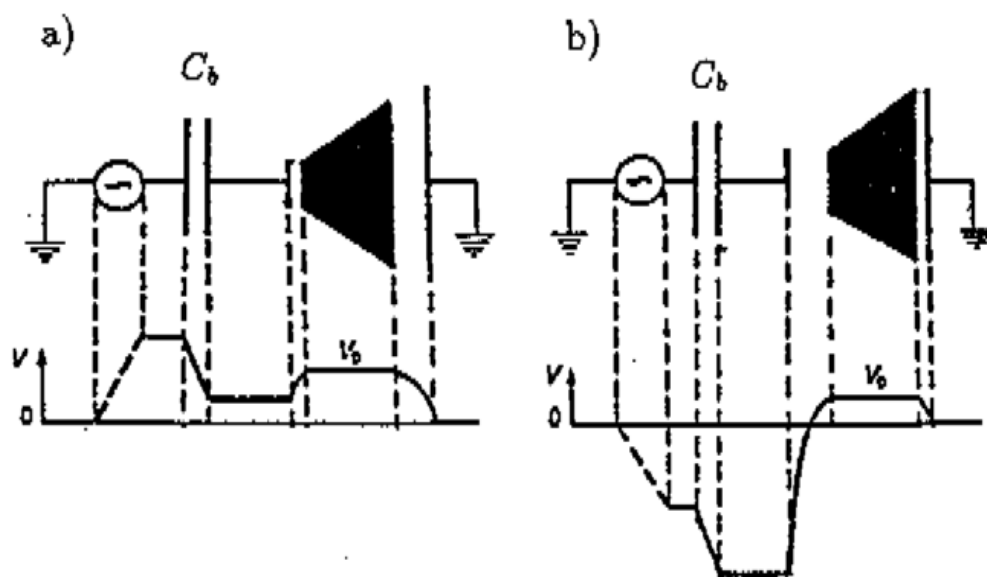


Figure 2-2: Schematic representation of the voltages in an AC coupled asymmetric RF plasma. a). Maximum RF voltage condition, b) minimum RF voltage condition. V_p is the plasma potential [3].

The electron density in the RF sheath changes with the instantaneous voltage. Electrons move in and out of the sheath region when the sheath momentarily collapses as the electrode potential approaches the plasma potential, V_p , allowing electrons to escape and balance the ion current.

2.2.3 Ion Energy Distribution

The energy with which ions impinge on the wafer surface is a critical parameter in any plasma process. In particular, ion bombardment plays a critical role in reactive ion etching. The ion transit time to cross the sheath is given by [5]:

$$\tau_i = 3\bar{s}\sqrt{m_i/2e\bar{V}_s} \quad 2.3$$

where \bar{s} is the time average sheath width, m_i is the ion mass and \bar{V}_s is the dc sheath potential. For a low frequency of 400 KHz, used in the bias of the ECR discharge discussed later in this chapter, $\tau_i/\tau_{rf} \ll 1$ the ions cross the sheath only during a small fraction of the RF cycle. As the sheath oscillates back and forth with the RF cycle, the energy the ion gains is strongly dependent on the phase of the RF cycle that it enters the sheath at as illustrated by Figure 2-3. This results in a broad bimodal distribution of the ion energies, where the minimum and maximum ion energies correspond to the minimum and maximum sheath voltages. For example a frequency of 13.56 MHz has $\tau_i/\tau_{rf} \gg 1$, and the ions take many RF cycles to transit the sheath and are not influenced by the instantaneous sheath voltage. The ion energy is influenced more by the time averaged voltage and therefore not as dependent on the phase with which the ions enter the sheath. The ion energy distribution for these higher RF frequencies is not bimodal.

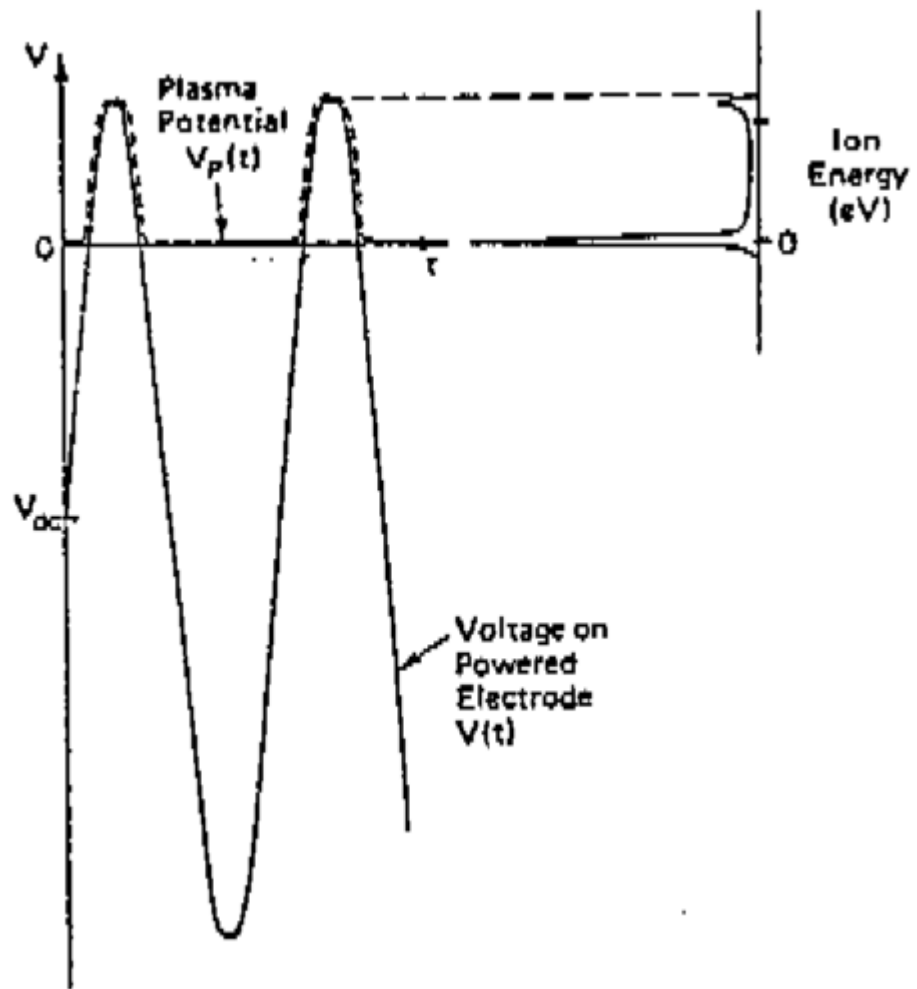


Figure 2-3: The schematic shows the relationship between the phase in the RF cycle that the ion enters the sheath and the resultant energy gained the ion as it accelerates crossing the sheath[3].

2.2.4 Electron heating

There are two main mechanisms for heating electrons in RF capacitively coupled discharges: ohmic (collisional) and stochastic heating. Plasma resistivity due to

electron-neutral collisions leads to ohmic heating while momentum transfer from high voltage moving sheaths leads to stochastic heating. Thus, ohmic heating is mainly a bulk phenomenon while stochastic heating is localized in the sheath regions.[6]

In the higher pressure regimes (100-500 mTorr) of capacitively coupled RF discharges studied in this thesis, ohmic heating is the predominant mechanism for the transfer of energy to the electrons. The energy is gained by an electron in the oscillating electric field and is transferred into a direction perpendicular to the field and it is not lost during the reversal of the electric field[7][8]. In this pressure regime, secondary electron emission may still occur with the majority of electrons traversing the sheath without collisional ionization and penetrating the bulk plasma with energies above the ionization threshold. The surf riding mechanism of the oscillating sheath edge can also heat electrons. During the second half of the RF cycle the sheath spatially extends back into the bulk, accelerating electrons into the plasma [9][10].

2.2.5 Electron – Ion collisions:

In this section some of the basic processes involving electrons and ions are reviewed to give an understanding of the basic mechanisms. It is by no means an exhaustive review of the complex interactions that occur in the discharge, but is mainly focused on those processes which are most important to plasma processing.

Collisional processes can be divided into elastic and inelastic collisions. An elastic collision is one in which kinetic energy is conserved. In the collision between an electron and an atom the difference in mass is such that the energy transfer is

negligible and the electron just changes direction. If the electron is moving in an electric field the collision just serves to restrict the velocity in direction of the field. If the electron energy is above the ionization threshold, the impinging electron may remove an electron from the atom resulting in an ion and two electrons.

The three primary electron loss mechanisms are recombination, attachment and diffusion. Electron attachment is a significant loss mechanism in the electronegative gas regimes (O, Cl, F, Br) used in plasma processing, where electrons are lost in the creation of negative ions. The electronegative gases have a quenching effect and a significant impact on the resultant plasma properties, specifically the electron energy distribution function (EEDF) and plasma emissions observed in optical emission spectroscopy.

2.2.6 Collisional Cross Sections.

The concept of mean free path refers to the average distance travelled by a particle between two successive collisions. In kinetic theory the mean free path of particles is considered to have a Maxwellian distribution of velocities. This is more conventionally reserved for elastic collisions between thermal molecules [11].

The collisional process between electrons and other particles needs to consider how the particle presents itself to an approaching electron. The effective collisional cross section of a gaseous atom or molecule and an electron can be defined in terms of the probability of an interaction between the particles. The interaction between the

approaching electron and the particle is strongly dependent on the electrostatic forces on the relative velocity of the approaching electron and the particle. There is a certain element of probability and uncertainty about the interaction that can occur in the collision. This probability is represented as the collisional cross-section of the particle. Each of different collisional processes has a different probability of occurring and is strongly dependant on the velocity of the approaching electron. Figure 2-4 gives the cross sections for argon which is commonly used in plasma processes. Low energy electrons have a higher probability of elastic collisions, while the higher energy electrons can penetrate the atomic cloud.

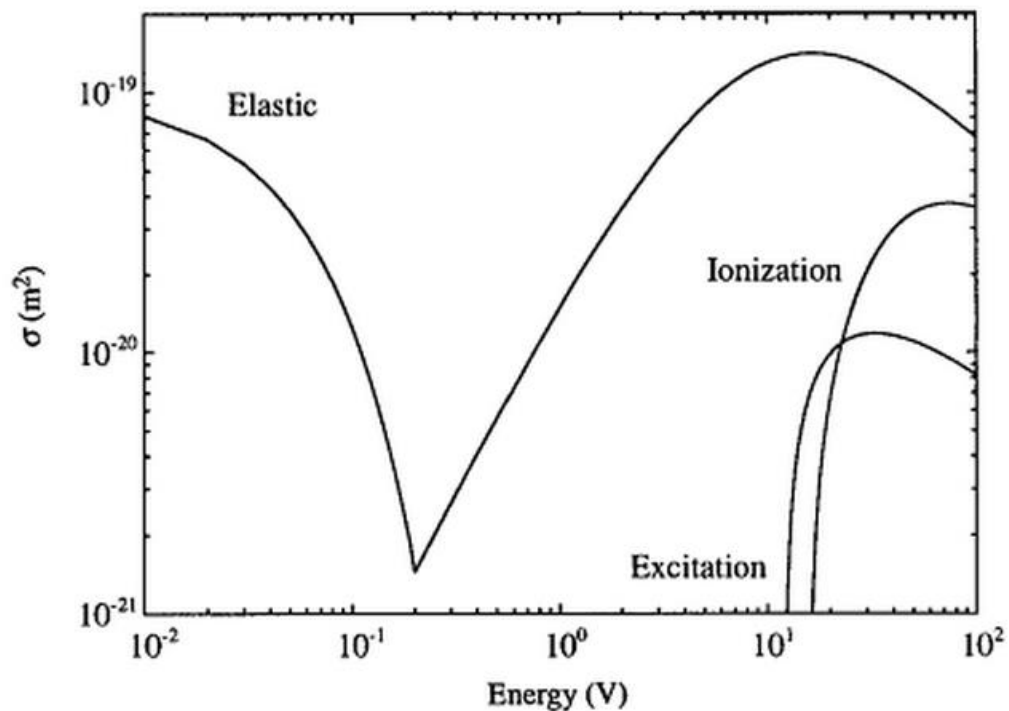


Figure 2-4: Ionization, excitation and elastic scattering cross sections for electrons in an Argon gas [12].

2.2.7 The electron energy distribution function (EEDF)

The Maxwell Boltzmann distribution applies to an assembly of particles that are in thermal equilibrium. Electrons in a plasma discharge are not in a state of equilibrium. Slow electrons make elastic collisions while electrons with energies above excitation and ionization thresholds are involved in inelastic collisions [11]. Many studies have been completed to determine the EEDF for a variety of processing conditions[13]. The addition of electronegative gas species to the discharge can also affect the EEDF. Many studies have measured a hot tail in the distribution which is responsible for much of the ionization[14][15].

2.3 Plasma etching

Plasma etching's popularity in the manufacturing of semiconductor devices has grown greatly since the 1960s. As an alternative to wet chemical processing, plasma etching has a number of advantages. In addition to the environmental benefits of moving away from chemical baths, in which batches of wafers would be processed together, plasma etching offers a cleaner, more efficient and controllable environment for removing material from the surface of silicon wafers. With the reduction in dimensions of semiconductor devices, plasma etching offers the only commercially viable solution. High-volume manufacturing of 14 nm devices would be impossible without plasma processing. Plasma etching provides anisotropic etching with a very high degree of control and the ability to selectively etch one material in preference to another.

2.3.1 Processing requirements

The challenge for process engineers is to develop a process capable of etching submicron features, meeting all the dimensional tolerances of the feature size, while maintaining a high degree of repeatability. The challenges for plasma etching are:

1. The etch rate of the process must be as fast as possible in order to maximize the throughput of the plasma etch tool.
2. Critical dimensions of the feature must be achieved.
3. The process uniformity from the centre to the edge of the wafer must be maximised.
4. The process uniformity for dense and isolated structures must be the same.
5. The process must be able to selectively etch the bulk material over the mask or an underlying layer such as silicon oxide underneath the polysilicon gate.
6. The amount of deposition of by-products on the chamber walls must be minimized to prevent flaking and causing defects. This will lead to low meantime between chamber cleans which affects costs and productivity.
7. The process variability from wafer to wafer and from lot to lot must be minimized.
8. The process must be tolerant to the different product mixes and recipe mixes processed in the same chamber.
9. Wafer charging damage must be minimized.

The development of robust manufacturable processes are still largely an empirical effort involving a great deal of design of experiment in order to arrive at the best

compromise for process performance. The process must be evaluated as to how repeatable it will be at processing wafers across multiple chambers in a high-volume manufacturing fab. The commercial pressures to develop new process technology does not afford the opportunity to continuously refine and develop the robustness of the process. There is also large risk involved with changing processes once they have ramped up to high-volume. One of the approaches taken in increasing yields and productivity has been to use process diagnostics to investigate the source of process variation. If the cause of process variation can be established, the appropriate control strategies can then be implemented to mitigate the process drift.

2.3.2 Plasma etching fundamentals

The objective of industrial plasma process is to provide a consistent uniform flux of etchants species, and in some cases ions, to produce repeatable reactions on the wafer surface.

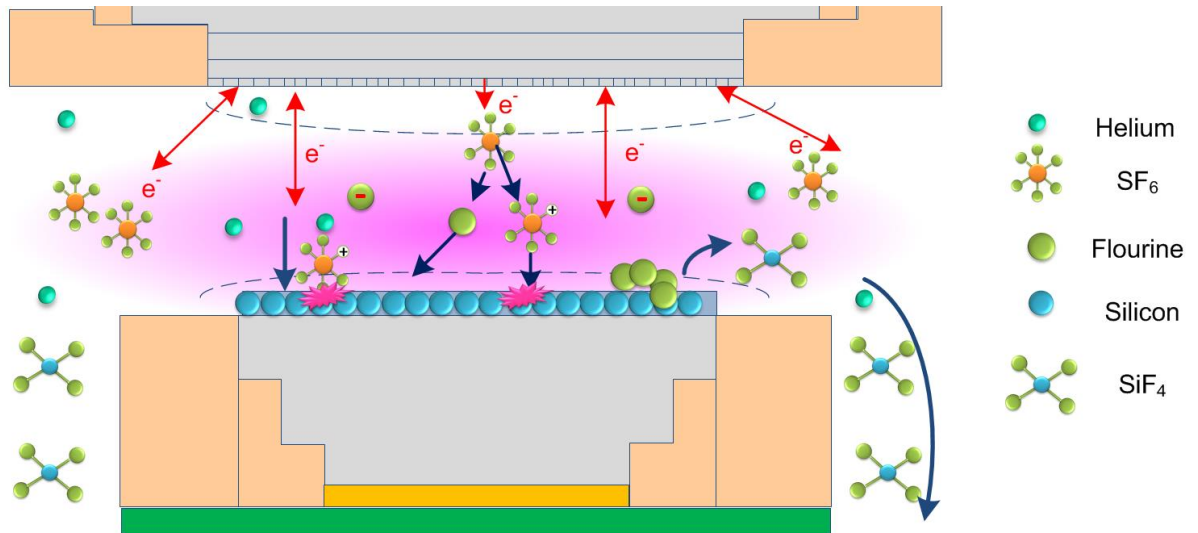


Figure 2-5: Simplified schematic of isotropic etching of silicon surface in SF₆/He discharge.

The process can be divided into some basic steps as shown in Figure 2-5.

1. Firstly, radicals and ions are produced from feedstock gasses. This process is governed by the electron collisional processes. The electron density and temperature and ultimately the electron collisional rate [16] are the important parameters that determine the density of ions and radicals.
2. The transportation of the reactive radicals from the plasma bulk to the surface of the wafer is through a diffusion process. The size of the chamber, gas flow rates and pressure setpoint also determines whether the radical will have a collision before making it to the wafer surface. The chamber is designed with a shower head and baffle plate configurations to facilitate the delivery of the feed gases in such a way as to compensate for the greater

loading/consumption of radicals in the centre of the wafer compared with the edge [17].

3. The flux of ions directed towards the wafer surface will enhance the reaction of the neutral radicals with the wafer surface. The ions provide energy that break the bonds of the substrate material creating an active etching site. In addition, any polymerization or passivation film that develops on the wafer surface will also be sputtered off the horizontal surfaces by the ion flux.
4. The reactive species (fluorine radicals for example) are absorbed onto the surface and react chemically. In the case of fluorine etching silicon, atomic fluorine penetrates approximately five monolayers into the bulk, resulting in a volatile by-product (SiF_4) or its precursors (SiF , SiF_2 , SiF_3) [18][10][19].
5. The volatile by-products need to be de-absorbed from the surface of the wafer and are pumped out the chamber. This process is assisted by ensuring low residence time in high flow process conditions.

The mechanism of etching three dimensional features involves some additional complexity. In Figure 2-6 the basic etch mechanisms are shown. In order to achieve a vertical profile, sidewall passivation is required to prevent neutral radicals from etching the feature horizontally. The process chemistry and plasma parameters are deliberately tuned so as to produce the right amount of passivation of the side wall to balance the vertical etching. Too much passivation and the profile will taper. Too little and it will bow.

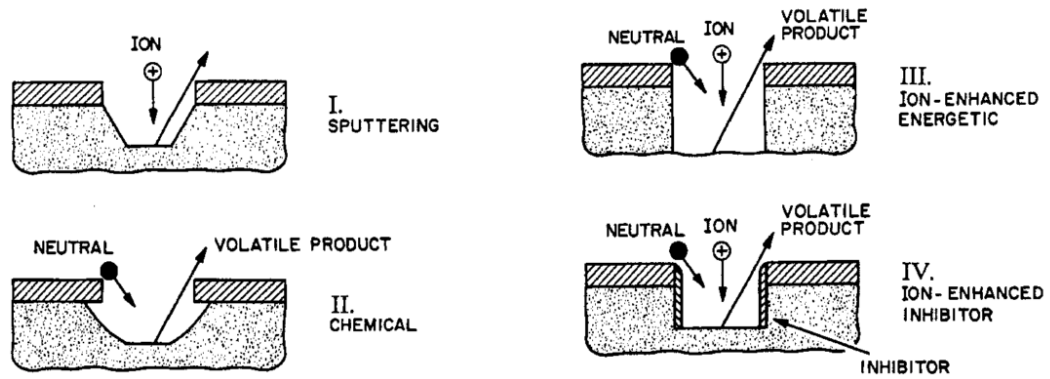


Figure 2-6: The four fundamental etching mechanisms. I. Physical sputtering, II. Chemical, III. Ion Enhanced, IV. Ion enhanced inhibitor [18].

This carefully engineered balance of vertical etching and lateral passivation determines the profile of the etched structure. Figure 2-7 shows the cross section of the transistors and first metal interconnects of a 45nm semiconductor device. While 90° profiles are desired in the etching of the gate features, other structures demand tapered profiles. For example, silicon germanium is used on either side of the channel under the gate to stress the silicon lattice to improve electron mobility and increase the clocking speed of the device. To achieve this two trenches are etched on either side of the gate which are subsequently filled with silicon germanium. The shape of this trench, both its depth and undercut latterly, underneath the transistor gate are extremely critical in determining the performance of the device. In etching this type of trench, precise control is needed and the chemistry must be tuned to achieve these dimensions.

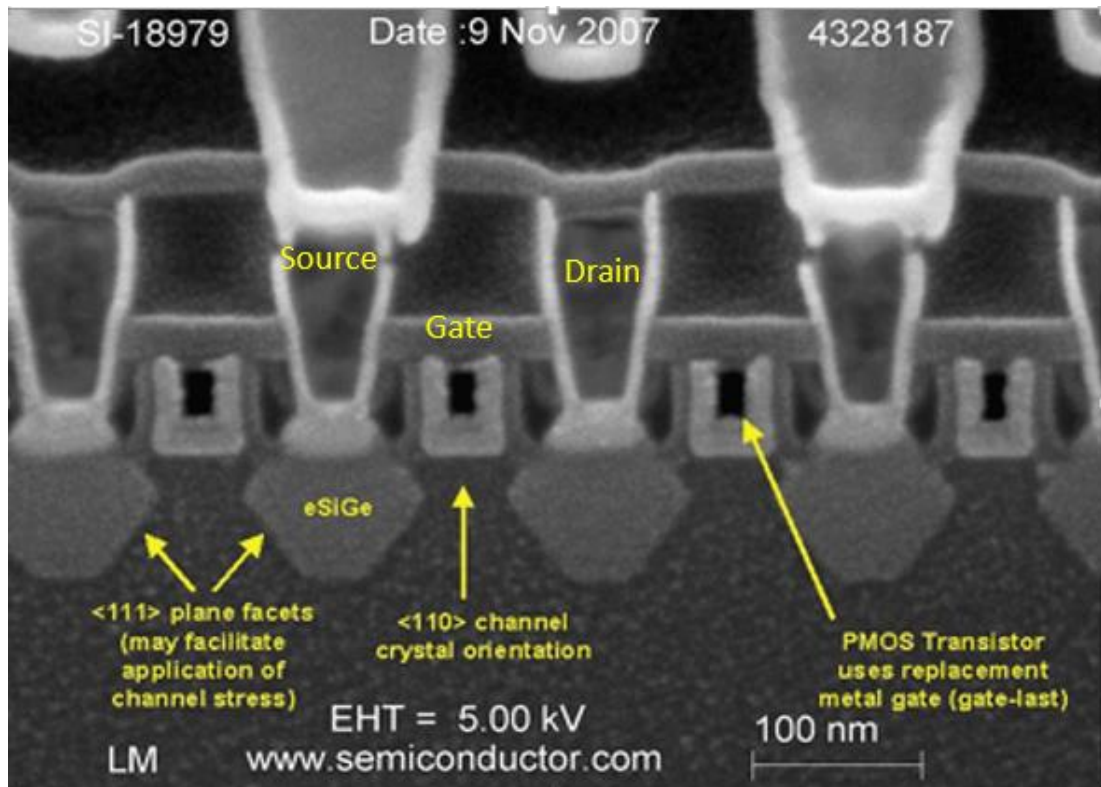


Figure 2-7: Cross section of 45nm transistors showing details of the different profile of the etched structures.

2.3.3 Other considerations for plasma etching

2.3.3.1 Lithography and Photoresist

Lithography and photoresist are a vital components in the patterning of semiconductor devices. The ability of plasma etching to produce smaller feature size is dependent on the ability of the lithographer to provide imaging solutions that can create smaller and smaller patterns in photoresist which act as a mask for plasma etching. To deal with the reduction in line width, lithography has increased the numerical aperture of the lens and reduced the wavelength of the illumination used to expose the photoresist [20]. To accommodate shorter wavelengths of the

illuminated source the photoresist thickness and robustness has been reduced. As a result of these changes to the mask materials and thickness, as well as the large cost associated with printing for small featured masks, significant changes have been made in plasma etching. Firstly, to deal with the reduced robustness of the photoresist, a hard mask is introduced into the process flow. This thin sacrificial layer of silicon nitride, for example, upon which the plasma process transfers the mask from the photoresist to the hard mask using a chemistry which etches away the hard mask except where it is covered by the photoresist. The mask integrity is now maintained by the more robust hard mask enabling harsh processing conditions for a long duration during which the photoresist would have been eroded away. The other option is to trim the photoresist before transferring the pattern. Using a isotropic oxygen discharge, the dimensions of the photoresist mask can be reduced [21]. The technique means that lithography can print a line of 65nm which can be “trimmed” to 50nm resulting in a 50nm etched feature. This technique is especially useful in extending the lifetime of older lithography equipment.

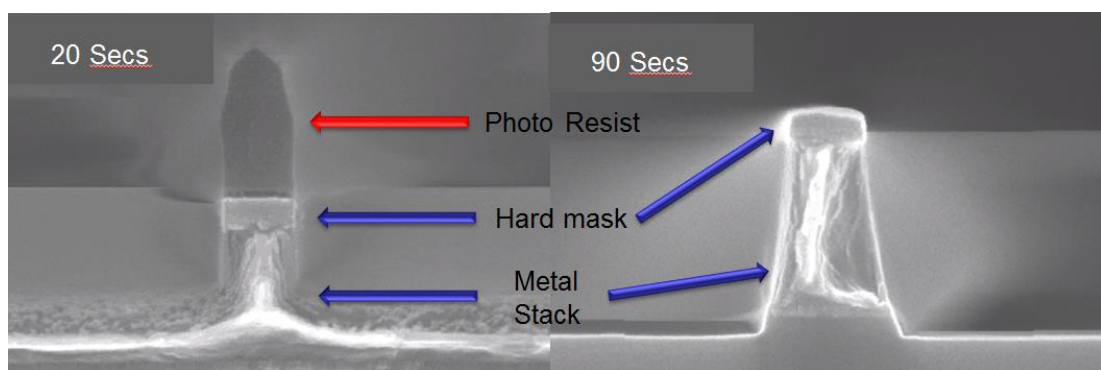


Figure 2-8: SEM cross sections of metal etch stack with photoresist and Si_3N_4 hard masks at 20 and 90 seconds into the etch process. SEMs show the height erosion of the photoresist mask showing the need for the hardmask .

2.3.3.2 *Selectivity and within wafer uniformity:*

Selectivity of a process is the ability to etch one material preferentially over other materials. In plasma etching, selectivity to underlying thin etch stop layers is critical in preventing damage to underlying structures and have been studied extensively [22]–[26]. In Figure 2-8 high selectivity of aluminium over Si_3N_4 is required to prevent the hard mask from being etched during the process and having an impact on the profile of the metal line. Selectivity to the underlying silicon is critical to minimise damage to the surface. Tuning a process to achieve the required selectivity is mostly achieved by tuning the chemistry. If selectivity to an underlying layer is required, the process can be endpointed [27] upon the first signs of breakthrough to the underlying layer. Endpointing can be achieved by monitoring the optical emissions of a particular plasma species or an electrical signal of the RF power [28]. The process chemistry can immediately be modified upon the detection of the breakthrough to be more selective to the underlying layer. In the etching of polysilicon gates using Cl_2/HBr , oxygen is added to improve selectivity to the underlying SiO_2 gate oxide stop layer [19]. The bias power is also lowered to reduce the ion bombardment and allow the oxygen to diffuse into the thin gate oxide promoting oxide growth. Pulsing the RF wafer bias has also been successful in improving the selectivity. The ability to control the ion energy and flux to the wafer surface can significantly improve selectivity [29]. Pulsed plasmas have also been successful in alleviating the issue of notching at the interface of conductive films (polysilicon and aluminium). Notching can also occur at the interface between

underlying dielectric films (SiO_2) and the polysilicon gate. Wafer charging, caused by the charging of the polysilicon line, influences the ion trajectory arriving at the surface of the wafer [30]. Pulsing the RF bias allows the charge build-up to dissipate when the RF bias is momentarily turned off.

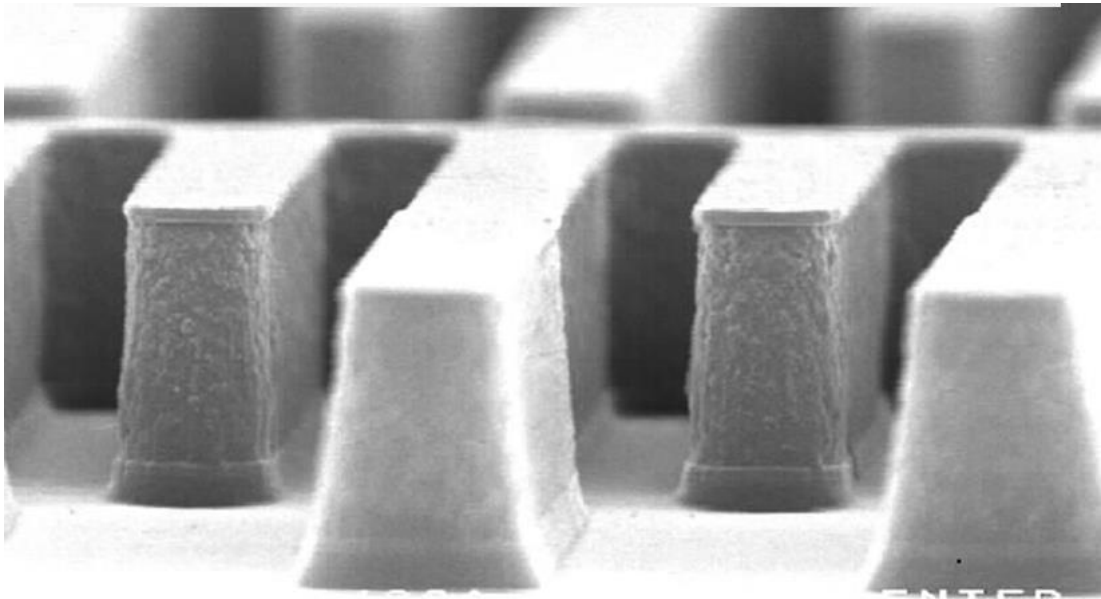


Figure 2-9: Metal interconnects structures providing inter wiring as well as metal contacts to metal plugs connecting the metal layer below using Cl_2 and BCL_3 .

Consider the process used to etch the metal lines in Figure 2-9. The process must etch a near 90° degree profile and ensure that all metal between each metal line is cleared in the most dense structures in the wafer die. Even the smallest amount of metal remaining will cause electrical issues (leaks or coupling) when the device is operational. To achieve this, the process recipe has an aggressive step 1 to remove the bulk of the aluminum and Ti/TiN_3 capping layers as quickly as possible with a less aggressive step 2 to cleanup any remaining stringers in the dense areas of the

wafer. In Figure 2-10, the evolution of the two-step metal etch recipe is examined. The RF voltage on the 2 MHz bias power is displayed alongside cross sections taken at various intervals in the recipe. The RF voltage, and indeed many of the electrical measurements (current, phase angle), give an excellent indication as to the changing conditions of the wafer/process interactions. The RF power of the bias couples through the wafer and into the plasma. As a result, any change in the electrical properties of the wafer surface will have an impact because the wafer forms an integral part of the RF circuit. Hence, as the aluminum is etched away, the wafer's electrical impedance shifts which is reflected in the RF current and voltage. The complete two-step recipe is displayed in black with the blue indicating the point with which the process was halted and cross sections of the metal line profile measured. Both isolated and dense structures at the edge and the center of the wafer were measured in order to determine how the etch was progressing in different locations for different structures across the wafer. At 17 seconds, graph (B), the RF voltage is observed to begin to drop corresponding to the clearing of aluminum at the edge of the wafer in the isolated open areas. The dense structures of the edge and the center of the wafer are still in the process of etching aluminum. Once the aluminum has been etched, Ti/TiN₃ underneath begins to be etched. By 27 seconds, graph (C), at the end of step 1, all the aluminum has been cleared but there are still a number of titanium stringers left in the dense areas at the center of the wafer. The process recipe switches to a less aggressive chemistry and reduced RF bias to give sufficient time for the last of the stringers to be cleared in the dense areas at the center of the wafer. In this second step, the selectivity to the underlying silicon dioxide must be sufficiently high to minimize any damage to the surface. In addition, the selectivity

must also be good enough not to etch the hard mask, SiN_3 at the top of the metal stack. As the isolated structures at the edge of the wafer are the first to clear, these sites are most at risk for any marginality in the process and must sustain a significantly longer exposure. The additional criteria of ensuring that the profile of the metal lines achieves as close to 90° as possible, the passivation of the sidewalls of the aluminum structures is also extremely important. In aluminum etch processes, the sidewall passivation is formed by oxygen from the photoresist eroded by the process forming AlO_2 on the sidewalls of the structure preventing chlorine from etching the metal stack laterally. A consistent supply of oxygen is needed as the aluminum stack is etched. The availability of the oxygen relative to the speed with which aluminum is been etched will determine the profile angle. Ensuring this is consistent for the different structures and locations across the wafer presents a challenge. Once the structures have been etched, the sensitivity to the quantity of oxygen is reduced. However, oxygen is always needed in the chemistry to re-oxidize the bottom of the metal stack where it may be subjected to some ion bombardment due to wafer charging Figure 2-11.

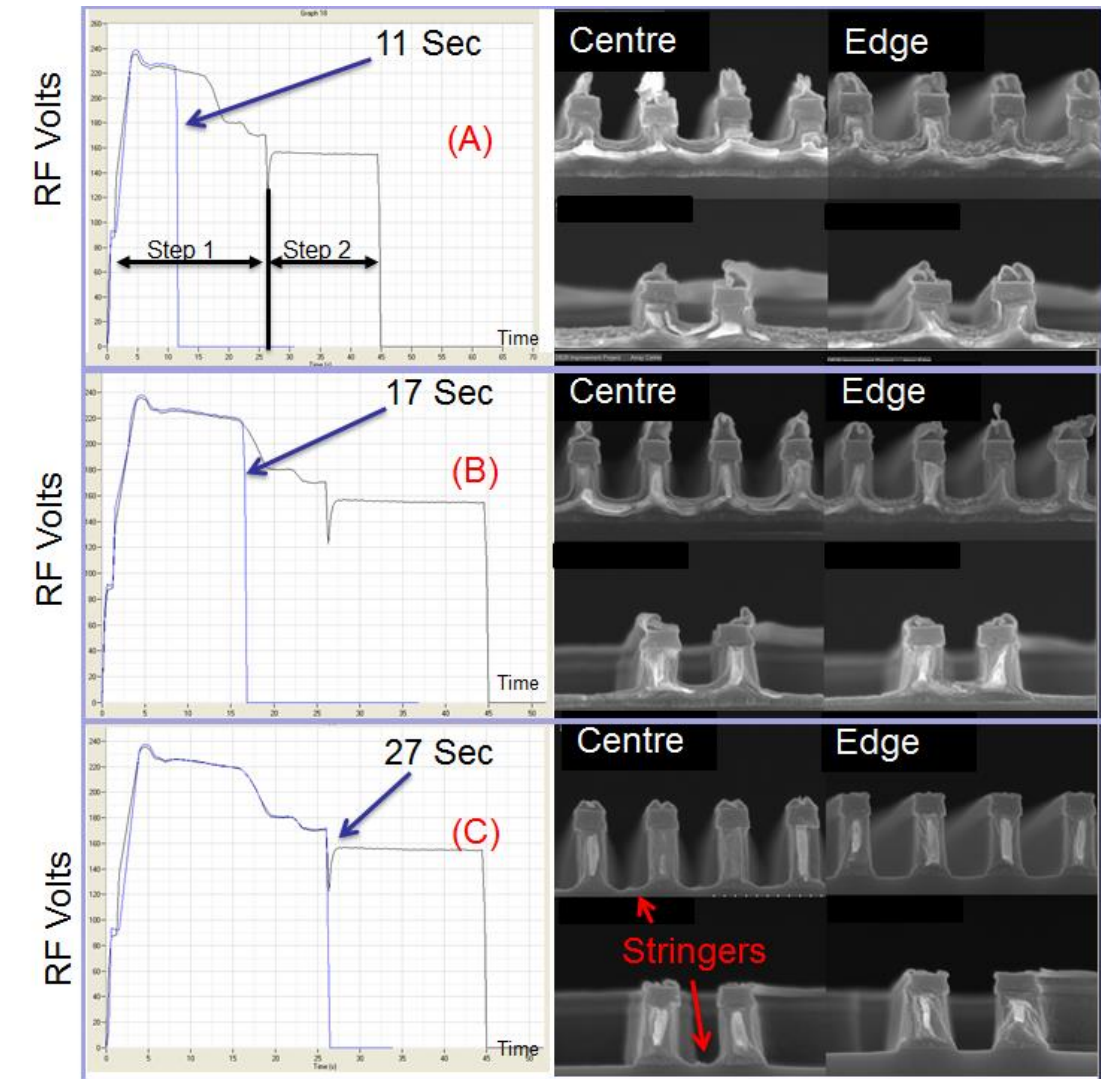


Figure 2-10: The evolution of the metal etch process. The endpoint signal on the left RF Voltage of the 2MHz RF bias displayed on the right the corresponding cross sections of the center and edge of the wafer dense and isolated structures. (scales removed for confidentiality)

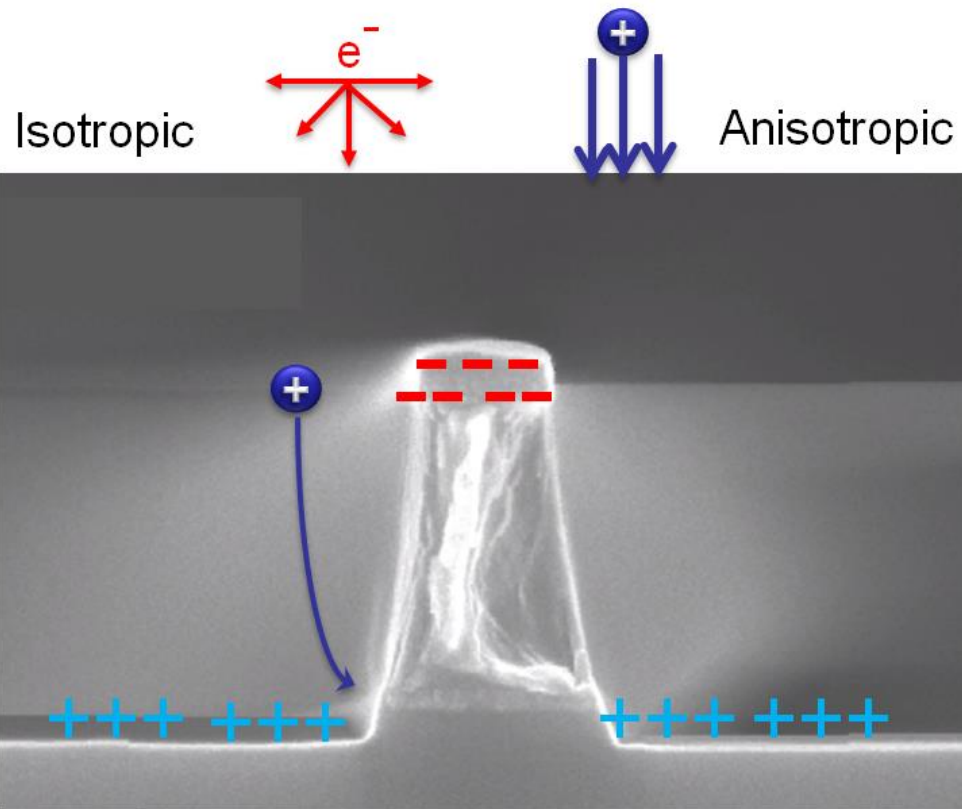


Figure 2-11: Effect of wafer charging due to the different behaviour of the electrons and ions at the surface of a wafer. Charging causes sputtering of the passivation at the bottom of the structure allowing lateral etching of neutrals.

Chapter 3

Process Equipment, Sensors and Statistics

3.1 Introduction

In this chapter the basic principles of the electron cyclotron resonance (ECR) plasma reactors are discussed, in particular, the hardware used for industrial plasma processing. The sensors used for the diagnostic measurements are explained and the statistical approaches used to process the sensor data and correlation techniques are discussed.

3.2 Electron Cyclotron Resonance plasma sources

Electron cyclotron resonance (ECR) plasmas have been in use since the early 1960s for space craft propulsion applications [31]. Suzuki et al. first published the application of a microwave source for plasma etching in 1977 [32]. They have been commercially available in semiconductor factories from the mid-1980s. The main attraction of an ECR plasma source is the ability to generate a high degree of ionization (>10%) at low pressure. Since ECR plasma sources do not rely on a current flowing from an electrode, they offer the opportunity to generate the plasma remotely from the wafer surface. Thus, this minimized the damage to the wafer surface from ion bombardment or device damage from wafer charging issues. The ECR source also allows for the opportunity to independently bias the wafer using a

low frequency RF power supply. Figure 3-1 show a schematic of an industrial ERC etcher. This decouples the generation of the plasma from the control of ion energy and ion flux to the wafer surface. Pulsing the microwave and RF bias further widens the process window increasing the capability of the process chamber to achieve more precise etch processes. The lifetime of ions and radicals generated in the plasma varies. Changing the resonance zone in the chamber effects the time it takes a radical reach the wafer surface and may result in recombination before it reaches the wafer. Therefore, increasing or decreasing the distance from the wafer where radicals are formed can result in different processing conditions on the wafer surface. This can be achieved by altering the position of resonance in the process chamber using the magnetic field settings.

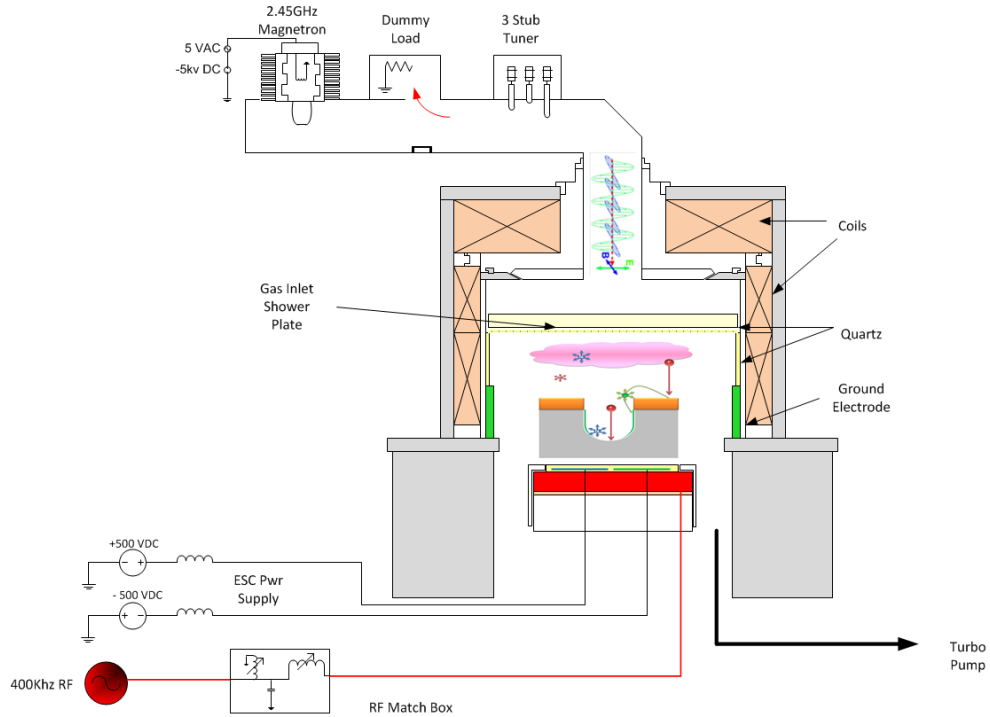


Figure 3-1: Schematic of an industrial ECR plasma etcher with a low frequency RF bias source.

3.2.1 Microwave tuner controller

The function of the microwave tuner is to provide accurate measurement of the forward and reflected power from the plasma. Additionally, a three stub tuner provides varying capacitance to resonate with the varying inductance of the ECR chamber. A voltage standing wave detector is mounted in the waveguide which consists of diodes placed at $\lambda/6$ which feeds the signals into the microwave controller. The measurement of the standing wave voltage allows the calculation of the progressive power propagating towards the plasma and the reflected wave returned from the chamber/plasma combination. The tuner determines insertion lengths of the three stubs which are inserted into the waveguide and provide the exact capacitance to resonate with the inductance of the chamber plasma combination to minimize the reflections. The measured forward power is compared to the recipe

setpoint and adjusts the high-voltage DC current to the magnetron to deliver the required power to the plasma. The tuner outputs the reflection coefficients measurements which are a very useful diagnostic measurement as it gives an electrical impedance that the plasma/chamber combination presents to the microwave power [33].

3.2.2 Electron cyclotron resonance.

The 2.45 GHz high-frequency electromagnetic wave generated by the magnetron and transmitted through the waveguide is introduced into the reaction chamber through a quartz window. A magnetic field is generated in the reaction chamber through three sets of electromagnetic coils, two placed around the chamber and one on the top. Electrons rotate around the magnetic lines of force with an electron cyclotron angular frequency given by the equation:

$$\omega_c = \frac{eB}{m_e} \quad 3.1$$

where e is the electric charge, m_e is the mass of an electron and B is the magnetic field[10]. The electric field of the 2.45 GHz microwave delivered through the waveguide is superimposed on the perpendicular magnetic field lines generated by the electromagnets. At 87.5mT magnetic flux density, the 2.45 GHz microwave will cause the electrons to rotate at 2.45 GHz around the magnetic field lines. As the electrons are spiralling around the magnetic field lines, they continuously accelerate achieving very high energies. This resonance zone is where the microwave energy is strongly absorbed. Magnetic flux density higher than the 87.5mT is required in the source region of the vacuum window above in order to facilitate the propagation of

the microwaves into the vacuum chamber before reaching the dampening of the ECR zone[34]. In Figure 3-3 Kushner's [35] simulation of an ECR chamber is displayed. The results show that most of the microwave power is absorbed in the resonance zone accelerating electrons to very high energies. These electrons then collide with the neutral gases causing a high degree of ionization which again is highest in the resonance area.

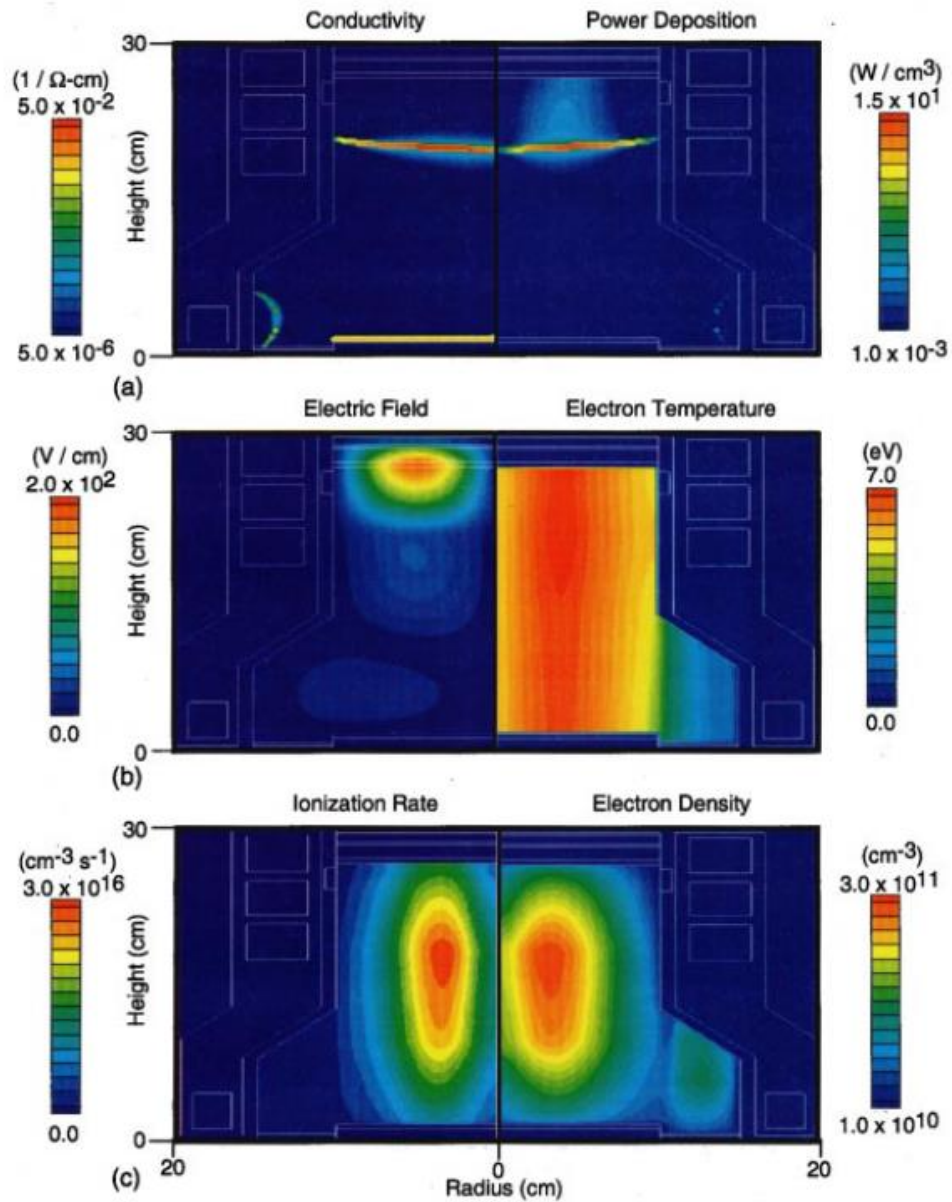


Figure 3-3: Plasma modeling completed by Kushner et al[36]. The simulations show the power deposition, electron temperature and density in ECR reactor.

The electrode upon which the wafer is electrostatically clamped is connected to a 400 kHz RF power supply. As discussed in Chapter 2, 400 kHz frequency is below the ion frequency and therefore the ions will be influenced by the modulation of the sheath voltage. The $2.5\mu\text{s}$ period of the RF cycle is slow enough to allow ions to

transition across the sheath bombarding the surface of the wafer. The RF is controlled to a power setpoint. An electrostatic chuck used to clamp the wafer to the electrode facilitates high-pressure helium to be delivered to the gap between the electrode and the wafer, thus, enabling heat transfer from the wafer to the water cooled electrode.

3.3 Measurement techniques

The adoption of sensors in industrial plasma reactors has not progressed to the same extent to the capability developed in academia for plasma diagnostics. Process equipment manufacturers have always measured equipment parameters such as pressure, power, temperature, etc. in order to control the equipment. They also provide some basic alarming if process setpoints have not been achieved. In the 1990s a generic protocol for communication and control of semiconductor manufacturing equipment was agreed upon and the development of software began that could record the equipment parameters [37]. However, few of these parameters relate to the process and measurement of the process parameters in the industry remains relatively poor. The poor availability of robust process sensors, and the necessary software modeling to interpret the data, has limited implementation of advanced sensors in the industry. Many plasma diagnostic sensors are intrusive and cannot be used in a manufacturing environment. In addition, the corrosive chemistries used for industrial processes also limit the choice of sensors. In this section two non-invasive measurement techniques will be discussed along with two invasive sensors that are used for some fundamental characterization.

3.3.1 Optical emission spectroscopy

Chapter 2 describes the electron heating mechanisms in an RF discharges which results in a distribution of electrons with varying energies (EEDF). These electrons collide with the gasses in the process chamber causing excitation and ionization as discussed in Chapter 2. The subsequent relaxation by spontaneous emission to lower energy states can occur in one or several transitions with lifetimes varying from nanoseconds to seconds. The transition is accompanied by a photon emission at a wavelength related to the change in energy levels. The unique spectrum emissions of the atomic and molecular species in the plasma offers a very powerful diagnostic measurement of the discharge. In principle, if all the excitation process rates, as well as the electron density and temperature were known, it is theoretically possible to calculate the species densities from their optical emissions. In reality, is not possible and therefore the relationship between the emission of a species and its density is somewhat ambiguous. Notwithstanding this, for diagnostics of industrial plasma processes, spectroscopy has proven to be a very powerful diagnostic tool. The non-intrusive nature of the measurement renders it suitable for use in industrial plasma processing applications.

Two types of spectrometers where used in this study,USB2000 and HR4000 both made by Ocean Optics. The USB2000 has a 2048 element charge-coupled device (CCD) array which has a response of 250-850nm which give ~3lines/nm optical resolution with a entrance aperture (slit) of 25 μ m with a 42mm focal length. The

HR4000 has a 3648 element CCD array measuring 200-1100 nm with a 5 μ m slit giving a ~4lines/nm resolution with a focal length of 101 mm.

3.3.2 Current voltage probes

The electrical characteristics of the plasma process and hardware combination is another useful diagnostic measurement. The electrical measurement is usually taken between the RF matching unit and the powered electrode. A sample of the voltage waveform is capacitively coupled to a detector and a sample of the RF current waveform is usually inductively coupled to the detector. Both signals are processed and the phase angle between the current and voltage is also calculated. Harmonics of the fundamental frequency are generated by the nonlinearity of the modulation of the plasma sheath and can be measured and calculated using Fourier analysis. Harmonics measured by the VI probe are very sensitive to small changes in the sheath. If the wafer is placed on the powered electrode, RF harmonics have shown to be able to detect 0.5% open area endpoint[38]. Other studies of the harmonics have shown them useful in modelling the sheath behaviour [39]. Useful data from the VI probe is used to measure the actual power delivered to the electrode which can determine the losses in the match and delivery system as well as the determining the real and imaginary elements of the plasma/hardware combination which is detailed later in Chapter 6.

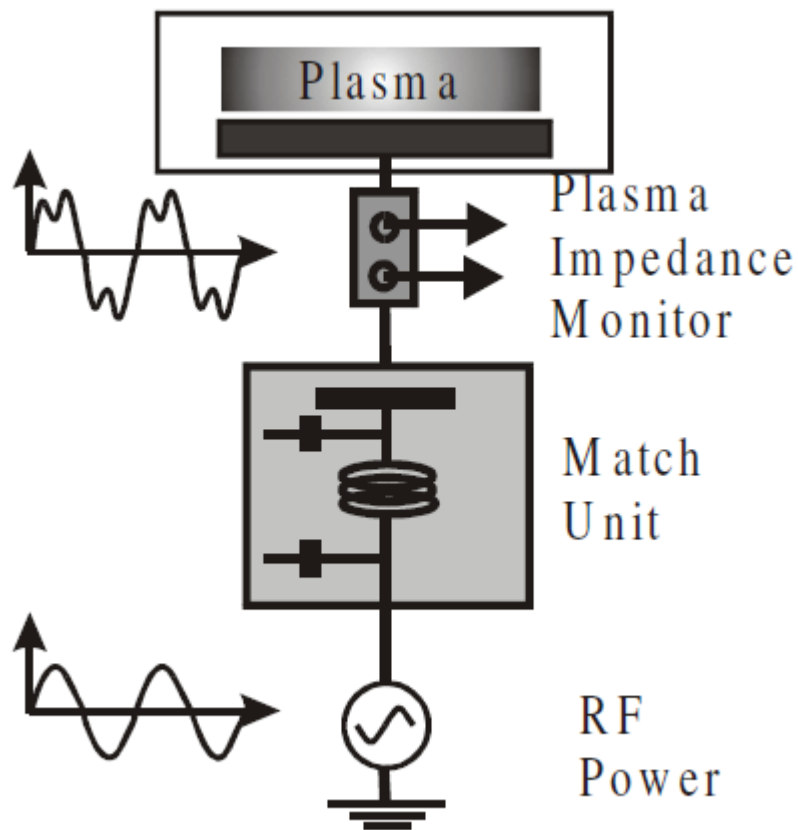


Figure 3-4 VI Probe sensor inserted between the match unit and the plasma chamber. [40]

3.3.3 Hairpin probe

A microwave hairpin resonator (hairpin probe) has been established as an effective way of measuring electron density in plasmas. The hairpin probe is an open-ended u-shaped quarter wavelength transmission line. When a suitable frequency signal source is applied to the short end of the probe, maximum power coupling takes place. This specific frequency has a quarter wavelength which equals the length of the pins.

The resonance frequency is related to the dielectric constant of the medium that surrounds the probe.

The resonance frequency f_r of the hairpin probe is given by [41]

$$f_r = \frac{c}{4L\sqrt{\epsilon}} = \frac{f_0}{\sqrt{\epsilon}} \quad 3.2$$

where c is the speed of light, and L is the length of the resonator, ϵ is the permittivity of the surrounding medium plasma and f_0 is the resonance frequency of the probe at vacuum.

Plasma can also be treated as a dielectric. If the thermal motion of electrons can be considered weak as compared to the electric field set-up between the pins, then one can model the plasma permittivity based on cold plasma approximation, which ignores the thermal motion of electrons. At low pressures, the electron neutral mean free path can be larger than the separation between the pins. Hence plasma permittivity can be given by [4]:

$$\epsilon_p = 1 - \frac{f_p^2}{f^2} \quad 3.3$$

where f_p is the plasma frequency. By substituting equation 3.2 into equation 3.3 the resonance frequency of the plasma can be expressed by:

$$f_r^2 = f_0^2 + f_p^2 \quad 3.4$$

The above equation can be further simplified [4][41]:

$$n_e = \frac{f_r^2 - f_0^2}{e^2/\pi m_e} \quad 3.5$$

where n_e is the electron density, e is the electronic charge, m_e is the mass of an electron. The

Data collection with a hairpin probe involves inserting an invasive probe into the plasma discharge. While this is not feasible in a production environment, it is possible to take the equipment off-line to make measurements. A microwave generator provides a sweeping signal from 2.0 to 3.8 GHz. The reflections are measured on an oscilloscope. The resonance point is measured at vacuum and then again under plasma conditions. The change in frequency from vacuum to plasma is used in equation 3.5 to determine the electron density.

3.4 Statistical analysis techniques

Statistics have a long history of implementation in semiconductor manufacturing. Statistical process control (SPC) has been widely used to set critical manufacturing parameters. More recently, with the availability of equipment parameters from processing equipment, statistical controls have been implemented on these

parameters. Univariate and multivariate analysis of these equipment parameters has been adopted in semiconductors manufacturing. However, these unsupervised analytical techniques are prone to false fails and missed alarms because they use statistical limits and not correlations to quality measurements. In particular, parameters that are sensitive to the process behave nonlinearly. In Figure 3-5 the RF voltage from a plasma etch process is greatly disturbed due to maintenance and chamber conditioning. This variation in the data is a challenge for applying appropriate statistical limits for fault detection. The supervised learning approach (virtual metrology) where correlations can be established with the metrology and the process parameters provides a more accurate and robust fault monitoring/detection capability. When this technique is combined with periodic model retraining it offers a very reliable fault monitoring system.

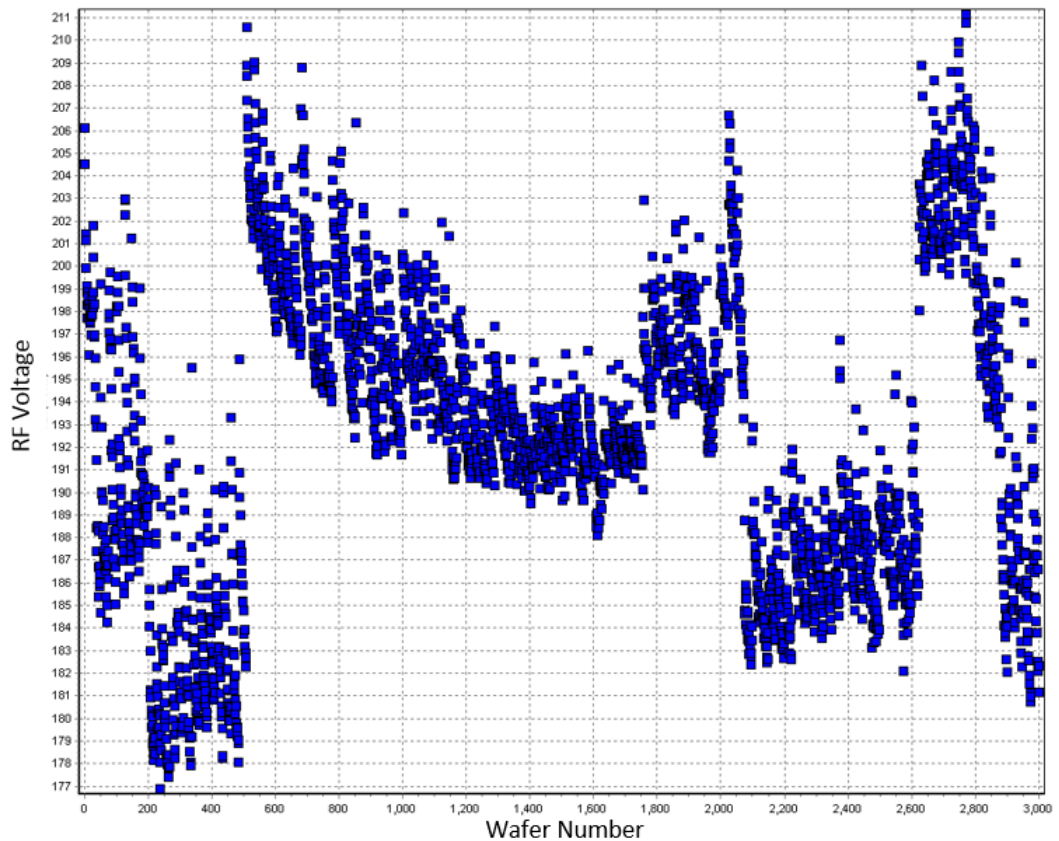


Figure 3-5: The mean value of RF voltage measured at the bias electrode (RMS) for 3000 wafers. Large shifts due to maintenance activity.

3.4.1 Summarisation of time series data

The data from sensors and equipment parameters is normally acquired at 1 Hz. This time series data must be rolled up into summary statistics in order to be merged with metrology data for analysis. In addition, the sheer volume and unstructured format of the data makes analysis and visualization difficult. The best approach has been to describe each recipe step with a set of statistical features. Figure 3-6 displays a typical process recipe and how the statistical features are calculated per step. These features

can then be rolled up together to give an accurate picture of the time series behaviour of each wafers process. This technique is most useful when looking at large volumes of wafers to characterize the performance of the process chamber over time. However, when anomalies are detected, it is imperative that the original data from which statistics are calculated is available to the engineer in order to help with diagnosis. Principal component analysis of the time series data are investigated in Chapter 4 and are useful in determining the main patterns in the OES data.

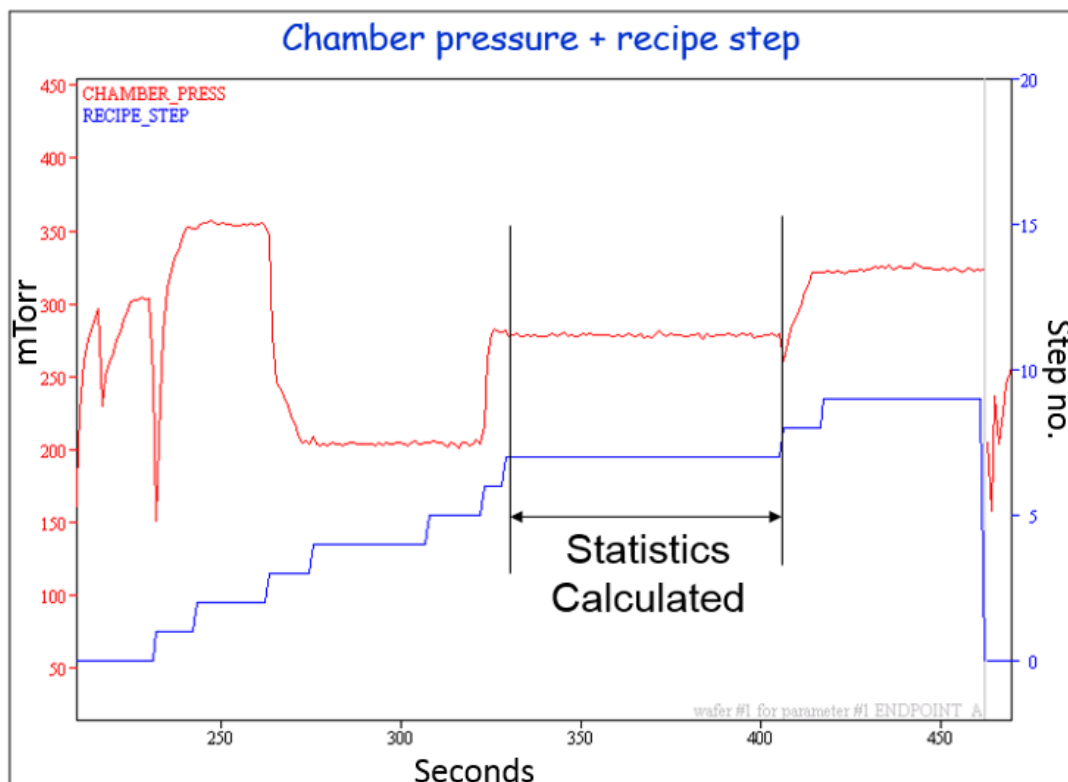


Figure 3-6: The changes in the recipe step is a function of time and the corresponding change in pressure.

3.4.2 Principal Components Analysis

Principal component analysis (PCA) is an unsupervised dimensionality reduction technique that extracts explanatory variables from the data and is especially useful for exploring the variation in the data sets and finding patterns.

In figure 3-7, a two dimensional dataset (x,y) is shown in (a). The principal component analysis can be considered as a rotation of the axis of the original coordinate system to new orthogonal axis that coincides with direction of maximum variation [42]. The construction of the two principle components (PC's) which pass through the direction of maximum variation are shown in Figure 3-7. Projecting each observation onto the principal component (PC), the distance to the PC gives a score for each observation.

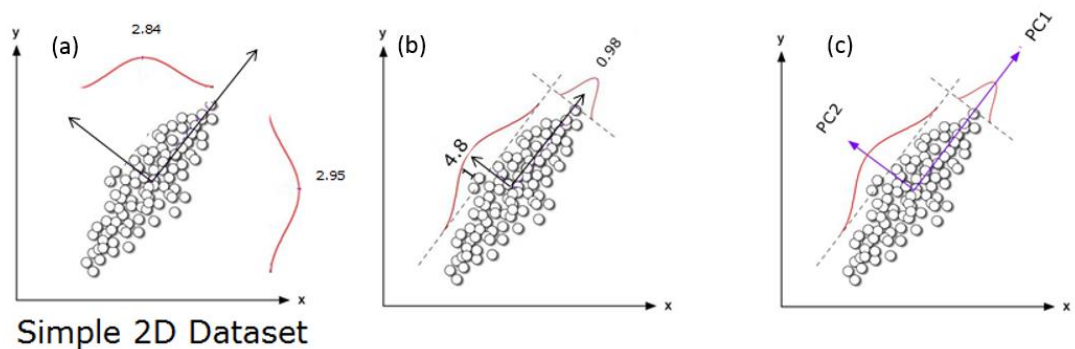


Figure 3-7: This two-dimensional representation of principal component 1 and 2 capturing most of the variability in the data set[43].

The angle between the PCs and the original variables is calculated. A small angle indicates that the variable has a large impact because it is most aligned with that particular principal component. A large angle indicates that that variable has little influence on that principal component. A loading plot shows how the variables influence the principal component.

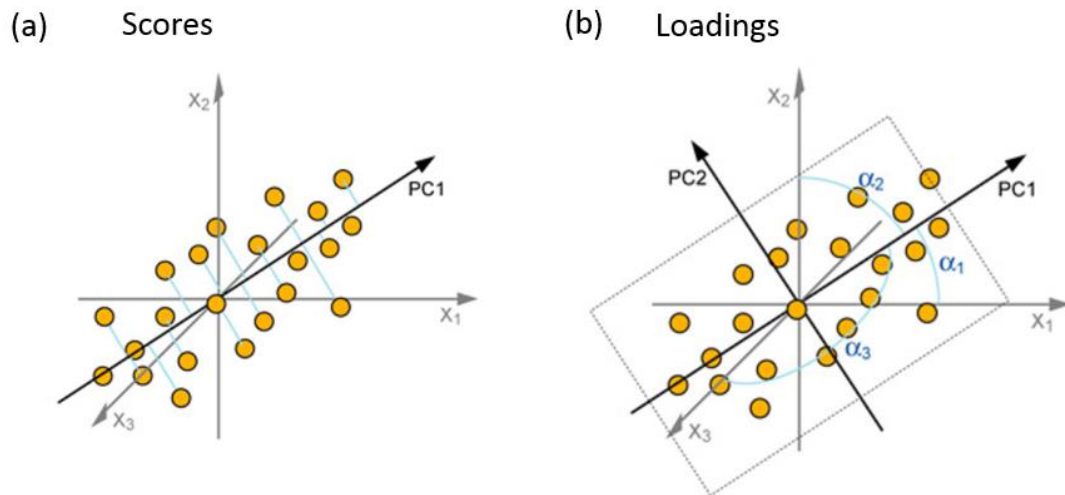


Figure 3-8: The score for each observation is the distance to the PC (a). The loading for each PC is the angle each variables is from the PC[44].

Before PCA is performed the data is normally pre-processed. Each variable is mean centred and normalized to unit variance by dividing by the standard deviation. This is necessary because each variable can be measured on different scales and units (e.g. temperature and voltage).

Next the covariance matrix is calculated. This is how much each pair of variables vary from their mean with respect to each other. Consider a matrix of variables where

For two vectors $X = \{x_1 \dots x_n\}$ and $Y = \{y_1 \dots y_n\}$ the covariance matrix is expressed by:

$$cov(x, y) = \frac{1}{n-1} \sum_1^n [(x - \bar{x})(y - \bar{y})] \quad 3.6$$

Where \bar{x} , \bar{y} are the means of X and Y respectively. The eigenvectors and corresponding eigenvalues of the covariance matrix are calculated. The eigenvector of a square matrix, A, is a non-zero vector v where the matrix is multiplied by the vector it yields a constant multiple of v :

$$Av = \lambda v \quad 3.7$$

where λ is the eigenvalue.

The eigenvectors (principal components) are arranged in descending order by eigenvalue consistent with the amount of variance explained. The eigenvector with the largest eigenvalue is the first principal component and explains the most variances in the dataset [45].

Hotelling's T^2 statistic is commonly used in conjunction with PCA and is a measure of the variation in principal component space. The statistic is defined as the sum of normalised squared principal components and is calculated for x_i of $X = \{x_1 \dots x_n\}$

$$T^2 = x_i P W^{-1} P' x_i$$

3.8

Where P is the PCA loading matrix and W is the diagonal matrix of the eigenvalues associated with that principal component.

3.4.3 Gradient Boosting Trees

Gradient boosting trees (GBT) is a supervised machine learning technique in which a model is built to predict an output Y from a set of input variables X. A decision tree is a tree structured layout of decision rules (logical splits) on the X variables to predict Y. In Figure 3-9 a decision trees is built to predict the weather from three X variables, temperature, humidity and dew point. The model would typically be trained using historical data and then used to predict the weather using the measurements.

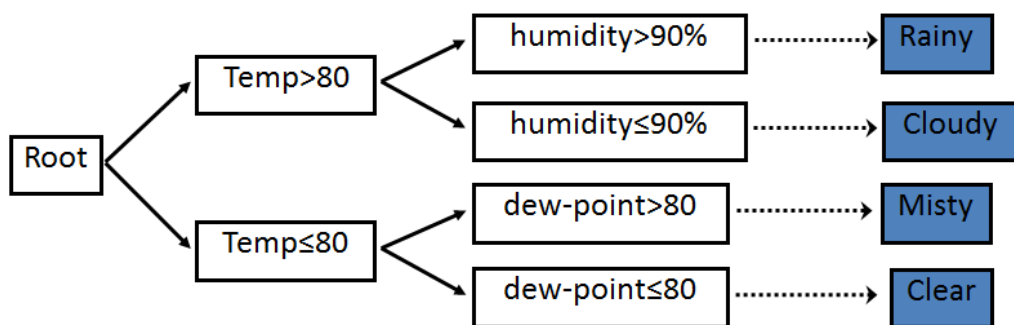


Figure 3-9: Shows a simple decision tree to predict the weather (Y) from temperature(X1), humidity (X2) and dew- point(X3)[46].

Depending on the nature of the data these decision trees works very well in producing accurate predictions. This single tree approach has some limitations in dealing with more complex and larger data sets. These trees can be unstable when small changes in the data can result in very different series of splits giving errors that propagate down the tree due to the hierarchical nature of the process.

The GBT algorithm computes the sequence of small trees for prediction. The first tree is constructed to predict Y . The error or residuals in this tree's prediction are determined. The next tree is constructed to predict these residuals (prediction errors). The process is then repeated to predict the errors from the previous tree and so forth. The depth of each tree and the number of trees constructed are tuned for each data set's characteristics in order to minimize the error prediction and prevent over fitting.

Chapter 4

Case Study One - Virtual metrology of a Plasma Etch Process

4.1 Introduction

Virtual Metrology is a concept used in the semiconductor industry where physical and/or electrical parameters of wafers and/or devices is estimated from information collected in real time from the manufacturing tools (e.g., equipment or process parameters) and from other available sources (e.g., production context information or up-stream metrology). The benefit of this virtual measurements is that it can be done before physical metrology is available giving early warning of process drift as well as affording the opportunity to reduce the numbers of wafers measured at metrology reducing cost.

In this chapter a two-step etch process (SF_6/Cl_2 , NF_3) is investigated to study etch-rate variability over a 6000 wafer period through the analysis of OES data collected for every wafer. Linear regression and gradient boosting trees modelling techniques are employed and evaluated for their suitability in estimating etch rate and also for investigating the source of the common cause process variability and special cause variability. The modelling results suggest that etch by-products adhering to the chamber walls are the main contributor to the etch rate variability. The results are validated by sampling the polymer build-up from the chamber walls and performing

elemental analysis of the sample. Experimental wall pre-treatments are also used to validate the hypothesis.

4.1.1 The etch process

After a transistor gate structure has been fabricated and spacers deposited and etched, the next step is an etch undercut operation. This is done to reduce the effective gate length of the transistor. This trench is subsequently filled with epitaxial strained silicon as shown in the Figure 4-1. This process has two functions; firstly the lateral etch under the gate reduces the “effective gate” width allowing the device to clock at high speeds. Secondly, the strained silicon fill increases the electron mobility again allowing faster gate switching. The requirement is to tightly control these very critical gate dimensions which presents challenges to the etch process. The specifications need to be maintained in both the vertical and horizontal directions. Since there are no termination layers, endpoint detection is not possible and any variability in etch rate (vertically or laterally) will be reflected in dimensional changes in the feature dimensions and hence the electrical performance of the device. The trade-off between speed and leakage requires precisely specific physical dimensions of the etched trench. If the trench is too shallow or the lateral etch too narrow the device will not clock as fast and if the effective gate is too narrow the device will leak more.

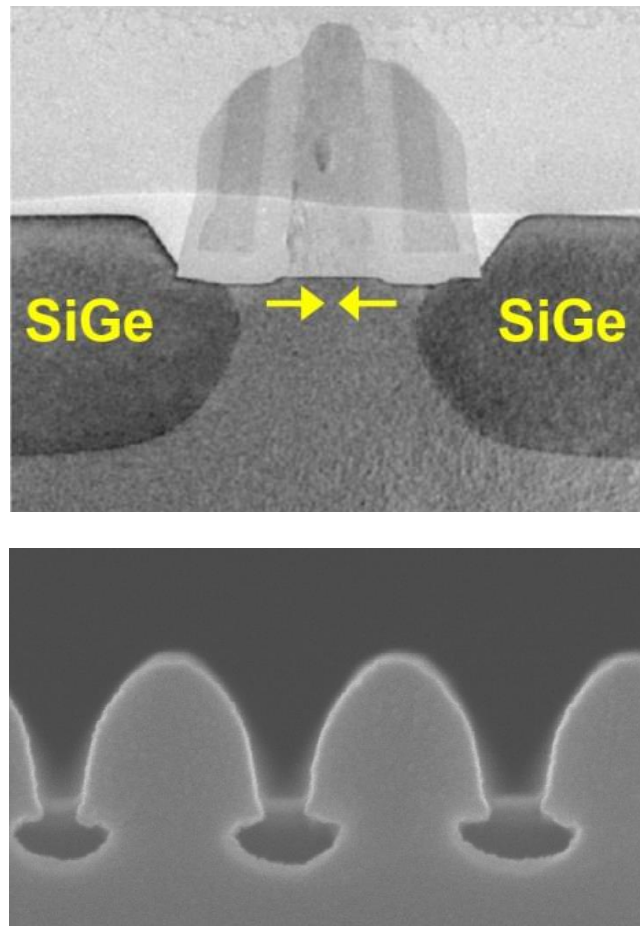


Figure 4-1. Transistor Gate (scales excluded)

4.1.2 Recipe structure

A two-step process is used to etch under the transistor gate. For confidential reasons the exact dimensions of the gate and chemistries used are not specified.

1. Step one employs a dilute SF_6 and helium anisotropic chemistry to etch through the native oxide film on the surface of the wafer and to etch down vertically to a targeted depth. Ion flux needs to be minimised in order to reduce damage, therefore no active RF bias was used in this case.

2. With the plasma on the chemistry is switched to $CL_2/NF_3/Ar$ chemistry with an increase in pressure and a decrease in microwave power. This isotropic etch step further deepens and undercuts laterally under the gate.

In Figure 4-2 the evolution of the gate profile shows how the profile progresses within each step of the two steps recipe. The first step etches anisotropically using while the second step etches both isotropically.

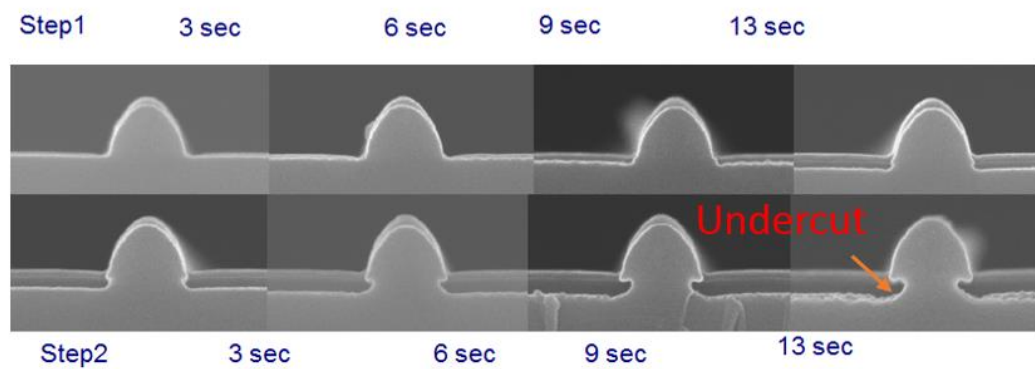


Figure 4-2: Time evolution of the profile progressing through the etch process.

4.1.3 In situ plasma chamber cleaning

Coating of the chamber walls is a normal and unwanted consequence of the industrial chemistries used for wafer etching. As discussed in Chapter 3 Etch processes are designed to create a precise combination of etch and deposition that results in a desired etched structure. In addition by-products of the etched wafer may also deposit on the chamber walls. The effect of this deposition of unwanted coatings on the chamber walls is that it can contaminate the etch process by recycling gas species

back into the process and may also promote further chemical absorption of key gas species through recombination on the walls. In addition, if chamber coatings are allowed to continuously grow they eventually begin to flake off and cause defects on the wafer surface. In order to maintain wafer to wafer and lot to lot reproducibility and prevent the deposited film from growing too thick on the chamber walls, in-situ plasma cleaning regimes are employed. In this particular etch process an SF₆ plasma clean is performed before a lot is etched in the chamber. Between each wafer a Cl/HBr/O plasma etch is used to ensure the chamber walls have a consistent SiOCl_x film on the walls. This pre-treatment of the chamber wall is to enhance wafer to wafer reproducibility.

4.1.4 Sensor process measurement and data collection

An Ocean Optic USB 2000 spectrometer was used to collect a 250-850 nm spectrum. A fibre optic was mounted in a window in the waveguide which collects light from a view port looking down into the process chamber. More details of the spectrometer specifications are presented in Chapter 3.3.1. A HR4000 spectrometer was used only to measure experiments. A data acquisition system was employed to collect OES data from the USB2000 and equipment parameters at 2 Hz for each wafer processed in the chamber. Mean and standard deviation summary statistics were calculated for each recipe step.

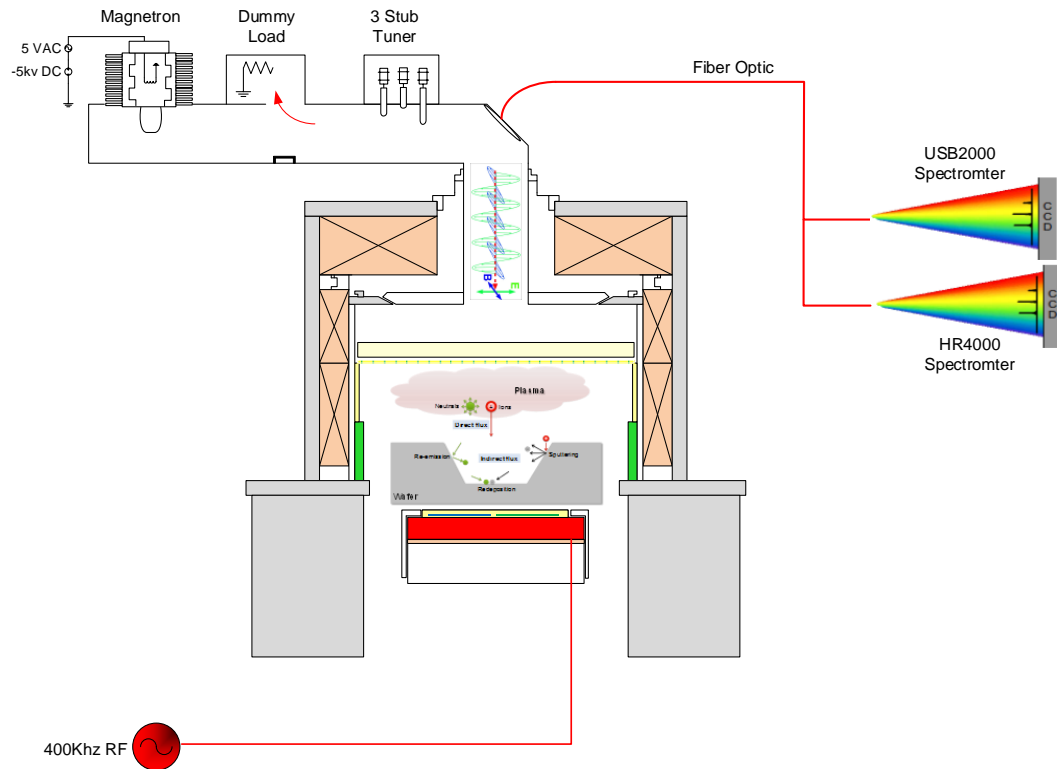


Figure 4-3: Schematic of ECR plasma chamber with OES sensor measuring light from a window looking down into the plasma chamber.

4.1.5 Post etch metrology

Post etch, the lots receive a number of wet chemical clean steps to remove any residue left over from the etch process. Subsequently, a profilometer is used to measure the depth of the undercut. As it is not possible to measure the trench at the transistor gate, a large trench test structure is purposely placed between each die and is measured as a proxy for the undercut depth at the transistor. The depth of ten test sites spatially distributed across the wafer are measured. The measured depth is

divided by the total time of the recipe to give an etch rate and averaged for each wafer. A total of seven wafers in each lot is measured for trench depth.

4.1.6 Automated Process Control

Automated process control (APC) automatically adjusts the recipe selected for each lot based on incoming or post metrology. In this process, feedback metrology from the downstream depth measurements are used and an EWMA (effective weight moving average) algorithm modifies the recipe step time to maintain a target trench depth. It achieves this by taking the weighted average depth of the last nine lots given a larger weight to the more recent lots and calculates the difference from the target depth for the process. A lookup table was developed at the start of the APC implementation in which the relationship between the addition recipe time and the resultant change to the etched depth was determined. The APC systems then consults this table in order to determine how much to adjust the step time in order to bring the etched depth back on target. This then determines which recipe is selected for the subsequent lot.

4.1.7 The dataset

Data was collected over a four month period. The etch rate for the period of data measured is displayed in Figure 4-4. In this four month timeframe a sudden drop in etch rate was observed at wafer 190 when the process chamber went dramatically out of specification for one lot. An increase in etch rate was observed from wafers 600-1000 after which it returned to normal and again at wafer 1450 a slight increase was observed. There is also a significant variation in etch rate within each 25 wafer lot.

In order to reduce the data size without losing information Summary statistics (mean and standard deviation) of the all the sensor data were calculated and the metrology for the four month period are merged into a single dataset for analysis.

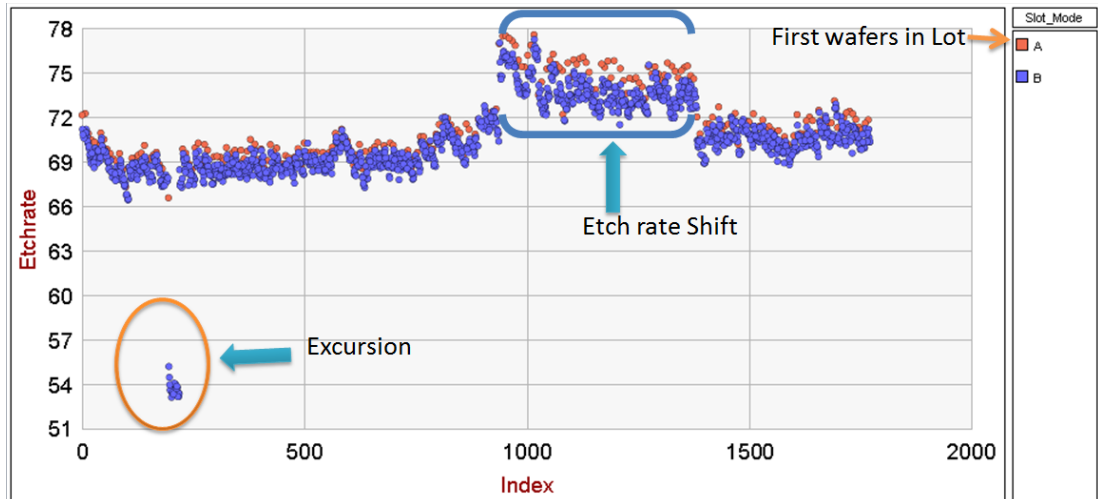


Figure 4-4 Etch rate in $\text{Å}/\text{sec}$ performance of chamber of period of 4 months in which 6000 wafers were processed and 1700 of these wafers had metrology measurements.

Seven wafers in each lot consisting of 25 wafers were measured at metrology and the etch rate for those wafers was merged with the associated sensor data. Wafers in slots 1,5,9,13,17,21 and 25 were typically measured. Context information such as lot ID, recipe, slot number etc. were also added to the data set. Wafers in the dataset with no metrology measurements were removed from the dataset. The time series data from which the summary statistics were calculated and retained for later analysis.

4.2 The analysis of time series OES spectra of a production recipe

The main objective of OES analysis in this study is to estimate the chemical concentration of the species in the plasma and study how they relate to the etch rate performance of the chamber. Understanding the wafer surface chemistry can lead to a better understanding of the mechanisms involved in the etching of features on the wafer. Understanding the chemical species in the spectrum and the rate with which the density of the species are changing within the recipe steps provides valuable information about the process. The intensity of a spectral line can be used as a proxy for the density of a species in the plasma when measured within one wafer's recipe or from wafer to wafer[47]–[49].

The spectral peak identification of complex industrial plasma chemistries is not a straightforward task. Industrial chemistries contain a variety of gasses and the interaction of chamber walls and etching silicon wafers can create a very complex spectrum of atomic and molecular species emissions. Atomic spectral lines are well documented in the online NIST database [50]. The low resolution of industrial spectrometers give broadened spectral lines making individual spectral lines difficult to isolate and identify. The spectrum of a HBr/Cl₂ plasma measured with a high resolution HR4000 (0.05nm) and low resolution spectrometer USB2000 (0.25 nm) is shown in Figure 4-5. In the low resolution spectrometer the hydrogen and bromine peaks adjacent to each other blend together whereas with the higher resolution spectrometer the individual lines can be resolved into individual peaks.

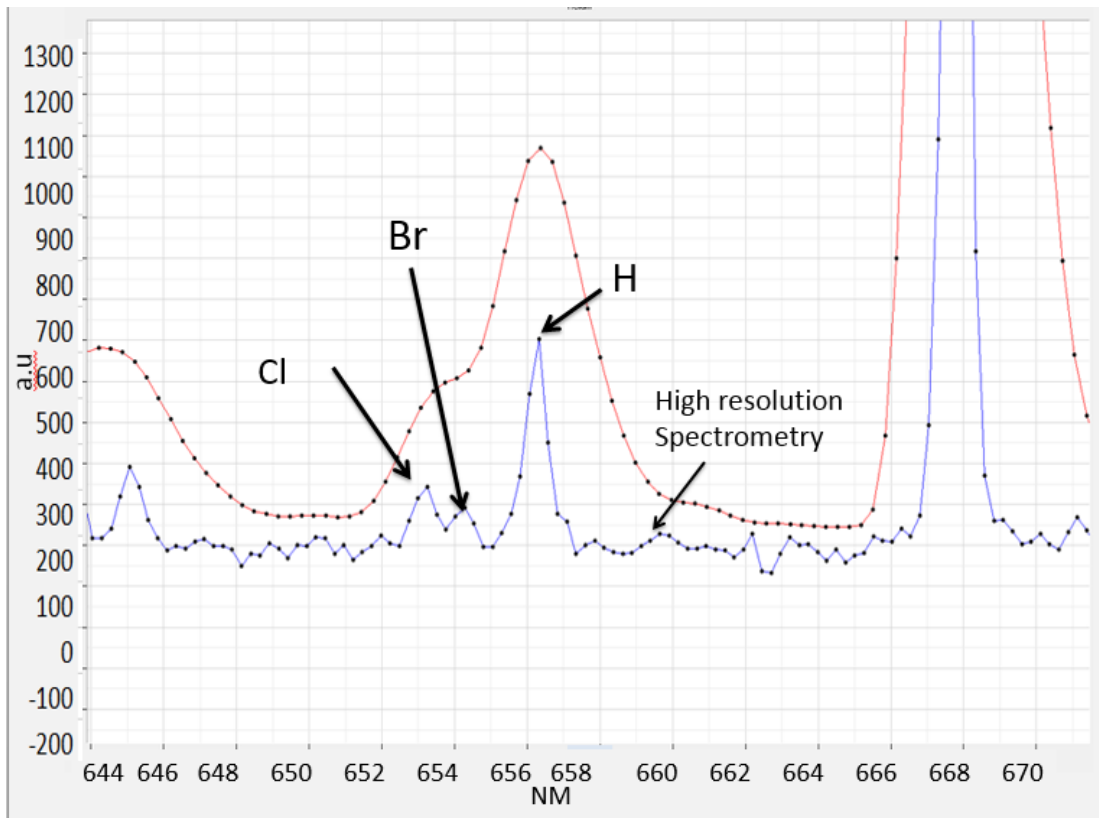


Figure 4-5: Low (Red) verse High (Blue) resolution Spectrometer displaying resolved and unresolved lines for Cl, Br and H lines.

A number of different approaches are described here that can be used to determine suitable spectral lines. In addition, virtual metrology can be employed to correlate OES spectral lines to metrology. Virtual metrology is an important technique in determining variables that are related to the variability of metrology. This technique is described in more detail later in the section 4.3.

4.2.1 Analysis of time series OES spectra

The spectral data for a two-step recipe is displayed in Figure 4-6. In step one, SF_6 and helium etch for 15.0 seconds. The plasma stays on while the recipe chemistry changes to $\text{Cl}_2/\text{NF}_3/\text{Ar}$. These transitions can be observed in the emission spectrum. Analysing the transients between recipe steps can be a very useful diagnostic in evaluating the dynamic performance of the chamber's response to recipe parameter changes. The dynamic performance of MFC's (mass flow controllers), pressure control and power tuning responses are very important characteristics of a process chamber. This performance can be a very important factor in matching chambers in a factory. In Figure 4-7 the transient behaviour of chlorine is shown when the MFC is turned on in a plasma-on transition step. In this case, the 'blue' flow controller releases a burst of chlorine at turn-on when compared to a normal 'green' flow controller. This chlorine burst resulted in a chamber mismatch in etch rate.

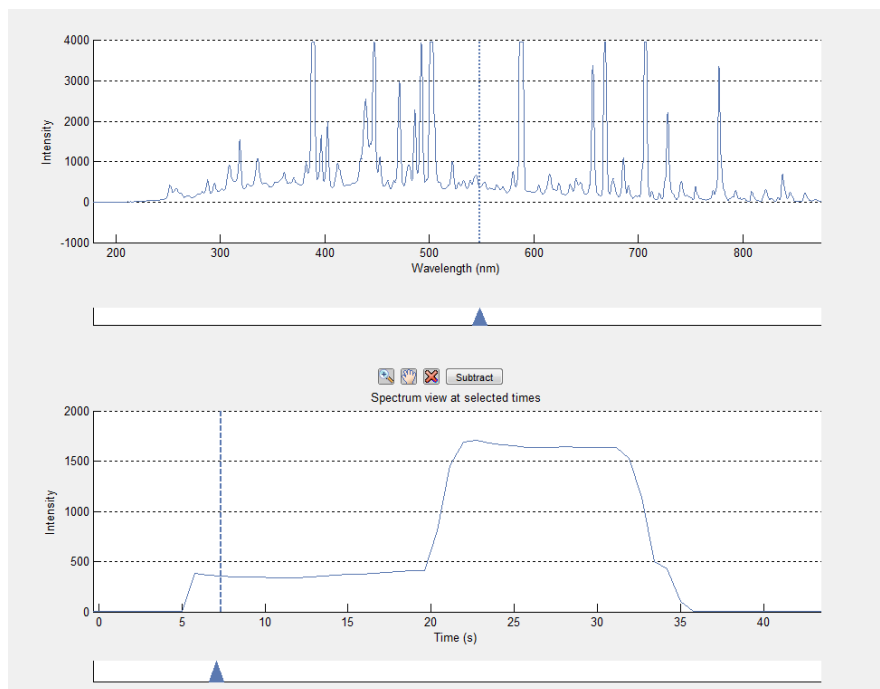


Figure 4-6 displays the spectrum at 7 seconds and the temporal behavior of 550nm

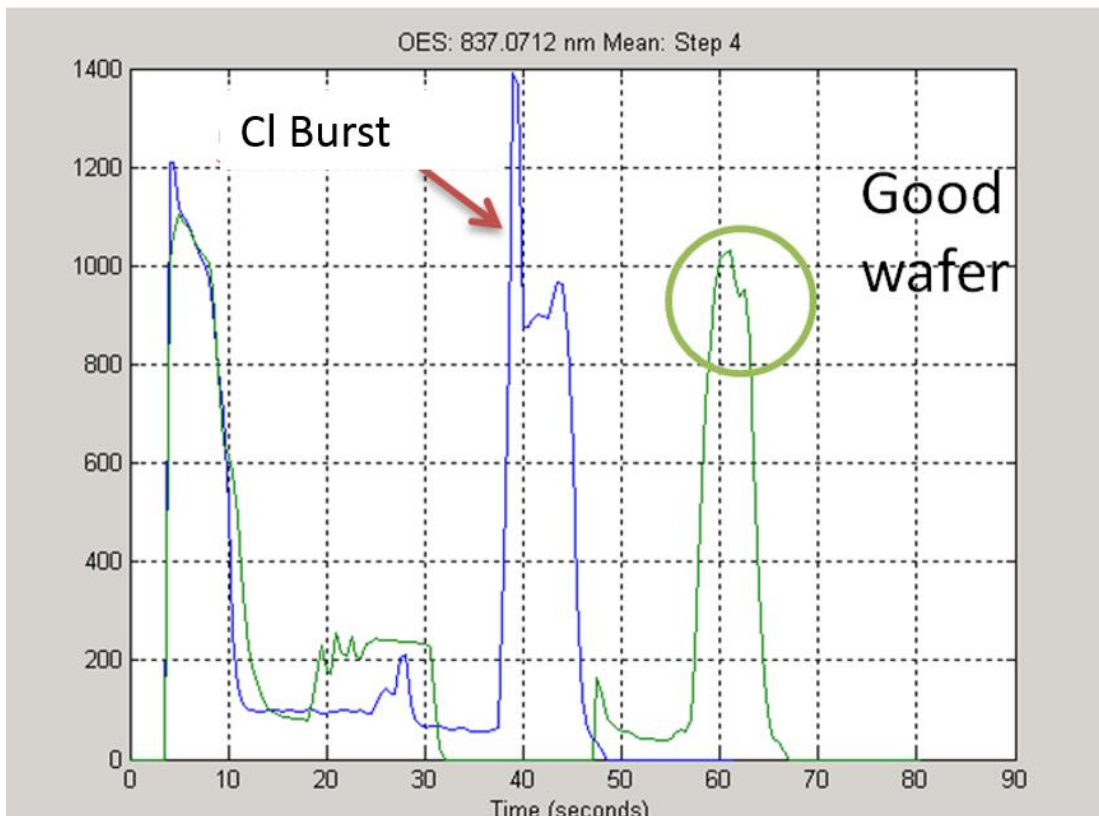


Figure 4-7 The graph displays the temporal behavior of chlorine. The chlorine flow controller is turned on during the plasma. The dynamic behavior of the flow controller’s response is displayed.

The emission spectrum is analysed by recipe step, with the objective of determining which species exists in that recipe step and how they behave temporally and interact with each other. This analysis provides key information about the reaction rates in the plasma as the wafer etches, and the influence the chamber walls and the wafer itself have on the plasma chemistry. The approach is to consolidate the entire spectrum down to a subset of wavelengths that is representative of the chemistry of each recipe step.

A number of different techniques have been developed to investigate the dynamic behaviour of the recipe.

Recipe step 1 of the process is most heavily influenced by the condition of the chamber walls due to the fact that only 2.5% of the total gas flow is SF₆ at a pressure below 1 Pa (97.5% Helium). Therefore, residual by-products from the chamber walls play a significant role in the process chemistry. As the wafer begins to be etched, the effect of the walls begins to become less significant as species that were initially outgassing may be superseded by deposition on the walls and/or the memory effect of the wall wears off. As described in section 4.1.3 an in-situ wafer clean is performed between each product wafer. The chlorine, hydrogen bromide and oxygen chemistry of the in-situ clean leaves a residue on the chamber walls.

A relatively simplistic visual approach illustrated in Figure 4-8 where the spectrum at the end of step 1 is subtracted from a spectrum at the beginning of the step. The difference between the spectra can be used to identify what species are increasing or decreasing as step 1 proceeds. Positive peaks show wavelength increases across the step, while negative values indicate peaks decreasing. The time series for wavelengths 288 nm and 837 nm is also displayed in Figure 4-8 (b).

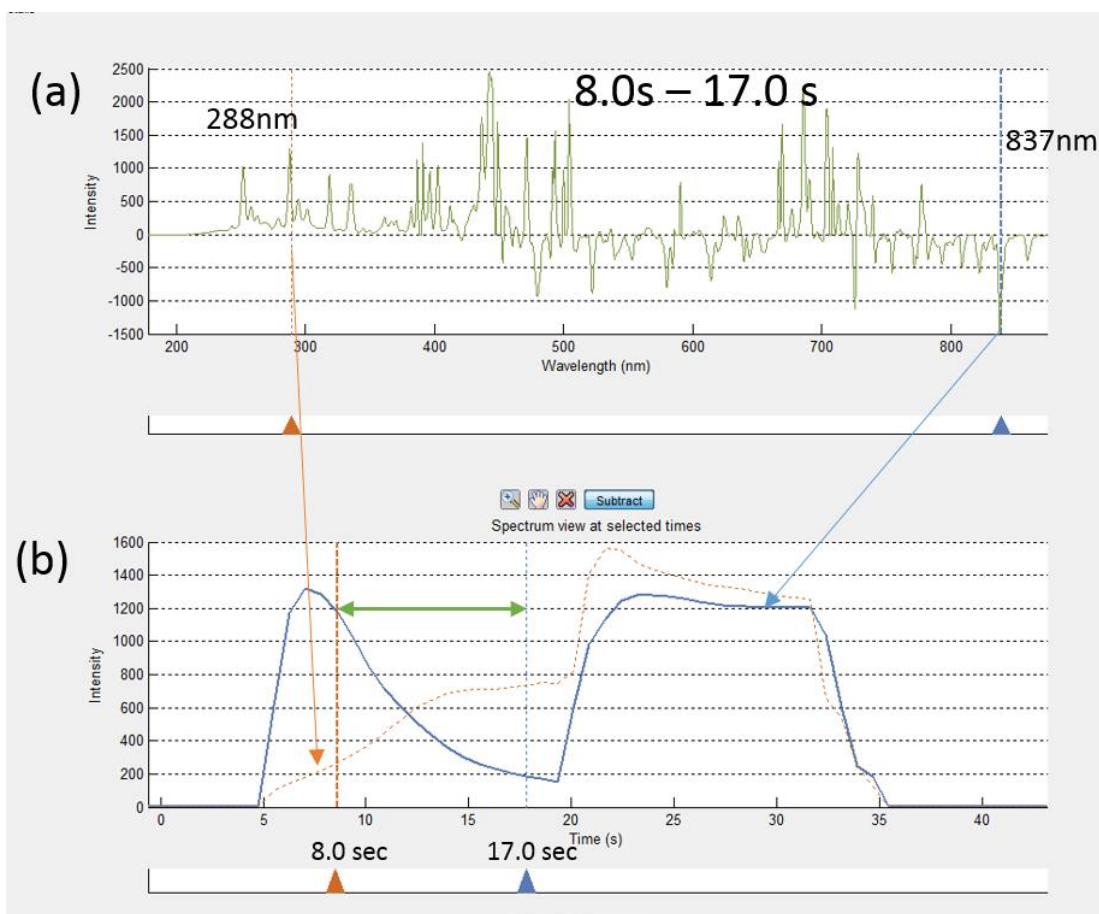


Figure 4-8: The change in spectrum across step 1 of the process shown in (a) and how this can be used to determine wavelengths increasing and decreasing within the recipe step (b).

4.2.2 Approach for atomic and molecular species identification

Additional validation is required before a wavelength can be assigned to a gas gaseous species. In the cases where wavelength peak is unique, with no close neighbours influencing the peak height, the assignment is straightforward by reviewing the literature and examining line peak structure. In Figure 4-9 837.6 nm, a

Cl peak has insignificant contributions from other neighbouring species and is suitable to represent a chlorine emission.

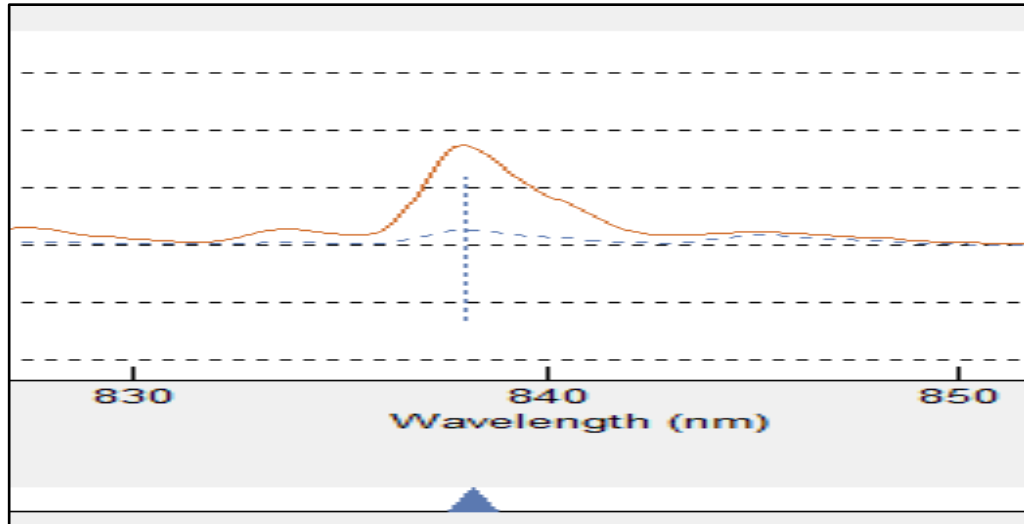


Figure 4-9: 837 nm Chlorine peak red (7 sec, blue17sec) in step1 of the recipe

Identification of other peaks in the spectrum is not always straightforward and requires closer analysis of both the spectral shape and the temporal shape over the recipe step. In the analysis of step 1 of the recipe, significant change is observed across step 1 in a band of wavelengths from 652 to 660 nm. In Figure 4-10 the spectrum for time 7 s, 12 s, and 17 s in the process is plotted in both time domain and frequency domains. The OES spectrum is difficult to resolve into individual species because there is significant overlap in the emission lines. In Figure 4-12, a high

(HR4000) and low resolution (USB2000) spectrum are displayed for the process recipe along with a pure chlorine and pure hydrogen bromide plasma. The low resolution spectrometer shows a distinct peak at 656 nm, however the non-symmetry of the peak structure indicates additional peaks in the region of 653 nm. In the high resolution spectrometer smaller peaks are identified at 653 nm and 654.5 nm. From the NIST database these peaks are identified as Cl and Br emissions respectively. The spectrum from a pure chlorine discharge and a pure hydrogen bromide discharge are displayed in Figure 4-11. These individual gas plasmas help give some indication as to the intensity and shape of the emission lines of Cl and HBr in that part of the spectrum and indicate that H emissions dominate in this region.

For the purposes of the analysis of the 656.3 nm peak can be used to give an estimation of the density of hydrogen in the recipe. Changes in Cl or Br will have little effect on the intensity of the hydrogen line 656.3 nm, except in their impact on the EEDF. More suitable lines exist in the spectra to give estimations as to the density of bromine. As shown in Figure 4-9, 837.6 nm is a more suitable line for estimating the density of Cl.

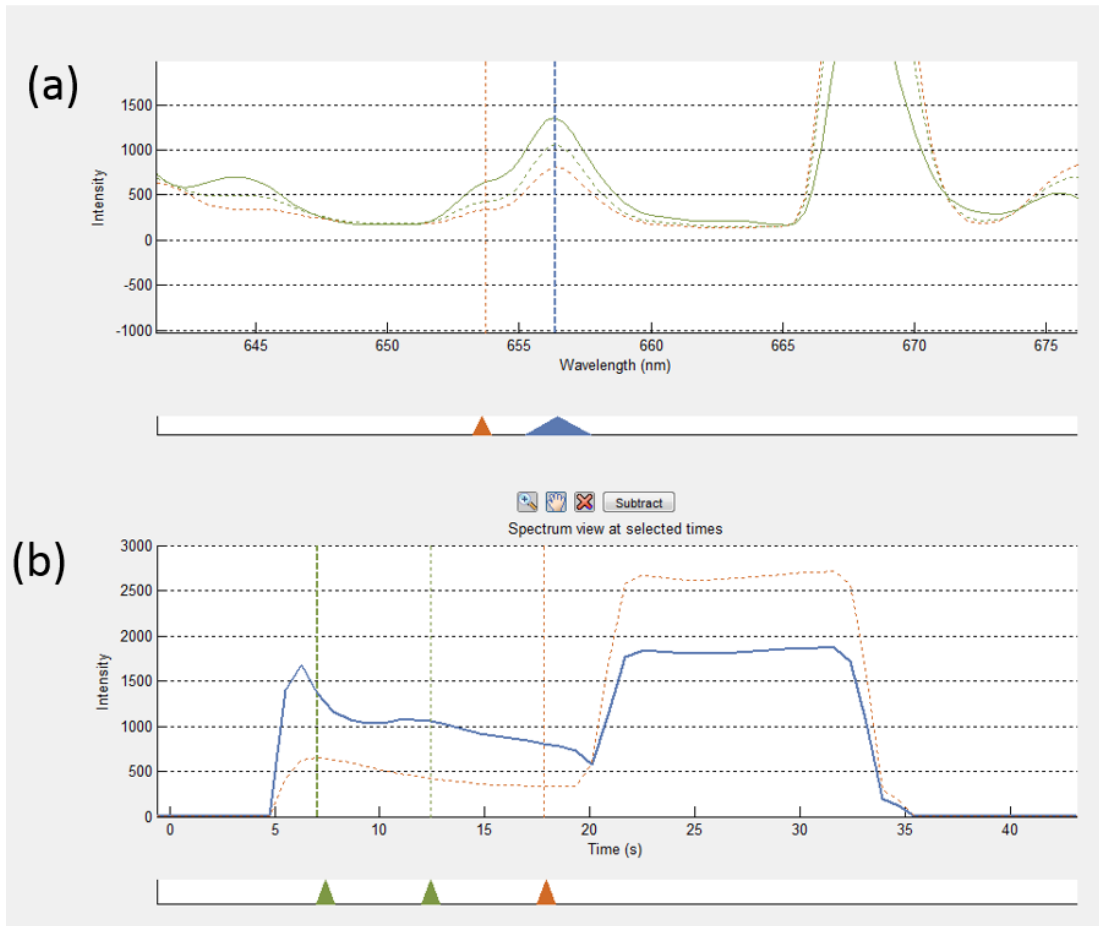


Figure 4-10: shows the peak structure for 656 nm and 654 nm (a) and also the time series traces for the same wavelengths in (b).

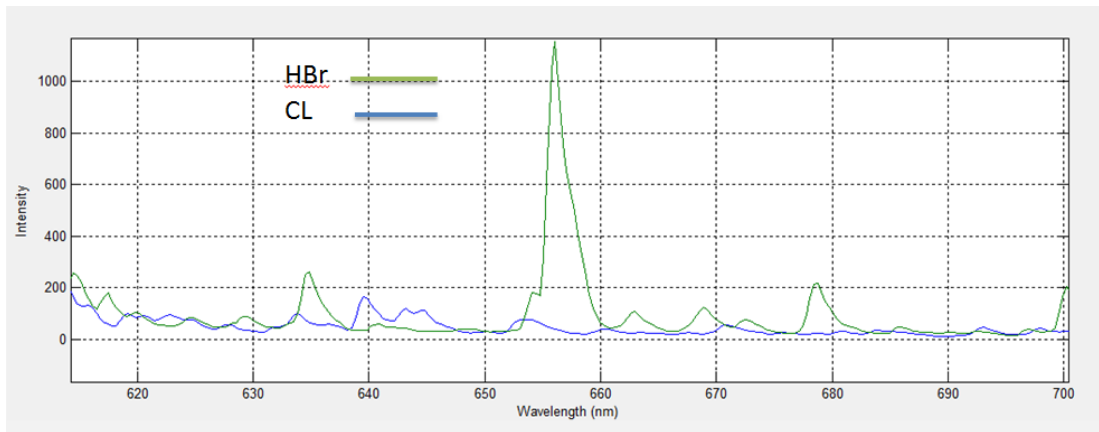


Figure 4-11. Individual spectra shapes structures of Cl_2 and HBr discharges run independently.

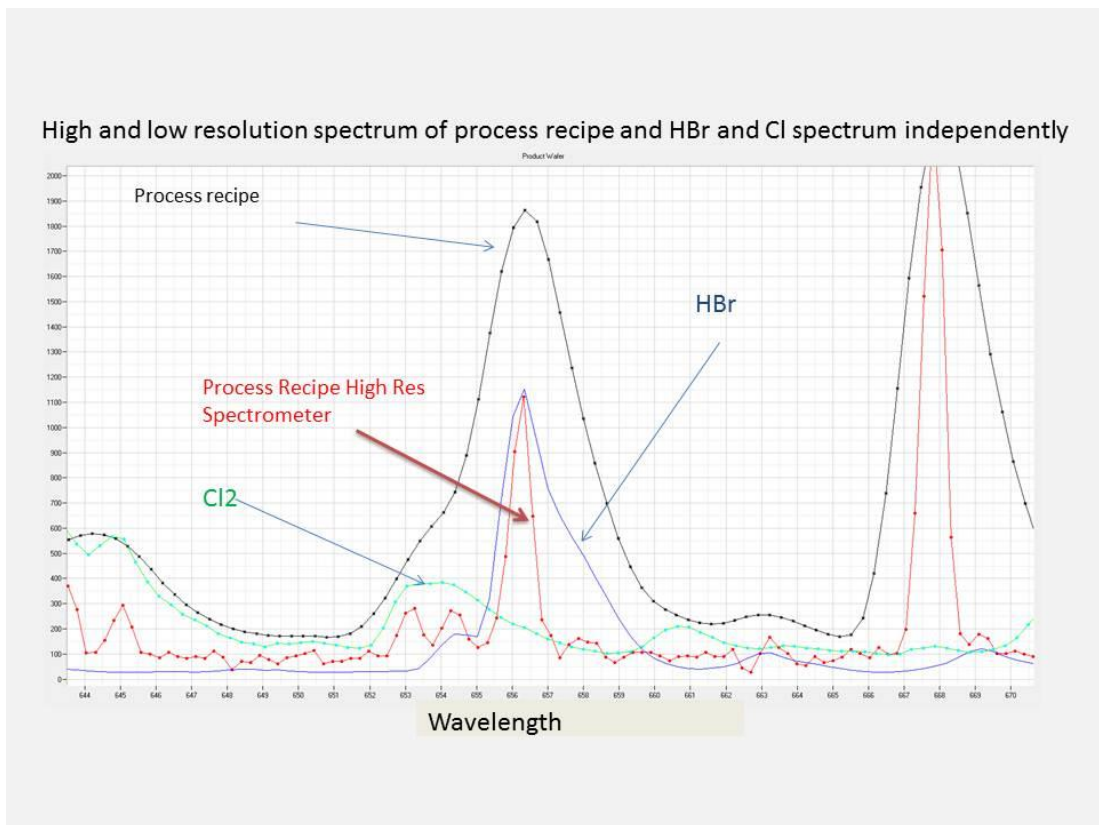


Figure 4-12. High and Low spectrum resolution spectra.

4.2.3 Principal component analysis of time series OES spectra

PCA is especially useful when dealing with OES data, which is continuous and where much of the data is highly correlated. In addition, there are also large differences in the data due to a large number of different atomic and molecular species and different temporal behaviours as reaction rates occur as the wafer is processed. The other advantage of PCA is that once found, these patterns can compress the data and reduce the number of dimensions with little or no loss of useful information. PCA is performed on all the spectrum lines for the entire time series data for 25 wafers. This is especially useful when visualizing the data for interpretation. In Figure 4-13 the first three principal components of the OES spectra for step 1 of the wafer are displayed. The three-dimensional graph displays an overview of the variability in the data and each point represents an observation at a point in time in the recipe step.

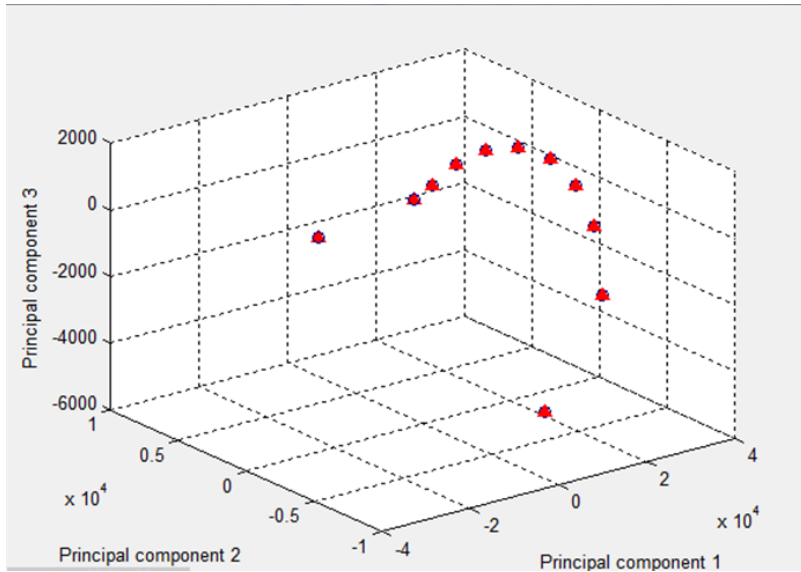


Figure 4-13 Three principal components of Step1 Time series data. Each point represents a time point in step 1 of the process.

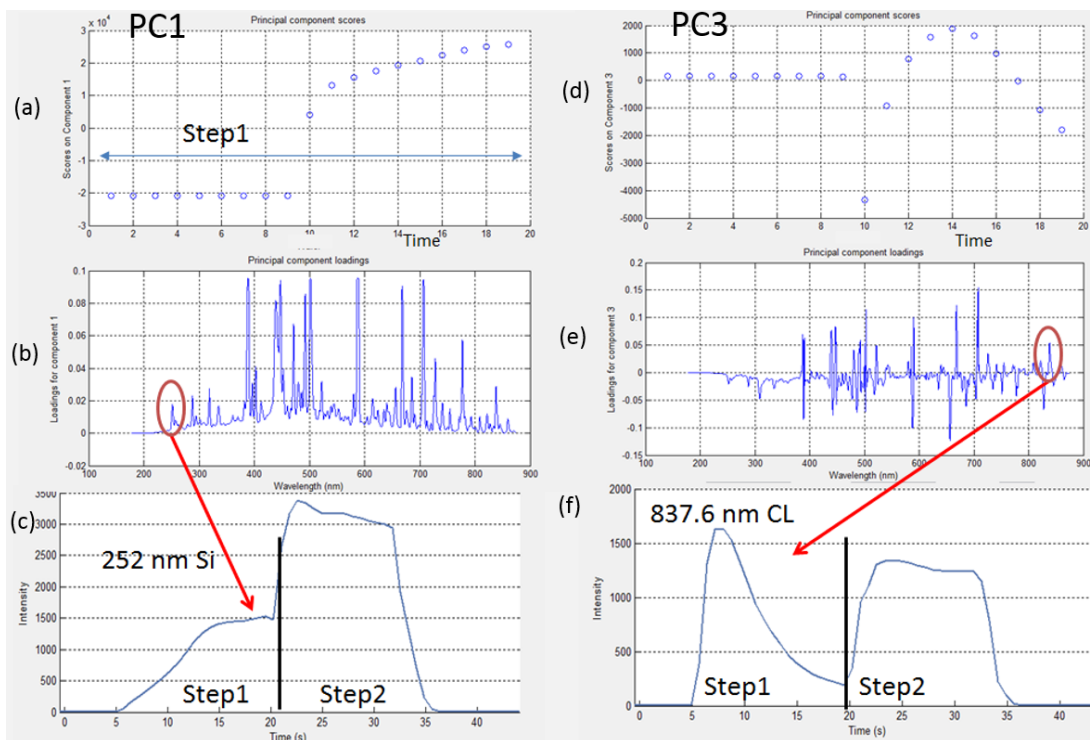


Figure 4-14 PCA of time Series spectral data for recipe step 1. Displayed is the scores (a, d) and loadings (b, e) for the 1st and 3rd components. The loadings help identify spectral lines patterns. Si and Cl lines are shown in the (c, f).

A description of principal component analyses is given in Chapter 3.4.2 In Figure 4-14 principal component (PC) 1 and 3 are displayed with the scores and loadings. PC1 represents the main variations pattern where intensities slowly increase after 9 seconds when the plasma is turned on. This is reflected in the scores chart for PC1. The loadings shows the most influential wavelengths that are most correlated with that pattern. These are displayed in the loadings chart below. Wavelength 252 nm (Si) is easily seen in the loadings chart. The actual behavior of the 252 nm line is displayed below the loadings chart. This pattern is highly correlated to the pattern of PC1. PC3 shows has a completely different pattern and is displayed along with 837.6nm (Cl) which can easily be identified again from the scores chart.

PCA is a very efficient technique in identifying patterns within the data set and when applied to OES data, the analysis can identify the temporal behavior of key chemical species in the plasma.

In addition to identifying the structure of the data within one wafer, PCA is also very useful in comparing wafers. Figure 4-15 gives a 3D graph of the first 3 components for a 25 wafer lot. The difference observed between wafers 1 and 2 is as a result of chamber seasoning across the lot as well as chamber heating.

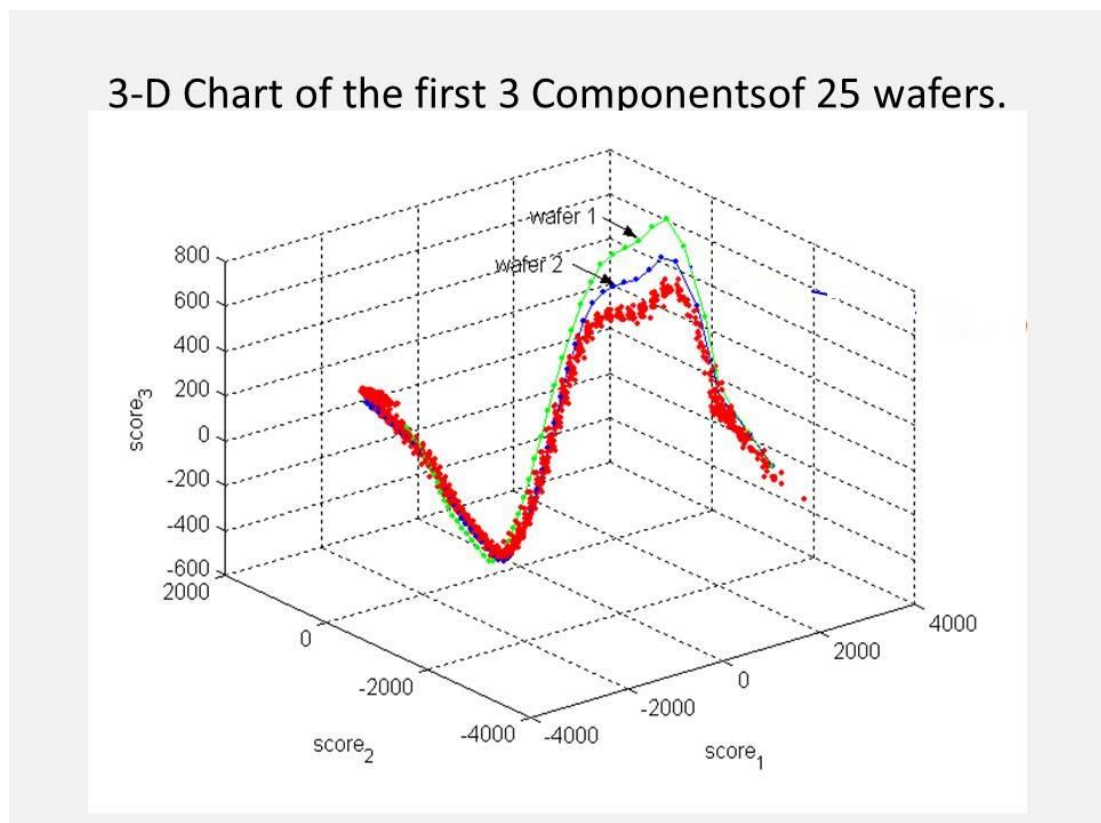


Figure 4-15 displays the principal components for 25 wafers. Wafers 1 and 2 are clearly distinguished from the rest of the wafers in the lot (red)

4.2.4 Spectral clustering

One disadvantage of PCA lies in interpreting the results of dimension reduction analysis. A reason why we need to normalize before calculating the principal components is to mitigate the effects of scale. For example, if the intensity of one of the wavelengths is orders of magnitude higher than the others, PCA tends to assign the highest amount of variance to this wavelength and thus bias the results of the analysis. By normalizing the data, we can reduce this effect. However, normalizing results means spreading the influence across many more principal components, so that more principal components are required to explain the same amount of variance in data. The interpretation of the PCA results can become more difficult.

A second tool for OES analysis is by so called data clustering. In this approach all of the wavelengths for the entire sample spectrum are correlated with each other and where the correlation is above a certain threshold they are clustered together. The data can be pretreated by being mean centered and normalized to unit variance or left in raw form. In addition, each wavelength over the entire recipe time is filtered for noise using a Kalman filter.

Figure 4-16 shows the results of clustering the time series data of step 1 of the process. Identifying the atomic or molecular species attributable to that cluster requires closer inspection of the cluster members. In Figure 4-17 an in-depth examination of the cluster structures and where the correlated spectral lines appear in

the spectrum is necessary to determine what species can be attributed to the cluster shape. As discussed earlier, distinct peaks are necessary to definitively determine the species. The objective of the clustering technique is that it allows the discovery of all time domain patterns within the data set. These time domain patterns presented in Figure 4-17 Figure 4-7 give information on how the species are changing as the wafer is etched.

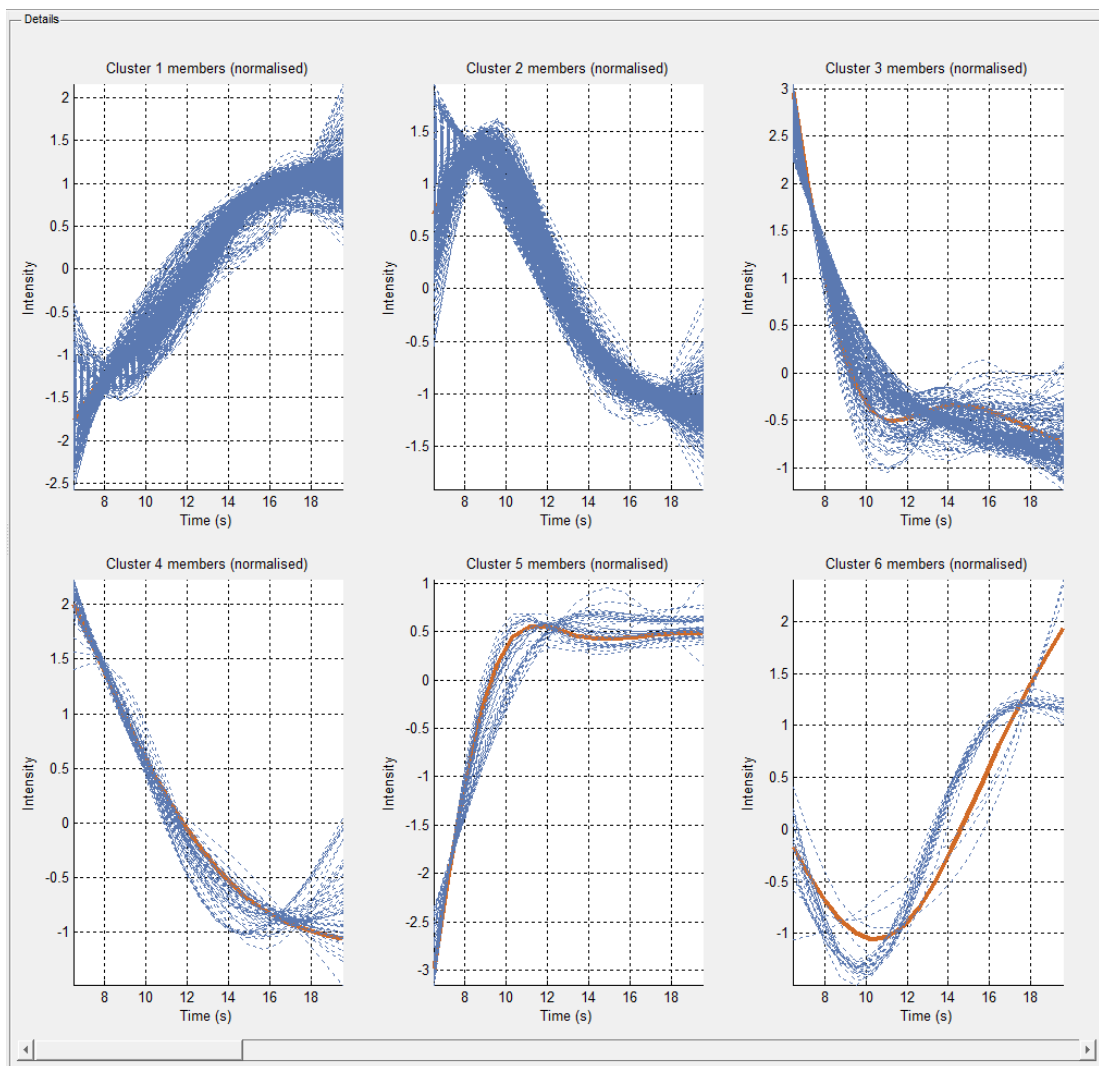


Figure 4-16. Six clusters per step one of the process. Oranges the centroid with members in blue. Correlation threshold set at 0.9

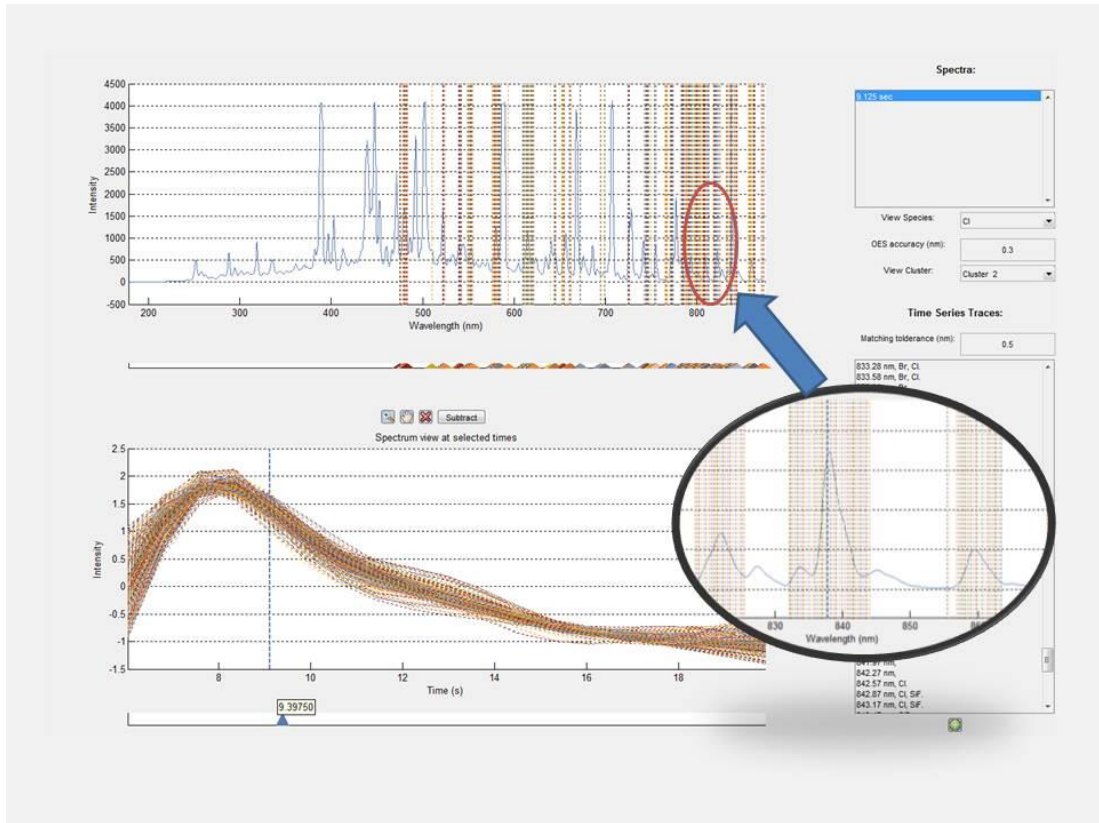


Figure 4-17: Exploration of the members of the cluster involve viewing where they appear on the spectrum. In this example clustering has identified a number of distinct peaks whose behavior across the step is depicted the bottom graph.

4.3 Virtual metrology - etch rate estimation from sensor data

This section describes the development of a machine learning technique to estimate the etch rate from the OES data. Gradient boosting tree (GBT) and linear modelling techniques are used with feature selection and peak-finding algorithms to predict etch rate from the OES spectra. The GBT model also gives diagnostic information about

the top predictors for the metrology variation. The validity of these predictors is validated through the analysis of the composition of the deposition on chamber walls, which is known to contribute to the etch rate variation. Excursions in etch rate is also investigated and again validated with experiments.

4.3.1 Data reduction and modelling approaches

A number of different approaches were used to investigate the cause of the etch rate variation seen in Figure 4-18. Two data reduction techniques, feature selection and peak detecting are employed in combination with two correlation approaches, GBT and ridge regression.

The spectral data contains 2048 data points corresponding to the number of pixels in the USB2000 spectrometer used in this work. The time series data was summarized by two statistics, mean and standard deviation for both process steps. This resulted in 8192 parameters for each 1772 observations (wafers). Two approaches are used to reduce the data set. A peak detection routine was performed on the data to return only the significant peaks from the original spectra. The data size is reduced from 2048 to 190 wavelengths (peaks). A feature extractor algorithm is also used on the original data. The objective of this technique is to find the most important variables that affect the response or etch rate. This supervised approach needs a response, such as etch rate in this case, in order to identify the important wavelengths.

A gradient boosting tree (GBT) and the linear model which are detailed in Chapter 3.4.3 were used to analyse the data. 70% of the data was randomly selected and used to build a model. The remaining 30% of the data was used then to test the model. The predicted response for 30% data set was then compared to the actual response. To quantify the effectiveness of the model ability to predict etch rate, the standard deviation of the difference between actual and predicted etch rate. The results are displayed in the Table 1 for the different modelling scenarios.

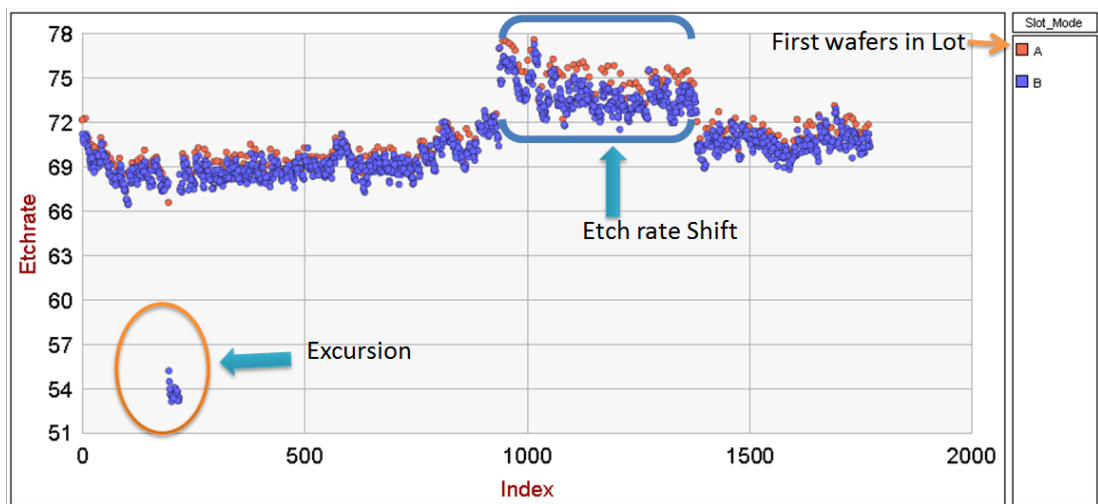


Figure 4-18: Etch rate performance in $\text{A}^\circ/\text{sec}$ of chamber of period of 4 months in which 6000 wafers were processed and 1700 of these wafers had metrology measurements.

Three areas of etch rate variation were examined. The first is the excursion that occurred and is highlighted in Figure 4-18. Here the etch rate performance of the chamber shifted dramatically down for a 25 wafer lot. The second is that after 900 wafers the etch rate shifted up for a period of about 400 wafers. A first wafer affect is evident in Figure 4-18 where the first wafer in the lot is colored red, referenced A.

Gradient boosting trees has the advantage of not requiring any prior feature selection and are able to handle a very large numbers of input parameters. Also, being a nonlinear algorithm technique, it is suitable for a wide range of responses. Feature selection was also performed as a reduction method. Due to the large number of input parameters relative to the number of observations, linear modeling could not be performed without some data reduction methods. Feature selection and the peak finder routines were used as data reduction methods. The output from the feature reduction was analyzed with a GBT model and a linear modelling technique. The results are displayed in

Table 1. A number of different scenarios were evaluated using all the input parameters and the output from the peak finder routine. The data with and without the excursion was also modeled. The weighting the model assigns to each variable (variable importance) is one of the most useful outputs from the data modeling. From a process diagnostics perspective, knowing the top predictors of the metrology variation provides key information about the root cause of the process variability. In addition to evaluating the error performance of the models, the top predictors were analyzed to see how well they correlated with the metrology variation.

Table 1: Error from different algorithm testing on all the data and the reduced peak file. The error is defined as the mean standard deviation of the observed-predicted.

Model	All Peaks Test Error	Peak file Test Error
GBT	0.68	0.76
GBT with FS	0.75	0.71
Linear (FS)	0.75	0.63
GBT with no Excursion	0.68	0.75
FS and Linear Model	n/a	0.64
argon Excursion		
GBT	0.76	0.82
GBT FS	0.71	0.76
Linear	n/a	0.60

4.3.2 Gradient boosting trees results

As described in the previous Chapter 3.4.3 the GBT method requires a large number of training observations and is well-suited to a very high number of input parameters. The model performed very well in dealing with the very large number of input parameters. The important variable parameters need to be examined in detail in order to determine if they are simply correlated with the metrology or whether they are causal. The distribution of the residuals (predicted-actual of the etch rate) is an important indicator in the evaluation of the model validity. The residuals should be normally distributed around zero with no systematic variation. The residuals behaviour across the data set is also reviewed, this gives an indication of how well the model behaved over the 1700 wafers. The results of the modelling using GBT are shown in Figure 4-19.

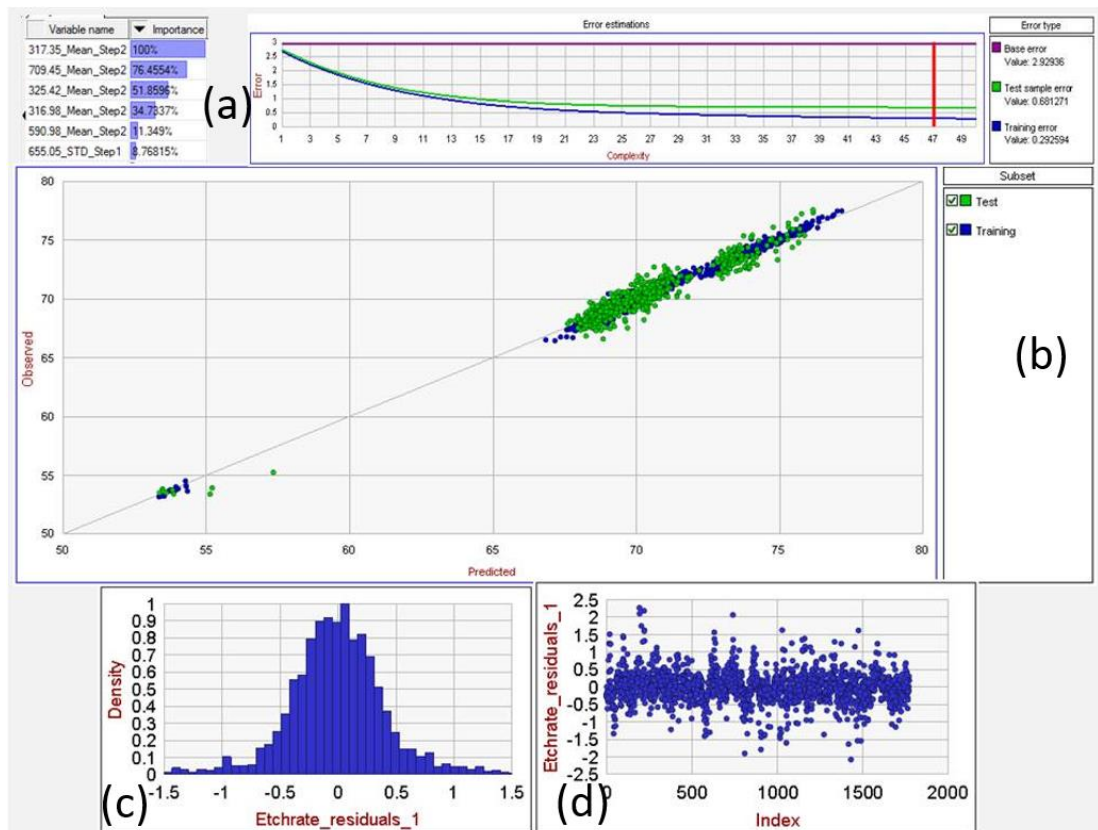


Figure 4-19: Output from GBT model showing the test error, the variables importance and the performance of the prediction and residuals.(a) shows the variables of most importance in the prediction, (b) predicted versus observed, (c) and (d) shows the distribution of the residuals.

The model ranks the variables in order of importance in explaining the variation in the response (etch rate). This information is extremely useful in understanding the behavior of the chamber with respect to the etch rate variation. The variables in this data set are spectral wavelengths which can be mapped back to the atomic or molecular species present in the chamber. Knowing the important wavelengths that contribute to the change in etch rate provides key information for process diagnostics. However, given that this is a black box modeling technique, interpretation of the wavelengths is necessary before conclusions can be drawn from the results of the modeling. In Figure 4-19 wavelength 317.4 nm of step 2 of the

recipe was ranked as the most important variable by the GBT algorithm in predicting etch rate meaning it is highly correlated to the etch rate. In order to determine what species 317.4 nm represents in the discharge, the spectral and temporal behavior must be reviewed. In Figure 4-20: 317.4 nm is plotted versus etch rate and also in processing order. In addition, the optical spectrum is also shown for several wafers identifying where 317.4 nm is located in the spectrum. Spectral 317.4 nm does discriminate reasonably well the shifts in etch rate. However, on close inspection of the spectral graph 317.4 nm is not a peak and cannot easily be assigned to a single atomic or molecular species.

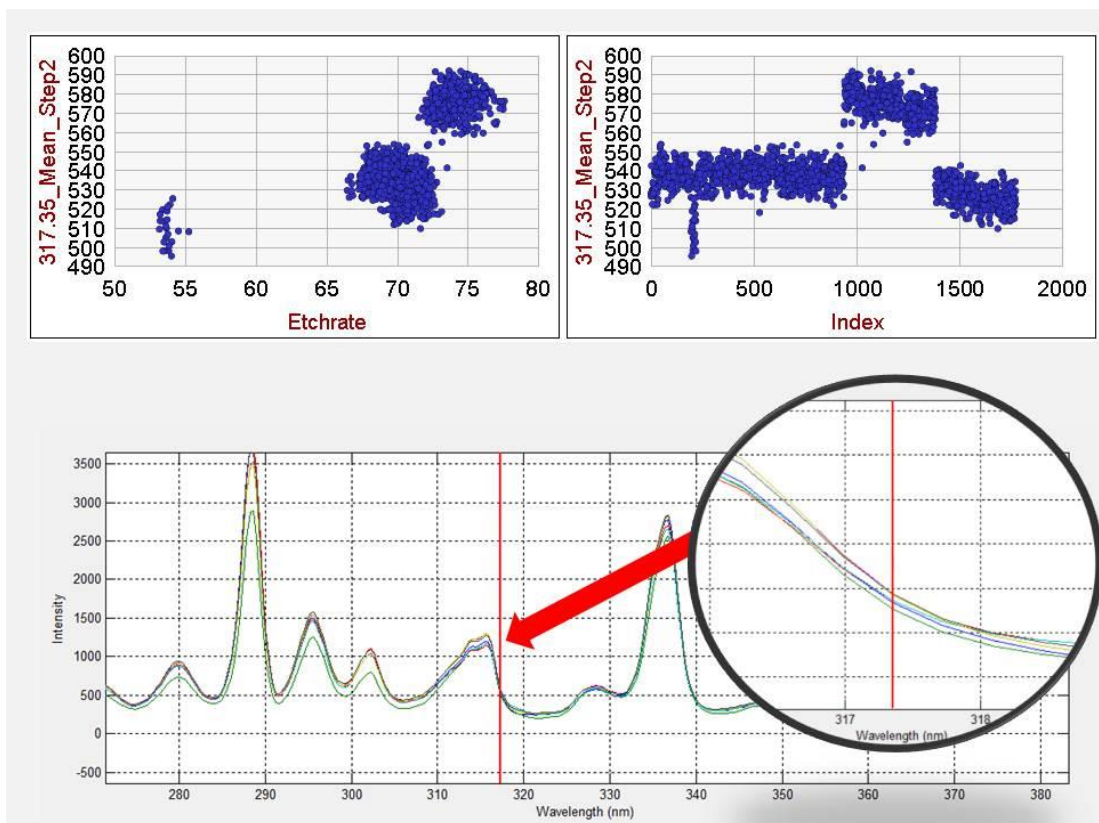


Figure 4-20: The relationship between the etch rate and 317.35 nm.

Further investigation is required into the 317.4 nm peak in order to determine if there is valuable information in this parameter. In Figure 4-21 the average spectrum for step 1 and step 2 are displayed as well as the time series data for the peaks surrounding 317.4 nm. Step 1, which is a He/SF₆ chemistry has a helium peak at 318.8 nm. Given that helium is inert and has little interaction with the chamber walls, it is shown in Figure 4-21 to be quickly pumped out at the end of the step. There is a plasma-on transition from step 1 to step 2 in which both the microwave power and pressure change significantly as well as a transition from He/SF₆ to NF₃/Cl/Ar . The 'plasma-on' transition has the advantage of reducing the overall recipe time. However, the process performance can be significantly impacted by the dynamic behavior of the flow, power and pressure controllers. This dynamic behavior is very important when it comes to matching chambers process performance in large semiconductor fabs as discussed previously.

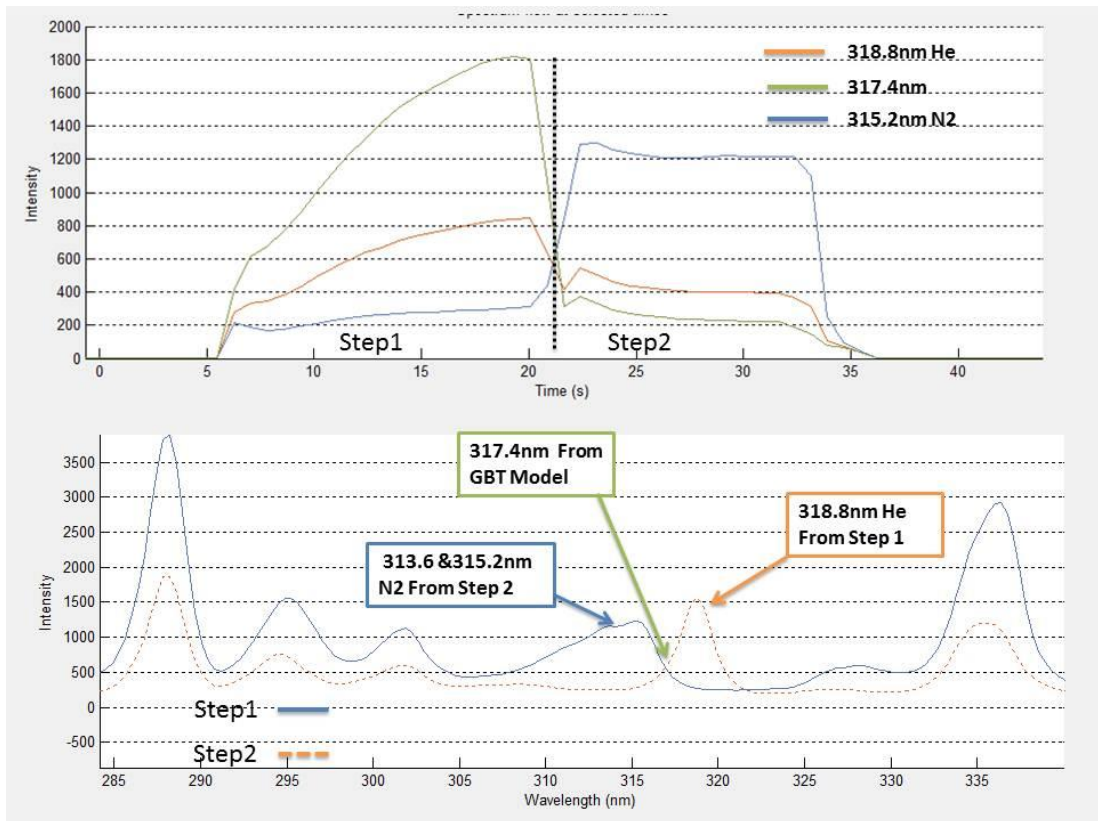


Figure 4-21: 317.3nm wavelength that the GBT Model classed as correlated variable to etch rate. Upper graph shows the temporal behavior of the wavelengths. Lower graph is the mean spectra from Step 1 and 2.

Reviewing the data in Figure 4-21 concludes that there is no easily determined physical meaning to the 317.4 nm peak in this recipe. While there is some correlation with the metrology, it is inconclusive what species it represents.

The same methodology is applied to the next parameter the 709.6 nm peak mean Step 2 from the GBT model. The results are displayed in Figure 4-22. The correlation to metrology is much stronger. However, inspection of the spectrum data shows that 709.6 nm is on a shoulder and is not truly a peak. This peak saturation is as a result of the trade-off in the integration time of the spectrometer enabling it to measure spectra over a wide range of microwave power and input chemistry settings.

In step 2 of the process, the high microwave power coupled with argon resulted in many saturated argon peaks. The emission spectra for argon in this regime produces very bright spectral lines. The argon emission line at 706.7 nm is saturated. However, some of the light at that wavelength would be picked up by neighboring pixels resulting in a very broad emission band. With no other spectral emissions on the high end of this band it can be appropriate to use the edge of the spectral band as a measurement of the argon density. In addition, the root cause of the etch rate shift up which was observed at wafer 900 was caused by an intervention on the chamber whereby the argon MFC's calibration was adjusted deliberately. This validates the results from the GBT model. The excursion wafers will be discussed later in the chapter in section 4.3.4.

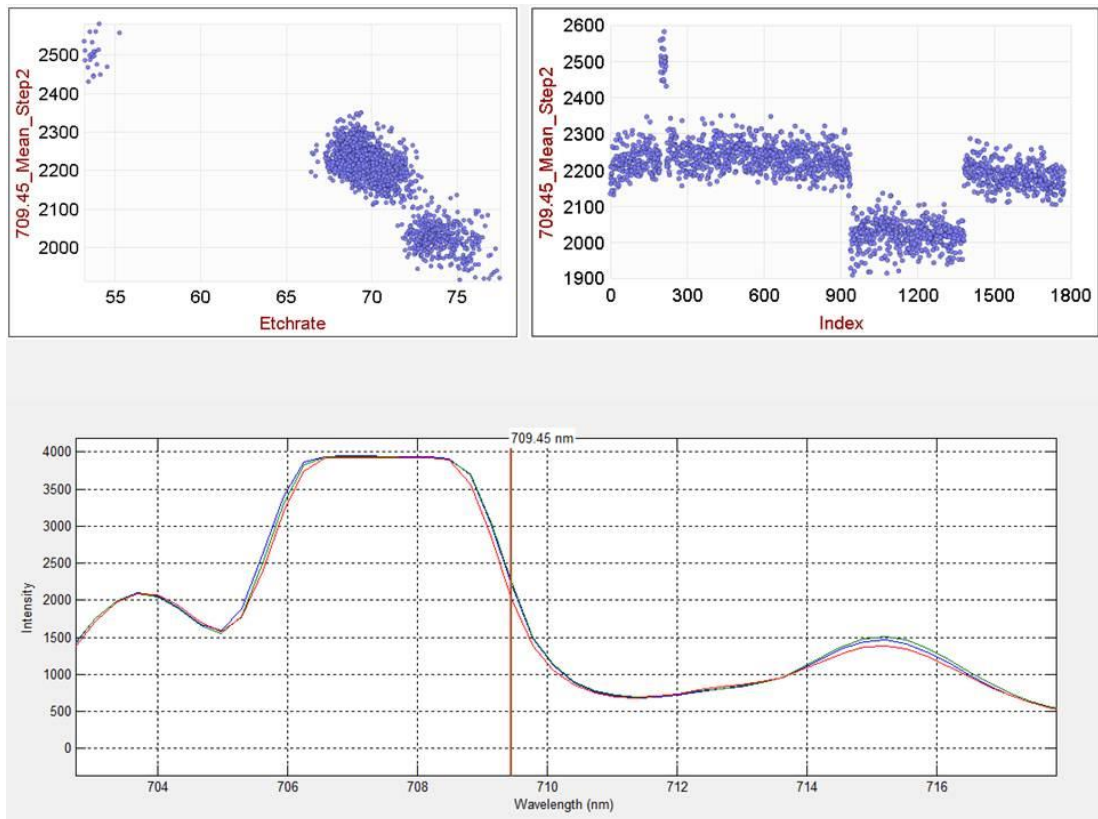


Figure 4-22: The output of the gradient boosting tree analysis. The algorithm ranked 709.45 nm in step 2 is one of the most important variables for determining etch rate.

4.3.3 Analysis of the first wafer effect

Significant effort is made during process development to ensure reproducibility across all 25 wafers in a production lot. These plasma cleaning strategies can be counterproductive or complementary depending how they are engineered. As discussed previously in the section 4.1.2 , a $\text{Cl}_2/\text{HBr}/\text{O}_2$ in-situ clean is performed between each wafer. In addition, at the beginning of the lot a pre-clean with SF_6 is performed to reduce build-up on the walls and also to pre-season the chamber before the first wafer is processed. Even with these strategies the etch rate of the first wafer is higher than the other wafers in the lot. In Figure 4-23 the etch rate of 300 wafers by slot position is shown. The box plot highlights the etch rate for slot 1 is 1.3 Å/s higher than the rest of the wafers in the lot. In Figure 4-24 the chart displays the cross lot etch rate variability. Here the variability across the lot can be as much as 2.5 Å/s with most of that variation attributed to the first wafer in the lot.

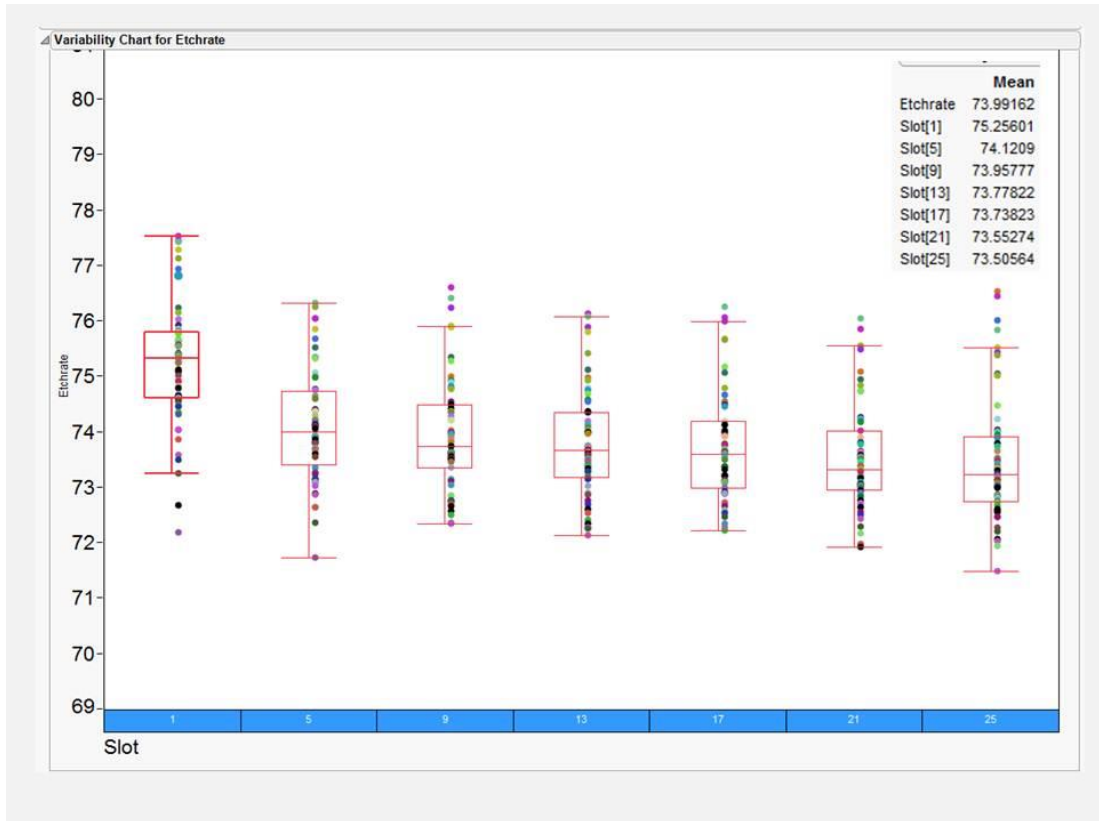


Figure 4-23: A box plots of the etch rate in $\text{\AA}/\text{sec}$ for each of the wafers grouped by slot.

A classification and regression tree (CART) model was constructed to discriminate wafer 1 from the rest of the wafer in the 25 wafer lot. The decision trees are produced based on a set of rules applied to the variables in the data set. The data was grouped into two sets, slot 1 and slots 2 to 25. The algorithm was then used to build a decision tree in order to discriminate between the two groups. The top three variables (318.5 nm (helium), 777nm (oxygen) and 827.3 nm (bromine)) were chosen by the model to discriminate slot 1 from the rest of the slots and the results are displayed in Figure 4-25. The standard deviation of the parameters indicates that there is greater change in these variables for the first wafer step 1 when compared to wafers in slots 2 to 25.

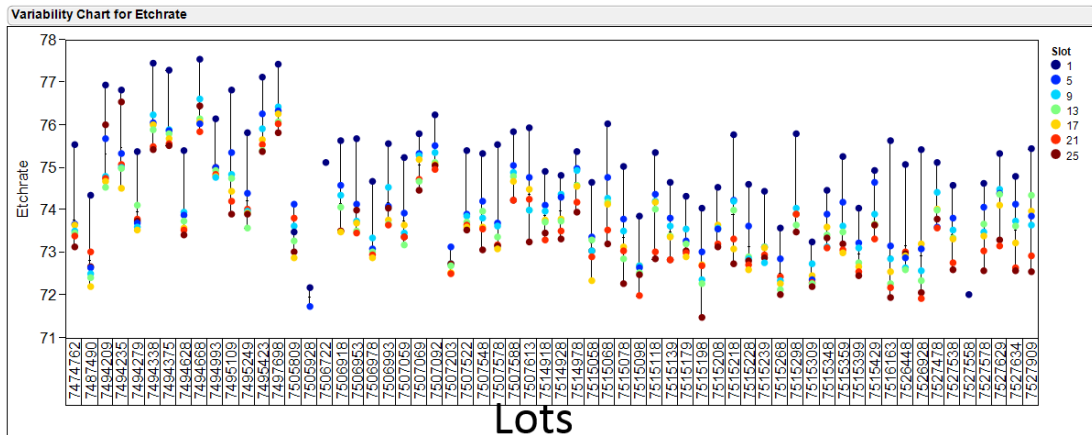


Figure 4-24: Graph displays the etch rate $\text{A}^\circ/\text{sec}$ variability by lot. The colours represent the slot position in the cassette.

The top three parameters that the CART model has identified needs to be further investigated in order to develop a diagnosis for the higher etch rate in slot 1. To do this the time series data from which the summary statistics are calculated is analysed. The model has identified the standard deviation of step 1 for helium, oxygen and bromine but more information is needed before a diagnosis can be made as to the cause of the higher etch rate of slot 1.

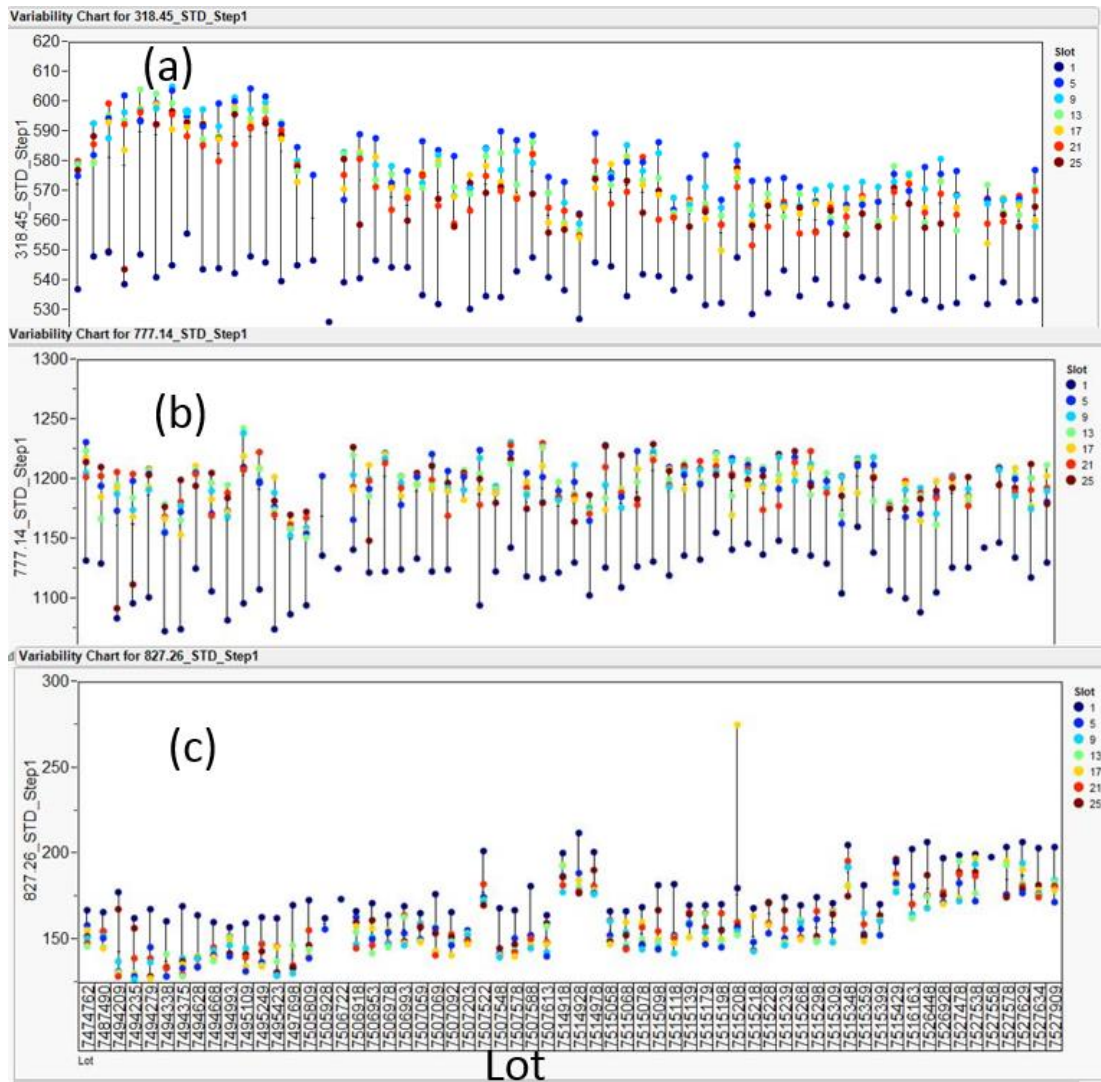


Figure 4-25: The variability graphs of the 318nm (a), 777nm (b) and 827nm (c) all which show to discriminate wafer 1 from the rest of the wafers in the lot.

As discussed earlier in the section 4.1.1 the chemistry for step 1 consists of SF₆/He, where the SF₆ flow into the chamber is extremely low. Hence, the process is heavily influenced by the residual by-product on the chamber walls from the in-situ process of Cl₂/HBr/O etching of silicon. This effect can be clearly seen in figure 4-26 where high levels of bromine and chlorine are present at the very beginning of the process step and decrease rapidly within the first 10 seconds into the step as the wall effect

begins to diminish. With such a low SF₆ flow in the step, contribution from chlorine and bromine as an etchant is quite significant, therefore the consistency of the wall contribution has a significant impact on the etch rate consistency from wafer to wafer. As the CART model indicated, variation in the bromine concentrations in the process has a significant contribution for the higher etch rate of slot 1. Figure 4-26 supports this hypothesis where increased levels of bromine and chlorine are observed for wafer 1 relative to the other wafers within that lot.

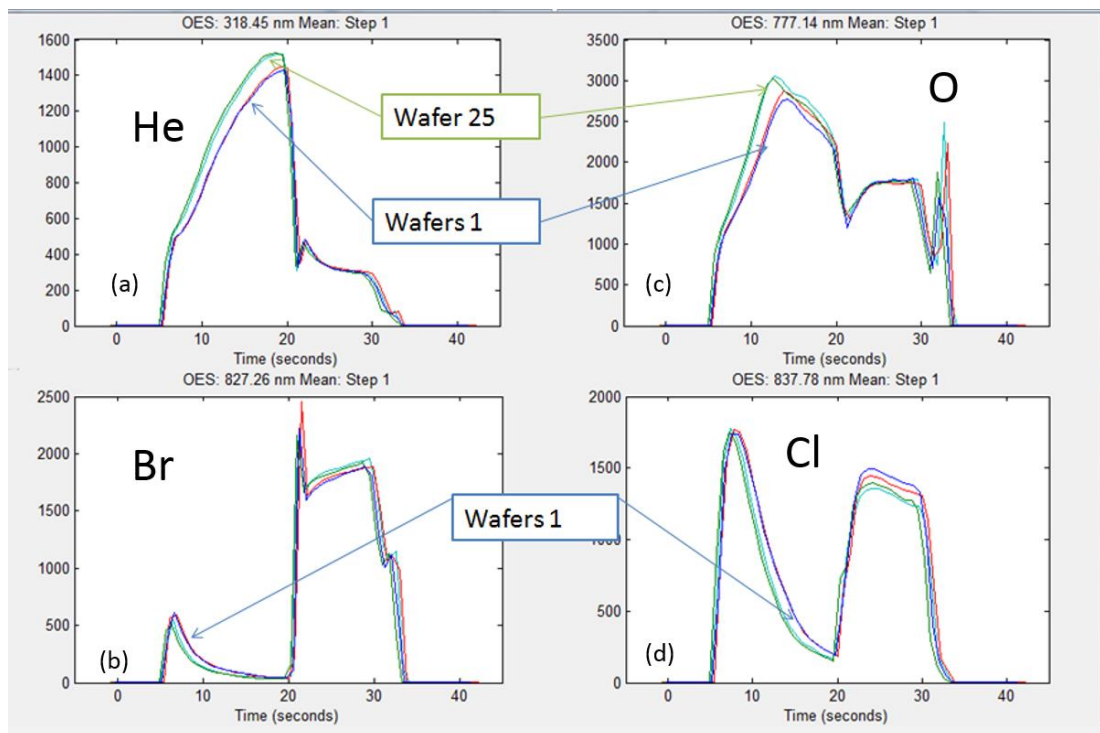


Figure 4-26: The spectra lines identified that can discriminate wafer 1 in a lot from the rest of the wafers in the lot.

One possible reason for the increased levels of bromine and chlorine for wafer one is the fact that at the beginning of the lot a pre-seasoning silicon wafer is processed using an extended SF₆ step which is intended to etch chamber walls removing by-products to prevent chamber flaking causing particles. At the end of that SF₆ step the

chamber is re-seasoned using an in-situ cleaning process ($\text{Cl}_2/\text{HBr}/\text{O}$). The analysis of the OES spectra suggests that the amount of chlorine and bromine emanating from the chamber walls is larger after the preseason wafer. This data indicates that the deposition on the walls is thicker post preseason versus the in-situ clean.

The behaviour of the helium and oxygen spectral lines in Figure 4-27 is not truly representative of their gas densities in the process. The presence of electronegative gases, chlorine and bromine, have a significant impact on the EEDF. Small changes in chlorine and bromine significantly affect density of electrons in the discharge due to electron attachment to electronegative gasses. The density of bromine and chlorine are rapidly falling in the first 10 seconds of the process as shown in Figure 4-26 (b) and (d). This impacts the entire discharge EEDF and the spectral emissions. Therefore, the temporal behaviour of helium and oxygen emission lines is not representative of their gas densities in the process. In particular, helium being an inert gas does not react with the walls or the surface and hence its density should be consistent across the step. However, in 4-26(a) the 318.5 nm emission line is observed to be increasing over the duration of the step. This is most likely due to the fact that as the density of bromine and chlorine reduces, there are more electrons available to cause excitation of the helium. The source of oxygen in this step must again be from the walls as there is no oxygen flow in the recipe. The 777 nm line emission line is also affected by the behaviour of electrons. In this case the oxygen density is believed to be decreasing across the recipe step and this can be observed after 15s, when the impact of the chlorine and bromine begins to decrease, yet the residual oxygen can still be seen to be decreasing until the end of the step.

To test the hypothesis, an experiment was conducted whereby no in-situ cleaning was performed between each wafer. With no in-situ cleaning the source of Cl and Br on the chamber walls is removed. The results are displayed in Figure 4-27 which, as expected, chlorine and bromine emissions are absent. The helium 318 nm line is consistent throughout the step as expected. The 777 nm line representing oxygen is also consistent throughout the step. While the contribution of oxygen from the wall is minimized, its presence in the discharge is most likely resulting from the etching of quartz components in the chamber. The experiments shows that when there is no residual Cl or Br outgassing from the chamber walls the He emissions are constant across the step, where in the presences of the Cl and Br outgassing the He emissions are impacted by the influence the Br and Cl presence.

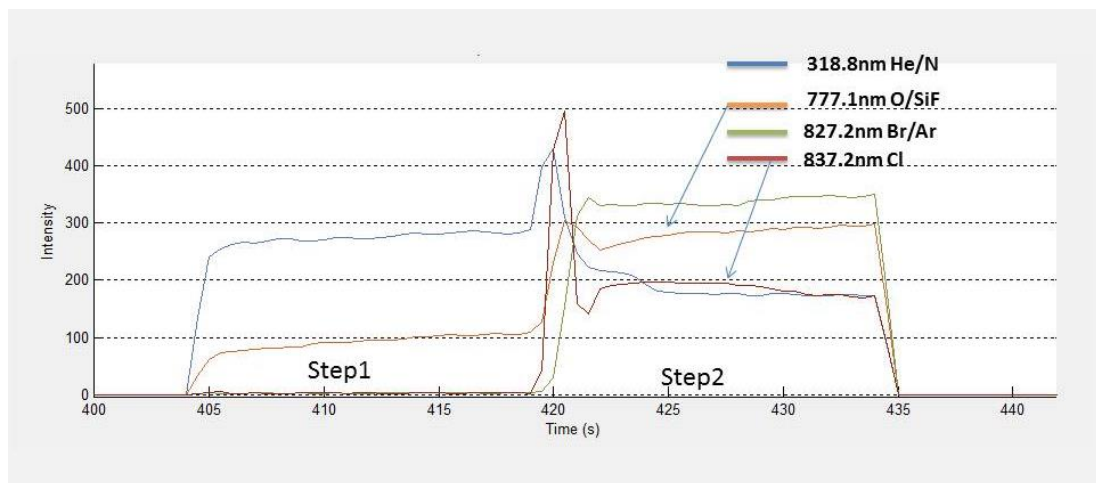


Figure 4-27: Graph of production wafer spectra where no in-situe wafer was processed. No Cl or Br is evident in step 1 of the process.

4.3.4 Excursion investigation

Within the data set, described previously within the section 4.1.7, there is a 25 wafer lot where the etch rate dramatically dropped by 20 Å/s. This excursion is highlighted in Figure 4-18. PCA is performed on the OES data independently for each process step. The PCA analysis can be performed on all process steps together, however this makes the interpretation of the results more difficult. Figure 4-28 displays the first two components (PC) of the OES spectra for step 1 mean. 47.2% of the variability is explained by the first principal component, PC1. PC1 lies along the line of greatest variation and tries to capture the shape of the variation of the data. Each wafer may now be projected on this line in order to get a coordinate value along the principal component line. This new coordinate is known as the score and is plotted in Figure 4-29. From the graph the excursion can be clearly identified as having large scores relative to the rest of the wafers. This is to be expected as the method captures the variation in the “normal” wafers and as there are only 25 excursion wafers they have limited impact on the model.

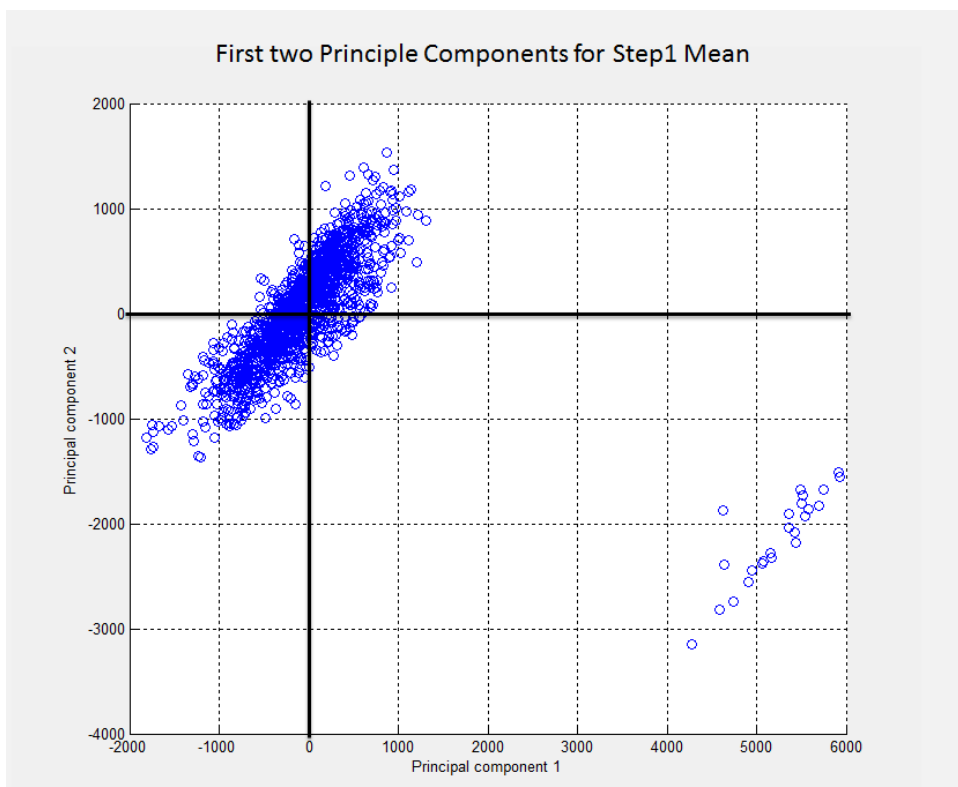


Figure 4-28: The first two principal components plotted against each other.

The loadings show the relationship between the original variables and the principal components. The loadings inform how the variables are linearly combined to form the scores. They unravel the magnitude and manner, positive or negative correlation, in which the variables contribute to the scores. In analyzing the loadings for the OES spectra, the results are best displayed as a computed spectrum so as to retain some of the peak structure and enabling important wavelengths to be more effectively determined. In Figure 4-29 the scores and loadings for PC1 are displayed. The wavelengths of importance for the PC1 are easily determined from the loadings chart. The objective again is to determine reasonably isolated peaks so as to be able to assign them to a specific atomic or molecular species. Since PC1 is representative of the normal wafers in the data set, picking atomic or molecular species from the

loadings chart would only be representative of those normal wafers. The approach taken was to determine some meaningful wavelengths that are representative of normal behavior and compared normal wafer wavelengths to the excursion wafers wavelengths.

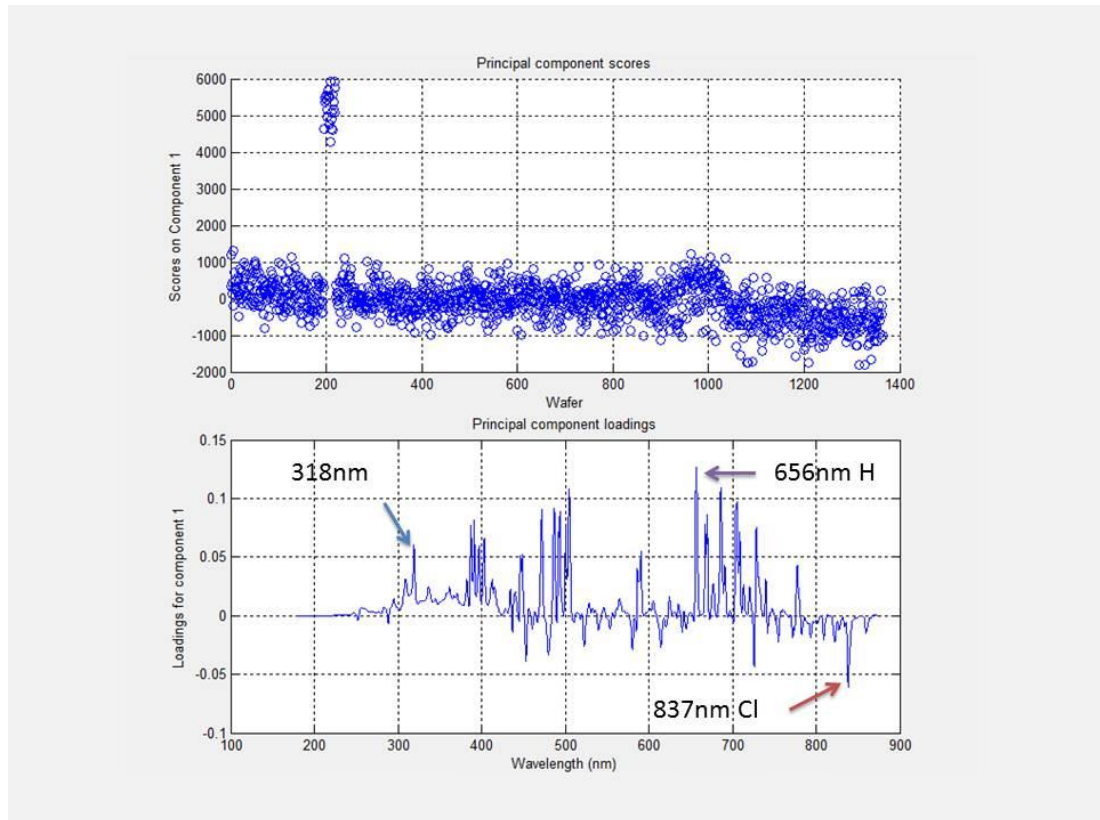


Figure 4-29: The results from the principal component analysis displaying the scores for each wafer in the loadings for each variable in the spectrum.

A number of key wavelengths were determined from Figure 4-29. Two wafers from the excursion were compared to two normal wafers. The results are displayed in Figure 4-30. The time series data for the spectral lines gives more information than summary statistics. The difference between excursion wafers and normal wafers can easily be seen. As discussed in section 4.1.1, residual chlorine and bromine from the chamber walls are an intrinsic part of the normal processing conditions. In Figure

4-30 considerably less chlorine and bromine is observed in the excursion wafers compared to the normal wafers. In addition, as discussed previously the of the reduced levels of bromine and chlorine has an effect on the EEDF and this is reflected in the emission lines of helium, hydrogen and oxygen. Given the important contribution of bromine and chlorine to the etching of silicon in step 1, the reduced levels for the excursion wafers suggest this to be the primary reason for the reduced etch rate during the excursion. It is also noted, while it is difficult to accurately determine the density of atomic oxygen in the process due to the changing EEDF, its impact is believed to be minimal. This is mainly due to the fact that, while chlorine and bromine would not etch SiO_2 , the fluorine from the SF_6 will etch both Si and SiO_2 and remove any SiO_2 on the surface of the wafer and additional oxygen emanating from the chamber walls. This data points to an issue with the in-situ cleaning process that is performed between each wafer. This is supported by the data in Figure 4-27 where the removal of the in-situ clean eliminates chlorine and bromine presence in the process.

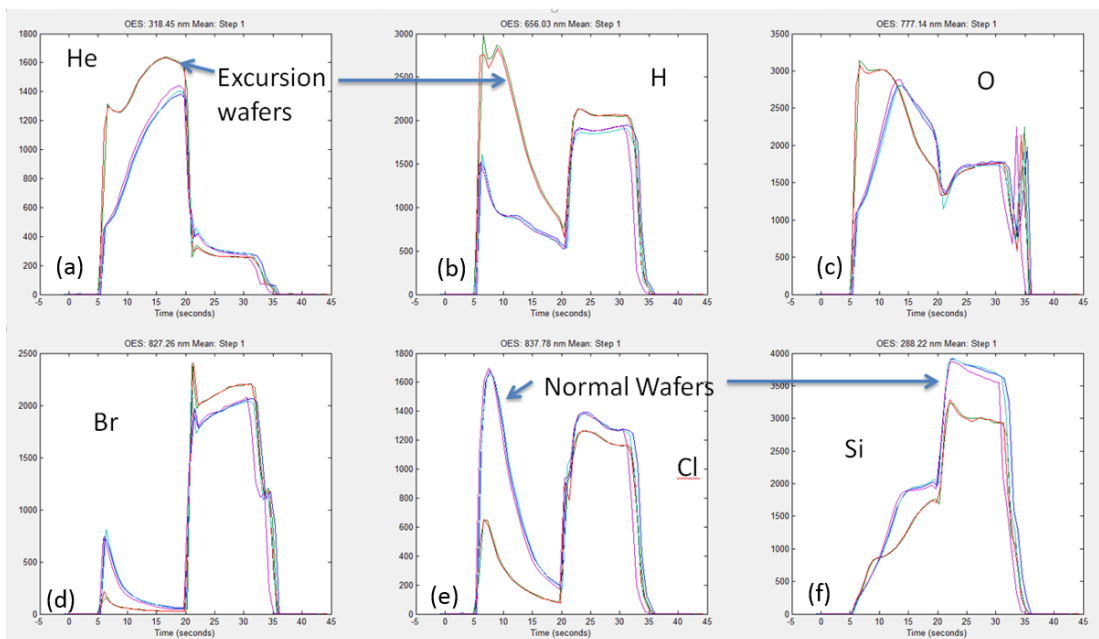


Figure 4-30: Graph shows the key wavelengths intensities that represent the main etch activity and the difference between the excursion wafers and the normal production wafers.

In order to further validate the cause of the lower levels of bromine and chlorine in the excursion wafers, the in-situ cleaning process was studied. As discussed previously, the in-situ clean is an Ar/Cl₂/HBr/O₂ chemistry, with a silicon wafer etching. An RF bias is also employed to increase the flux and energy of ions to the surface of the wafer increasing the bombardment of the silicon lattice and thereby enhancing the etching by chlorine and bromine neutrals. It has been widely reported that the etching of silicon in the presence of chlorine, bromine and oxygen results in the deposition of SiOCl_x and SiOBr_x on the chamber walls[17][51][52]. During the in-situ cleaning a thin layer is deposited on the chamber walls. During the subsequent etching of the production wafers, the deposited film is etched by the fluorine from the SF₆ feed gas [51]. This liberates chlorine and bromine and oxygen from the film which are then available to react with the surface of the wafer. From the analysis of the time series data from chlorine and bromine, it is evident that the densities decreased quickly in step 1 of the product wafer. This suggests that the film on the chamber wall is thin and therefore its contribution is limited to the start of the recipe step.

In order to test this hypothesis a number of experiments were conducted in which processing conditions for the in-situ cleaning were modified. The experimental set up involved changing a number of recipe parameters in the in-situ clean. The in-situ clean experiment was followed by a production recipe. OES analysis was then completed for each of the production recipes to determine the impact the in-situ

cleaning had on each production wafer. In Figure 4-31, chlorine wavelength (837 nm) of the production process is presented for four adjustments made to the in-situ clean and compared to the normal in-situ clean.

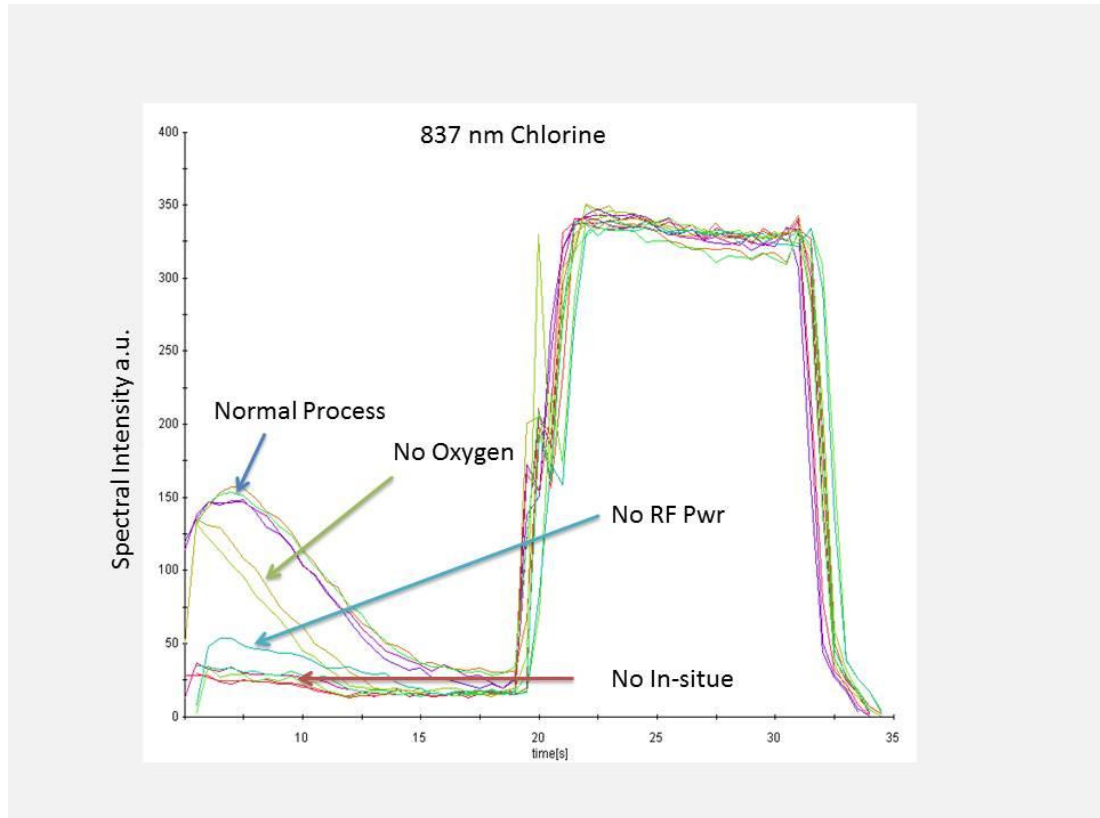


Figure 4-31: The intensity of chlorine outgassing from the chamber walls as a result of various pretreatment applied to the chamber before the wafer was processed.

The exclusion of oxygen from in-situ recipe significantly reduced the density of chlorine in the subsequent product wafer processed. Eliminating RF bias from the in-situ clean significantly reduces the etching of the silicon in the in-situ cleaning process. These two experiments are compared to the normal in-situ clean and to no in-situ clean. The density of chlorine in Figure 4-31 demonstrates that the presence of oxygen and silicon is needed in order to maximize the growth of SiO_xCl film.

Further investigation into the chemical composition of the deposits formed on the chamber walls was performed. A flake of deposition from the walls was extracted during a routine chamber clean. Time-of-Flight Secondary Ion Mass Spectrometry (TOF-SIMS) was used to analyse chemical profile of the flake. TOF-SIMS uses a pulsed primary ion beam to desorb and ionize species from a sample surface. The resulting secondary ions are accelerated into a mass spectrometer, where they are mass analysed by measuring their time-of-flight from the sample surface to the detector. Depth profiling by TOF-SIMS allows monitoring of all species of interest simultaneously, and with high mass resolution.

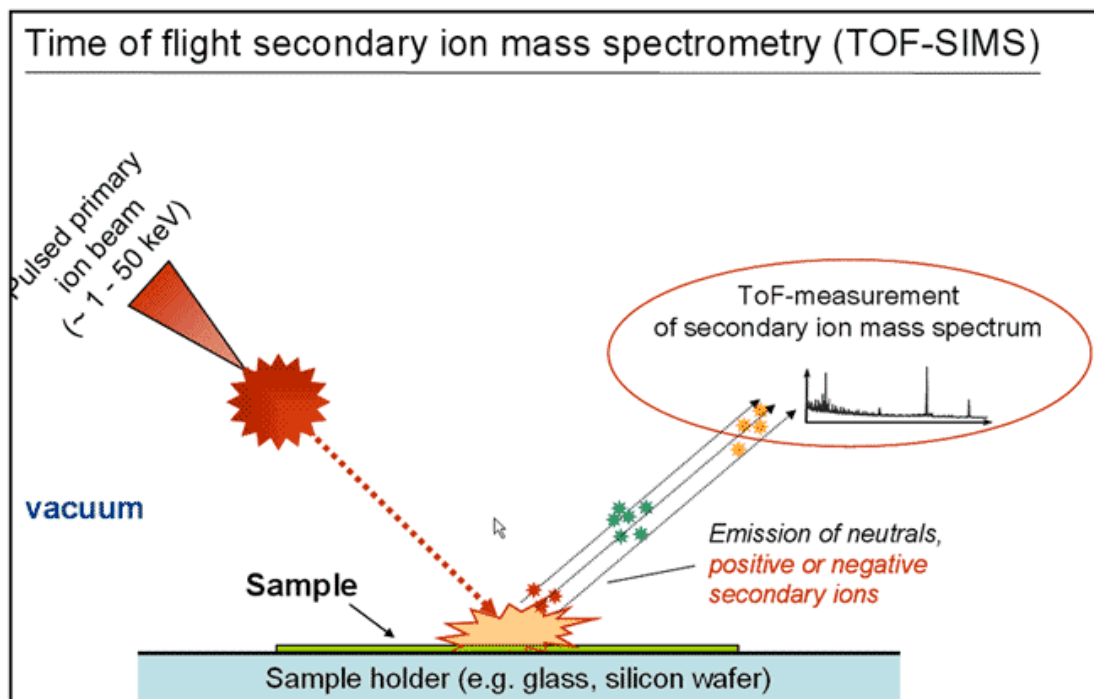


Figure 4-32: A schematic of the principle of operation of a time of flight secondary ion mass spectrometer.

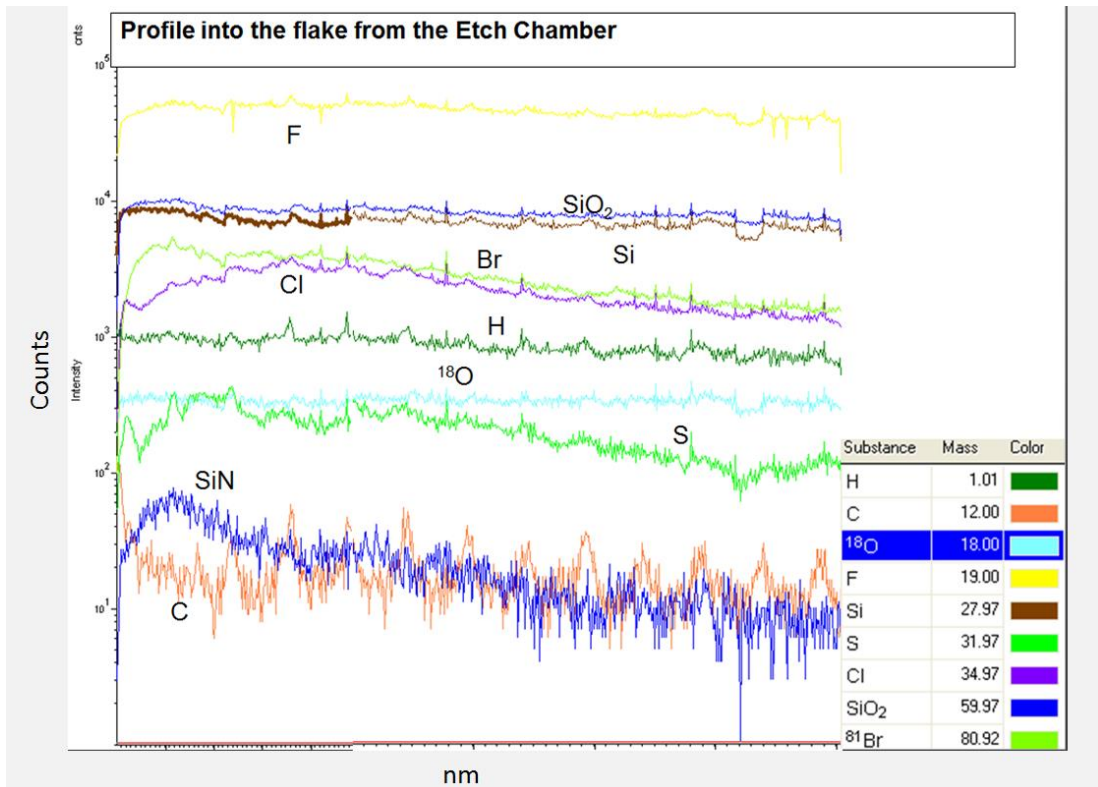


Figure 4-33: The results from the time of flight secondary ion mass spectrometer analysis of a sample taken from the chamber walls.

Results from the chemical profile of the flake taken from the chamber after it had processed over 10,000 wafers is displayed in Figure 4-33. The results agree with the experimental OES data confirming the presence of silicon, oxygen, bromine and chlorine deposited on the chamber walls.

In concluding the root cause of the excursion, it is evident that lower concentrations of chlorine and bromine in Step 1 of the processing of the production lot resulted in a lower etch rate. Subsequent investigation found that the in-situ clean wafers had oxidised significantly due to excessive use thus reducing the etching of the silicon (silicon oxide) by the Cl and Br species and also resulting in a reduction the SiO_xCl SiO_xBr film deposition on the chamber walls.

4.3.5 Discussion and Conclusion

The techniques described in this chapter were primarily focused on investigating the source of etch rate variation in an industrial plasma etcher. OES has been shown to be a very powerful diagnostic tool for process monitoring. PCA is a very useful exploratory tool for the analysis of large volumes of production data. It is especially useful when there is no metrology. For etch rate prediction GBT has been demonstrated as a robust technique with the additional benefit of ranking the importance of the variables used in the prediction. This information can be used to improve the understanding of the industrial plasma processes.

It was also shown that the intensity level of atomic or molecular species alone is not a true determination of its gas density. The dynamics of the chemistry can have a large impact on plasma parameters and electron dynamics resulting in changes to excitation rates resulting in different emission intensities. These changes to the excitation rates compound the chemistry's behavior and vice versa. It is therefore necessary to look at more than just changes in one species emission intensities in order to determine the behavior of the process chemistry. Looking at the emission intensities of inert gasses in the process gives clues as to the behavior of the electron dynamics. The chambers walls have a significant impact on the process repeatability for this processes.

Table 2: Atomic transitions associated with main spectral lines used for plasma monitoring

nm	Species	Lower eV	Upper eV	Transition
251.6	Si	0.02	4.95 eV	$3p^2 - 3p4s$
288.2	Si	0.7	5.08 eV	$3p^2 - 3p4s$
318.8	He	19.8	23.71 eV	2s-4p
656.3	H	10.2	12.09 eV	2-3
777.2	O	9.14	10.74 eV	3s-3p
777.4	O	9.14	10.74 eV	3s-3p
827.2	Br	No Info		
837.6	Cl	8.92	10.4	4s-4p

Chapter 5

Virtual Metrology in Production

5.1 Introduction

The implementation of virtual metrology in a semiconductor manufacturing can have significant benefits in terms of cost and quality[53]–[57]. As discussed in the previous chapter 4, the value virtual metrology can offer goes from simple and accurate (supervised) fault detection and process diagnostics to enabling metrology reduction and ultimately process control. The offline analysis of data by an engineer can have significant benefits in terms of understanding variability within the process and offering solutions to improving process recipes as well as detecting and diagnosing process excursions and equipment failures. Implementing this kind of analysis to occur in real-time with no human intervention and produce reliable and

accurate results presents new challenges. In this chapter the architecture developed to deliver real-time metrology estimation using OES data to predict etch rate. Details of the workflow for the data analysis is also presented as well as some of the safeguards developed to prevent inaccurate metrology estimation. Results are presented for the sequential prediction of the etch rate for two lots before the automated retraining of the model is performed when real metrology is available for the two lots. A variable contribution pareto algorithm is also discussed in which the variables responsible for the variation in the metrology for each wafer can be calculated. Discussion on using multiple models and switching between them dynamically is discussed.

There is considerable complexity when implementing a fully automated virtual metrology solution in a high-volume manufacturing fab. There are significant benefits of supervised learning over the traditional un-supervised approach that is widely implemented for fault detection in semiconductor manufacturing. One of the challenges of the un-supervised approach for fault detection and classification has been in determining statistical windows of operation for the parameters. The traditional approach has been to calculate statistical limits over a large timeframe and potentially across many tools. The limits are then typically set determined at a time when equipment was performing within specification. Any deviation from these predefined limits is considered a fault. This kind of approach generates a lot of false positives and in some instances false negatives. In some cases, where there have been numerous alarms an engineer may review the metrology for a period of time and determine a new good state and recalculate limits. This manual intervention is time-

consuming. A supervised approach to modeling the data is much more effective and accurate and affords the possibility of a fully automated solution.

5.2 Architecture

Implementing a virtual metrology platform in a manufacturing environment requires a very robust data flow management system. The system must deliver data from a number of sensors deployed on processing equipment in the factory. The sensor data must be merged with additional data sourced from the manufacturing database, such as metrology, to perform analytics in real-time. In addition, the large number of data points in an OES spectrum results in file sizes of over 3 Megabytes per wafer, which presents computing challenges. Further more the system needs to be scalable to allow factory wide deployment.

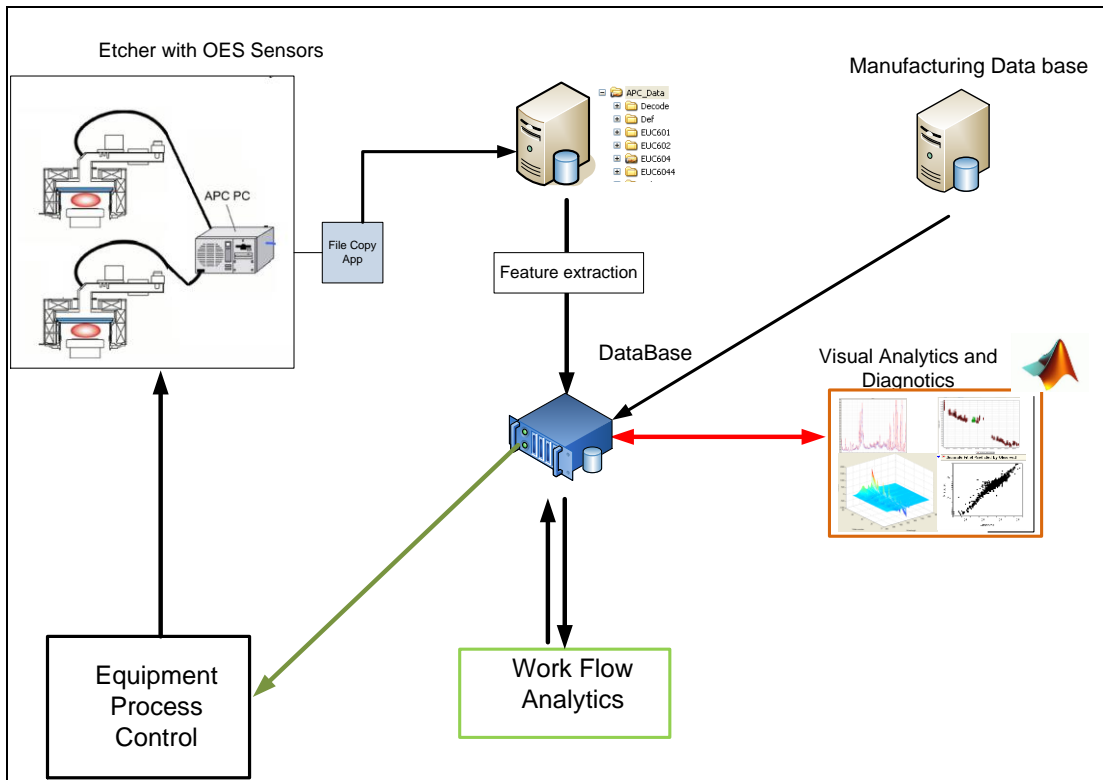


Figure 5-1. Real-time virtual metrology service orientated architecture. The schema enables real-time data collection and analysis and decision-making.

A schematic of the system architecture is presented in Figure 5-1. The OES sensor is a commercially available Ocean optics USB 2000 spectrometer. Acquisition of the data is triggered when light from the discharge exceeds a predetermined threshold. The equipment parameters are collected continuously for the duration for which the wafer is in the chamber. This data is saved on the local PC. A file copy service was developed to watch for new wafers and copy the files from the local PC to a server. A second service detects data files arriving on the server and merges and synchronizes the OES and equipment parameter data into one time series file representing the data for one wafer. A third service then passes the data to a feature extractor where summary statistics are calculated. Both the summary and time series

data are then loaded into the database. The loading of the sensor data for the wafers then triggers structured query language (SQL) to query the manufacturing database for contextual information including lot, product and recipe information for those wafers. Once the sensor data and context data have been merged in the database a SQL trigger exports the summary data for that wafer to the workflow environment. The workflow is described in the next section.

Using the same link server to the manufacturing database the SQL code continuously monitors tables within the manufacturing database for new metrology that is associated with lots that ran through the particular etcher. When new metrology becomes available for the lots that ran through the etcher, SQL copies the metrology to its own database and also sends a copy to the workflow to enable models to be retrained and validation to be performed. The local copy of the metrology is also to allow it to be merged with the sensor data for off-line analysis by the engineers for process diagnostics and model development. Merging all the data associated with a wafer in one database is imperative for effective diagnostics.

Once analysis has been performed within the workflow, results can be published back to the SQL database for review and/or sent to the equipment process controller where it can be used to shut the equipment down in the event of an excursion or the prediction of metrology can be used in the run to run controller.

Using a service orientated architecture allows the services to be distributed across multiple servers offering the opportunity to expand the capability to large-scale deployment by distributing the computing.

5.3 Workflow design

The objective of the workflow design is to provide a fully automated self-learning system capable of detecting outliers, estimating metrology and providing a list of important variables that drive the variation in metrology for each individual wafer. The advantages of using the gradient boosting trees (GBT) model in this case is that parameters such as recipe and product can be included in the models, reducing the number of models that are necessary to maintain. In a high-volume manufacturing facility there can be hundreds of products running through many chambers which would result in thousands of models. Managing such an environment would be unsustainable. The system was also designed to be able to automatically learn new relationships for new products or recipes and automatically defining the appropriate limits. This is achieved by continuously refreshing the models when new downstream metrology becomes available validating whether wafers are good or bad.

5.3.1 Outlier detection and metrology estimation

Once the sensor data for an individual wafer becomes available in the SQL database and the associated context data has been merged, a trigger is fired within SQL. A pre-set query extracts the summary data for all the peaks for steps 1 and 2 of the process and sends the data to the flow controller. Here the data is transformed into a matrix format. Using a system of folders and folder watcher services, the outlier detection service detects an incoming wafer and passes the data through a T^2 multivariate algorithm. Hotelling's T^2 is a measure of the variation in principal component space. The T^2 value is then compared with a warning and abort

thresholds. When the analysis is complete, the results are posted to an output folder which the flow controller is monitoring. This data is then sent back to the SQL database where it is stored. If an abort has been detected, the abort is published immediately to the SPC system to shut the tool down. If a warning has been calculated this information is also sent SPC. Here, rules can be put in place so that if more than one or two warnings are detected it will instruct the tool to shut down.

The GBT model that was built in Chapter 4 also monitors the output from the flow controller and copies the sensor data for analysis. It also monitors the results of the outlier detection. If the T^2 analysis reports an abort, no GBT calculation is performed. The reason for this is the validity of the estimation from the GBT algorithm is questionable when the data for the aborted wafer differs significantly from the distribution of the training data. In the case where a warning is detected, the GBT analysis is performed to produce an estimation of the metrology.

In all cases, the variability importance algorithm is executed. This technique, while using data the training data, gives information as to the weights of the variables within the boosting tree that made this wafer different. This information is extremely useful in providing diagnostic of the potential cause of the warning or an abort. Even on wafers that pass the SPC etch rate limits, information regarding the parameters that influence the variation in metrology give vital clues as to the characteristic of the process. This type of information can help engineers understand normal behaviour and process drift post maintenance and how the parameters that drive the variation may change across the preventative maintenance (PM) cycle. It also may be useful in understanding chamber to chamber variation.

5.3.2 Model updating

When new metrology becomes available, this data is used to refresh the modelling parameters in the workflow. If the metrology has met specifications and has passed the SPC limits, then this validation is used to update the outlier detection limits and to retrain the GBT model. To do this, the history of the metrology and sensor data is required to retrain the models. This historical dataset can be of the order of gigabytes. While the data is stored in the database, retrieving this volume of data each time new metrology is available to retrain the models puts significant loading on the I/O of the database server. As an alternative, the data is stored locally within the workflow with the new sensor and metrology data being appended to the file. In addition, a purging routine is performed on this data source to keep it within the configurable time window. If the metrology for a lot has breached the SPC limits then this information is used by the model manager to adjust the outlier detection thresholds automatically.

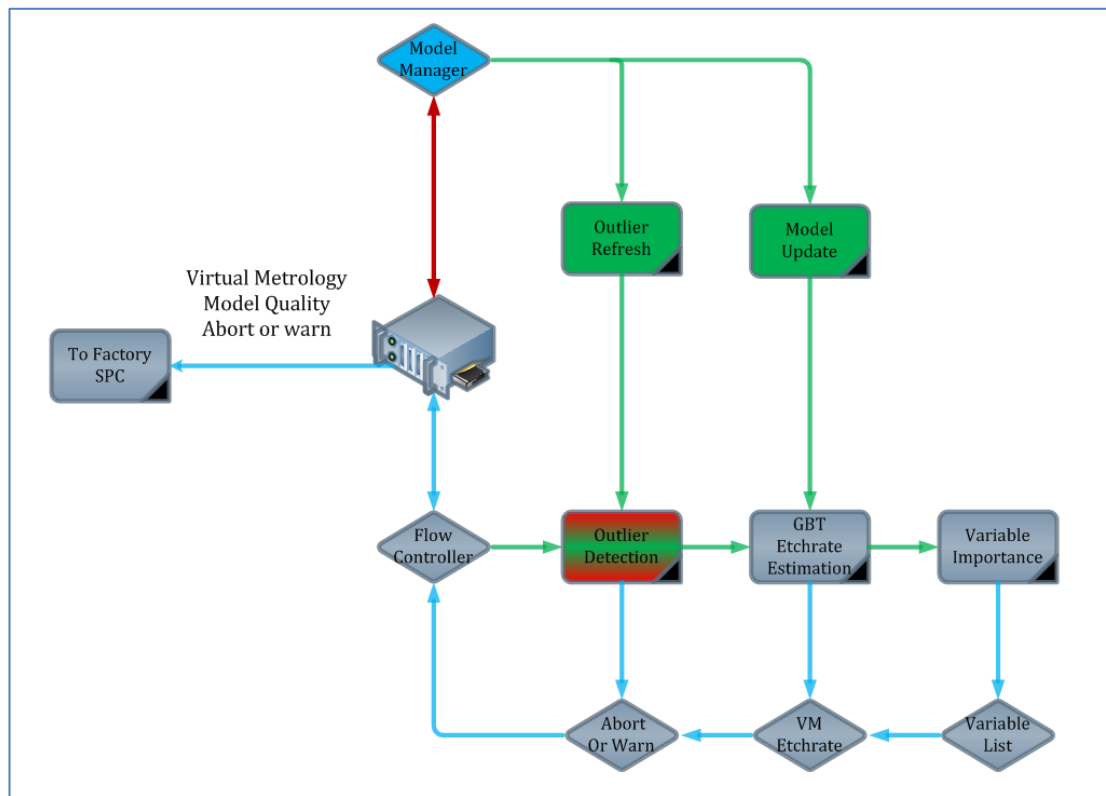


Figure 5-2: Diagram of the workflow used to detect outliers and predict metrology.

5.4 Results

Before evaluation could begin, a 200 wafer historical data set was used to build models for the Max T^2 , the GBT and the variable importance algorithm. The model configuration was set in the workflow and the system began calculating etch rate predictions for each wafer when it was finished processing on the tool. There was a four hour delay between the processing of wafers on the etcher and the measurement of metrology downstream. This resulted in a two or three lot delay between the predictions of etch rate and the model retrain.

A rolling window of 150 wafers was used to train the Max T^2 algorithm. This would give the algorithm a quick response to sudden shifts in the parameter distribution and also the ability to adjust quickly to chamber drifting or to relearn new environments. The results from the Max T^2 analysis are displayed in Figure 5-3. The graph shows the etch rate shifts for the excursion, elevated etch rate, and return to normal behaviour. The Max T^2 statistic detects these shifts but also re-teaches quickly. This is important so the algorithm can detect the excursion and afterwards manual intervention is not needed to retrain the tool before the chamber is brought up to production again.

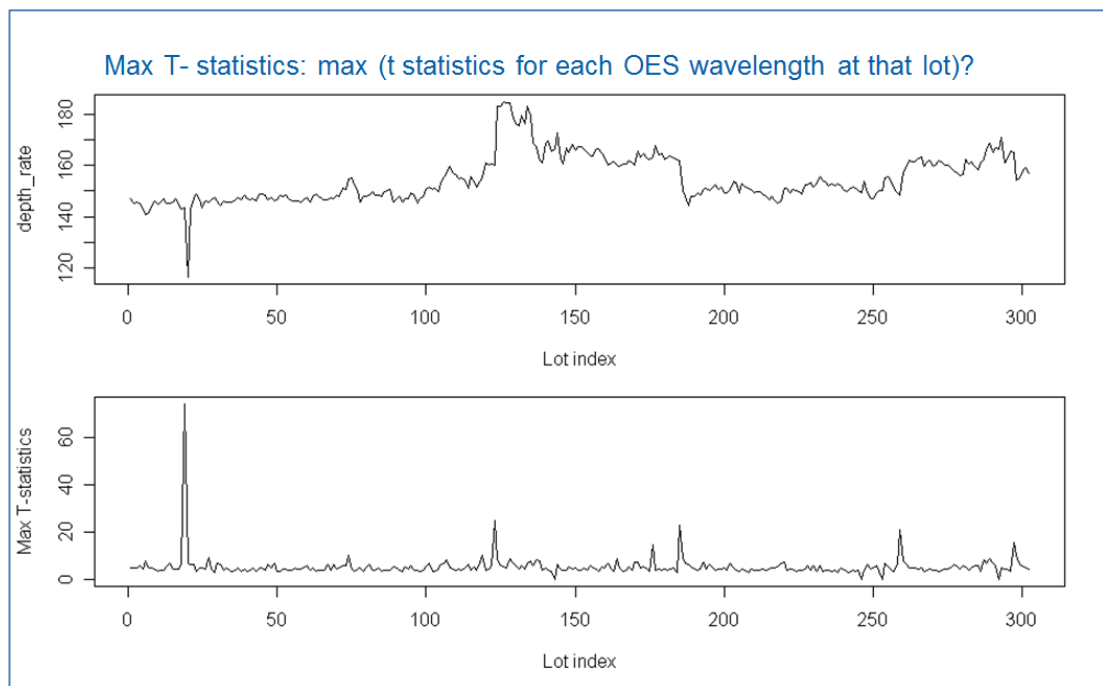


Figure 5-3 A Multivariate T^2 approach can easily pick up the etch depth deviations from the OES data.

The results of the GBT model prediction of etch rate are presented in Figure 5-4. The graph shows the actual etch rate, the predicted etch rate and the error in the

prediction. The model does not make a prediction for the excursion due to the fact that the Max T^2 outlier detection triggered an abort determining that the excursion was outside the range of reliable prediction for the GBT model. The rolling window for the GBT was set to maximum to include all historical data for this pilot test. The maximum error in the models prediction was at the shift up in etch rate. The GBT model is slow to retrain and a number of wafers are predicted with a higher error as the model slowly accounts for this new distribution of data. This is one disadvantage of the GBT modelling approach. The model performs well when the data returns to normal behaviour.

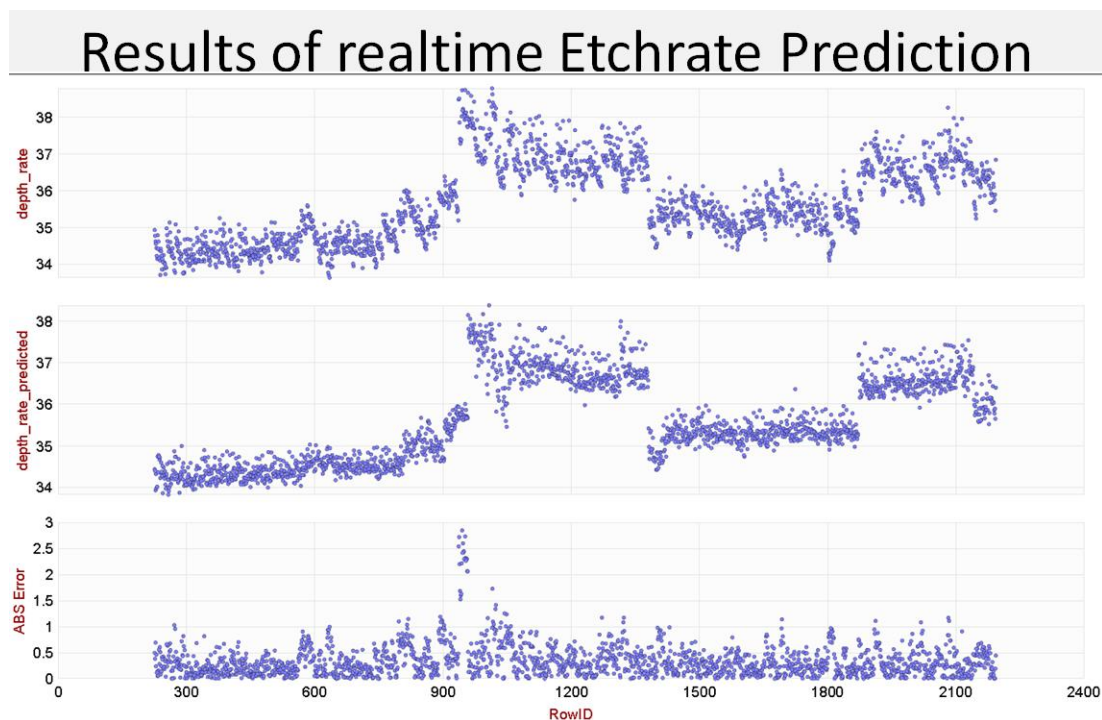


Figure 5-4: The graph shows the actual etch rate, the predicted etch rate and the error in the prediction.

The results from the variable importance algorithm are presented in Figure 5-5 and Figure 5-6. A tree ensemble model is built to predict etch rate from a given good baseline. This was carried out at the start of the modelling evaluation process. The model was only rebuilt automatically when the etch rate was within very tight target. The algorithm calculates a score for each wafer as a measurement of how far the wafer is from a known good baseline. The advantage of this “metrology aware” technique over others is that it takes advantage of a learned behaviour between sensor measurements and the metrology to determine which parameters are most likely to have caused the deviation from baseline. The score per wafer is presented in Figure 5-5. The graph presents the etch rate results and the score is represented by colours. The excursion has the highest score followed by the etch rate shift up at wafer 900.

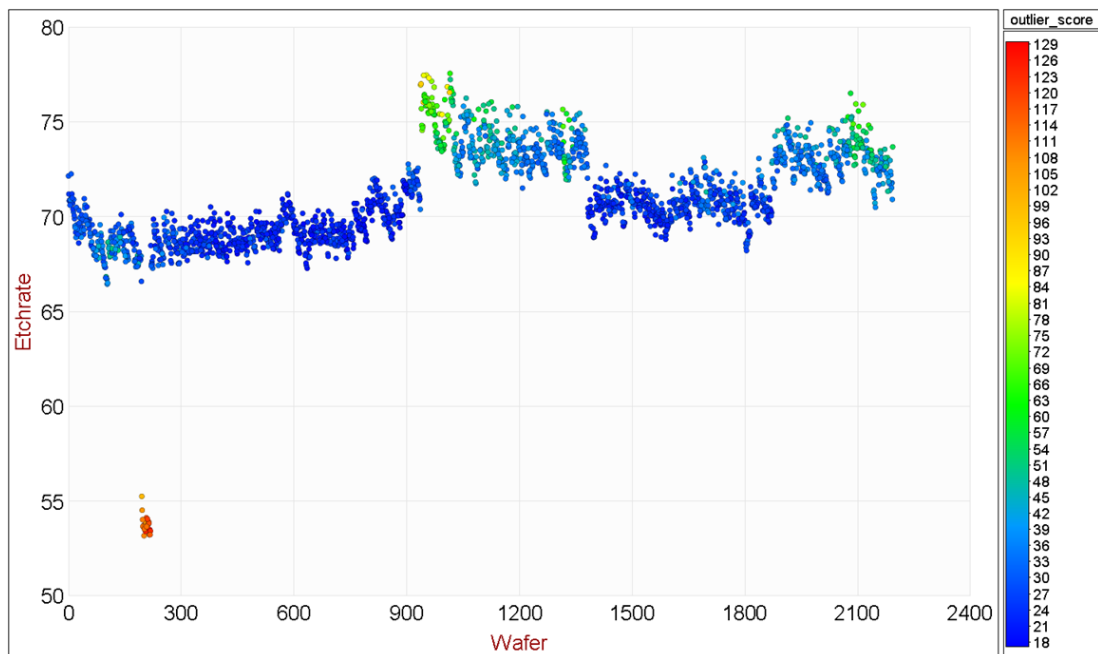


Figure 5-5: The graph presents the etch rate results in colour by the score. The excursion has the highest score followed by the etch rate shift up at wafer 900.

In examining the wafers with the highest score, a pareto chart of the parameter that contributes most significantly to this score is given in Figure 5-6. The pareto for an excursion wafer is examined and the top parameters are 310nm and 320nm. The time series data for these two parameters is displayed in Figure 5-7. The OH and helium time series line clearly differs from the excursion relative to the normal wafers. In Chapter 4 the diagnosis for the excursion was determined to be abnormal wall conditions resulting from low consumption of silicon in the in-situ clean. This statistical techniques also determines the abnormal behaviour of helium as a differentiator between the good and bad wafers. As shown Chapter 4.3.4, helium's behaviour is driven by lower chlorine and bromine density in the excursion wafer's process.

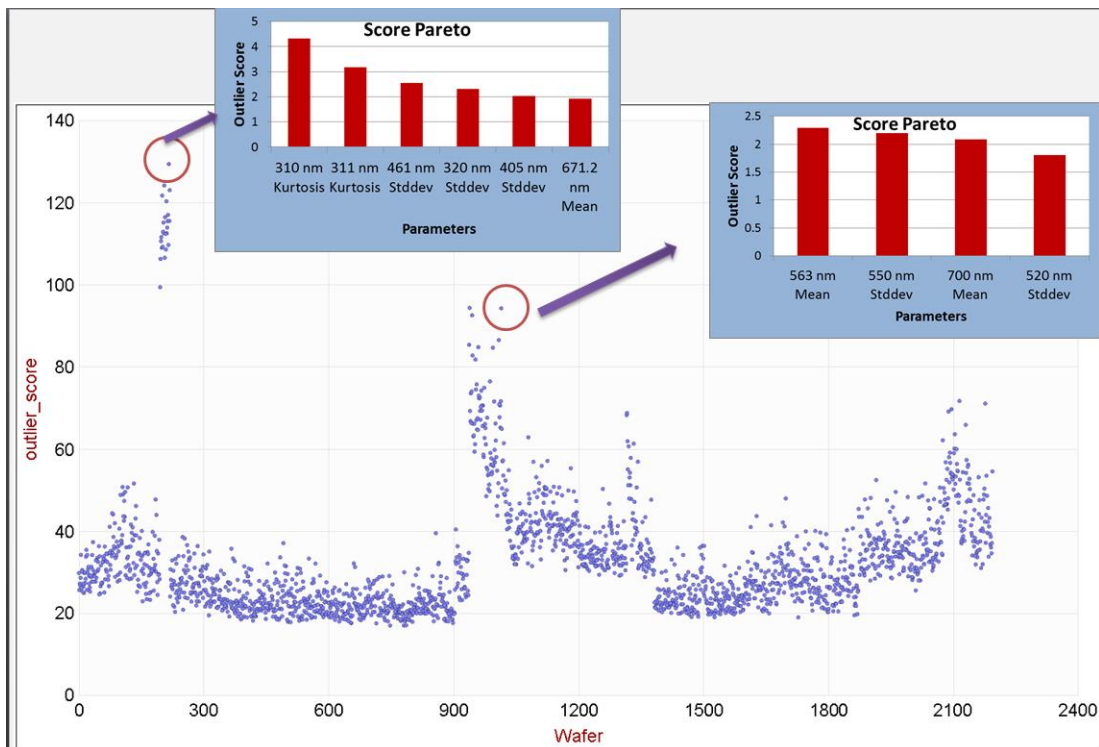


Figure 5-6: The pareto chart for a wafer in the excursion lot shows the wavelengths that have contributed the highest score.

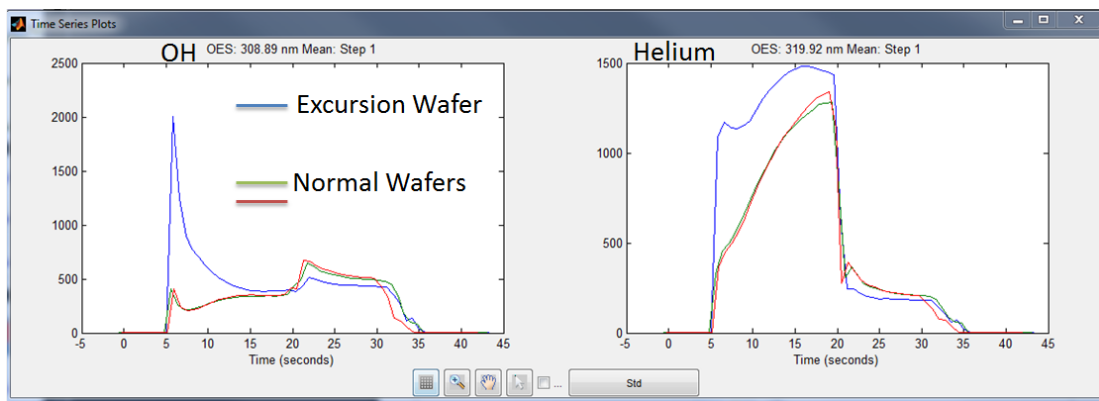


Figure 5-7: Time series of the spectral lines identified as the highest outlier score for the excursion wafer.

5.5 Discussion and conclusion

In the case study in this chapter, the fully automated architecture and workflow performed very well in predicting etch rate and providing diagnostic information as

to the cause of the excursions and shifts. The simple outlier detection algorithm detected the excursion and also provided some warning when there was a shift in the etch rate but it was still within specifications. The GBT model performed well with the exception of the first few wafers after the etch rate jump at wafer 900. Here the model was slow to retrain and alternative approaches could be taken. A number of different approaches have been explored [58]. Global and local model approaches have been applied on same dataset as this case study. The best approach for dealing with the sudden shifts in etch rate were use a short window local model (SWLM). The best results were achieved in predicting the first few wafers, after a significant etch rate shift, was to use feature selection and a linear model. Only one wafer after the etch rate shift was needed in the training dataset to provide accurate prediction of the subsequent wafers. This approach will be especially useful post maintenance when chamber conditions are significantly different from a seasoned chamber. The SWLM approach could be taught on a test wafer post maintenance providing accurate fault detection when the performance of the chamber is unpredictable and there is a high risk to production.

Further development of the workflow could employ multiple modeling techniques in parallel which could be supervised by a further algorithm which learns the performance of each modeling approach by comparing its prediction versus the actual metrology in combination with PM counter for example. The model could then switch from the global model using GBT to a linear model depending where in the PM cycle the chamber is.

The process diagnostic information, the modeling provides, is extremely useful. Characterizing the behavior of the metrology variation across the PM cycle and understanding what drives that variation is very important. This information can very useful for chamber matching and process characterization. Knowing the source of the variation can assist greatly in engineering solutions to mitigate this variation in processing conditions that drives the metrology. The important variables from the GBT model reveal that the mechanism driving the metrology variation changes over the course of the PM cycle. After maintenance with clean walls the sticking coefficient is different from that of a seasoned chamber. This will affect the absorption or de-absorption of species in the walls and also affects the recombination rates on the wall surface. These effects are captured in the behavior of the OES spectra.

When an excursion, or a significant deviation, in etch rate occurs, this is when these analytical tools become most useful. In these cases a decision on what actions to take needs to be made manually or automatically. In the case of the excursion, the workflow was able to identify the large deviation from normal operation mode. The variable importance algorithm identified wavelengths that contributed to the excursion. These particular wavelengths were validated in chapter 4 through experimentation and other statistical techniques. Having this analysis automated significantly reduces the work required by an engineer to come to a conclusion and greatly improves the reliability of the diagnosis.

Chapter 6

Electrical characterization of a capacitively coupled plasma etcher.

6.1 Introduction

In the previous chapters, the variation in etch rate was investigated through the analysis of OES data. It was concluded that the most significant source of variability in the process came from wall disturbances. In previous work of others particular case, the deposition of SiO_xCl_x [59],[60],[61] on the walls during an in-situ clean resulted in the recycling of chlorine/bromine and oxygen back into the chamber during normal wafer processing. The uncontrolled recycling and/or deposition during wafer processing creates significant wafer to wafer and lot to lot variation in etch performance. The analysis in the chapter 3 only pertained to the data within one maintenance cycle. In addition to impacting on the reproducibility of the plasma process, chamber wall deposition also generates solid particles. These particles are as a result of thin-film on the chamber walls flaking off due to stress within the film as well as thermal stresses induced by turning on and off the RF power. Routine chamber cleaning maintenance is necessary to keep flaking particles from landing on the surface of the wafer resulting in defects and impacting yield. During these

maintenance cleaning routines, chamber kits, including quartz, stainless steel and ceramics are removed from the chamber and cleaned. In many instances replacement process chamber kits are installed to minimize the downtime. During the course of removing chamber hardware, the disassembly of the chamber is necessary. In addition, some hardware, such as electrodes are eroded by the process and have to be replaced. The removal and reinstallation and/or replacement of this chamber hardware can significantly impact the process performance of the chamber. This intrusive maintenance is known to have an impact on the process performance of the chamber. In Figure 6-1 the etch rate performance of two chambers for 4000 wafers is displayed. A significant jump in etch rate is observed after maintenance cycle 2 on etch chamber 1 (EC1_2). Some process performance change is expected when the chamber walls are cleaned and the chamber is unseasoned. However, it would be expected that this effect would be reduced as more wafers are processed and the chamber walls return to a previous steady-state. After some particular maintenance activities, the performance of the chamber shifts dramatically which cannot be explained by the wall effect.

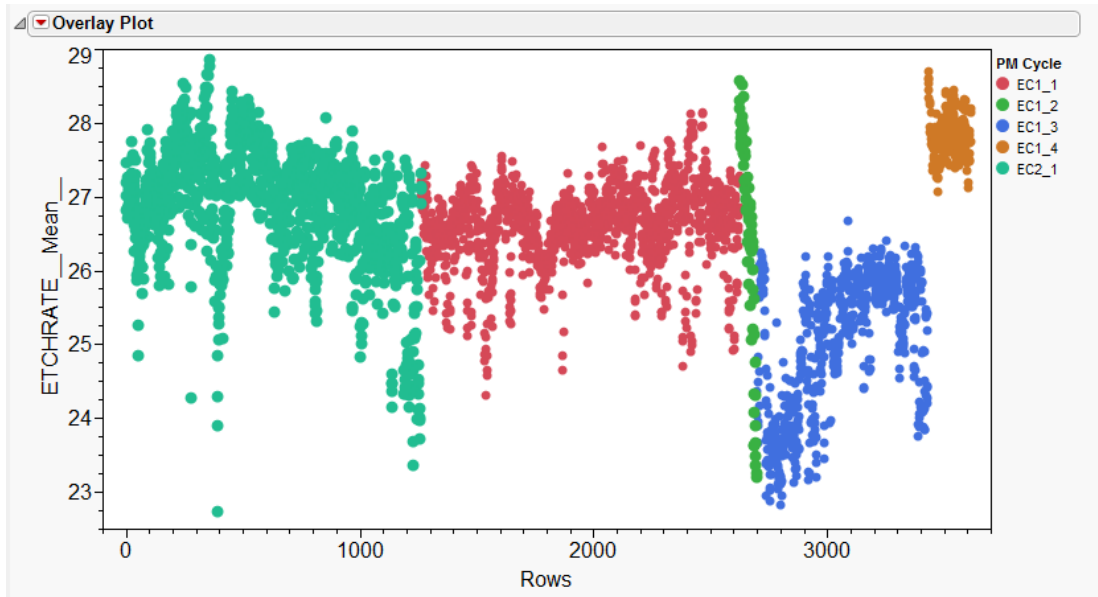


Figure 6-1: Etch rate performance of two ECR chambers EC1 and EC2. Significant etch rate shifts can be observed after preventive maintenance cycle (2) as observed in EC1_2

The data from the microwave tuner gives an electrical measurement of both the plasma and the chamber hardware. This electrical measurement can be used to characterize how the chamber/plasma impedance is presented to the 2.45 GHz electromagnetic wave from the magnetron. The autotuner measures the reflections from the plasma and responds dynamically to the changing impedance of the plasma as a wafer is processed. As discussed in section 4.3.4, the varying wall state does impact the plasma parameters which will drive a response in the electrical behaviour of the plasma process. This is seen in the behaviour of the autotuner data within one PM cycle in Figure 6-2. However, what is of most interest in this chapter is the electrical response of the plasma and chamber interactions induced by changing mechanical parts at maintenance activity. Significant shifts are observed in the

electrical characteristics of the process after certain maintenance activities. These electrical shifts have an impact on the process performance as seen in Figure 6-3 which shows the correlations between etch rate and tuning stub 1 position. The electrical characteristics of the process chamber from a radiofrequency perspective is a poorly understood phenomena in the semiconductor processing and the impact of the electrical characteristics on the process chambers has on the plasma parameters is poorly understood. In high-volume manufacturing, maintaining process reproducibility across multiple chambers is time-consuming and expensive business. Most chamber matching activities are performed empirically with few decisions driven by sensor data.

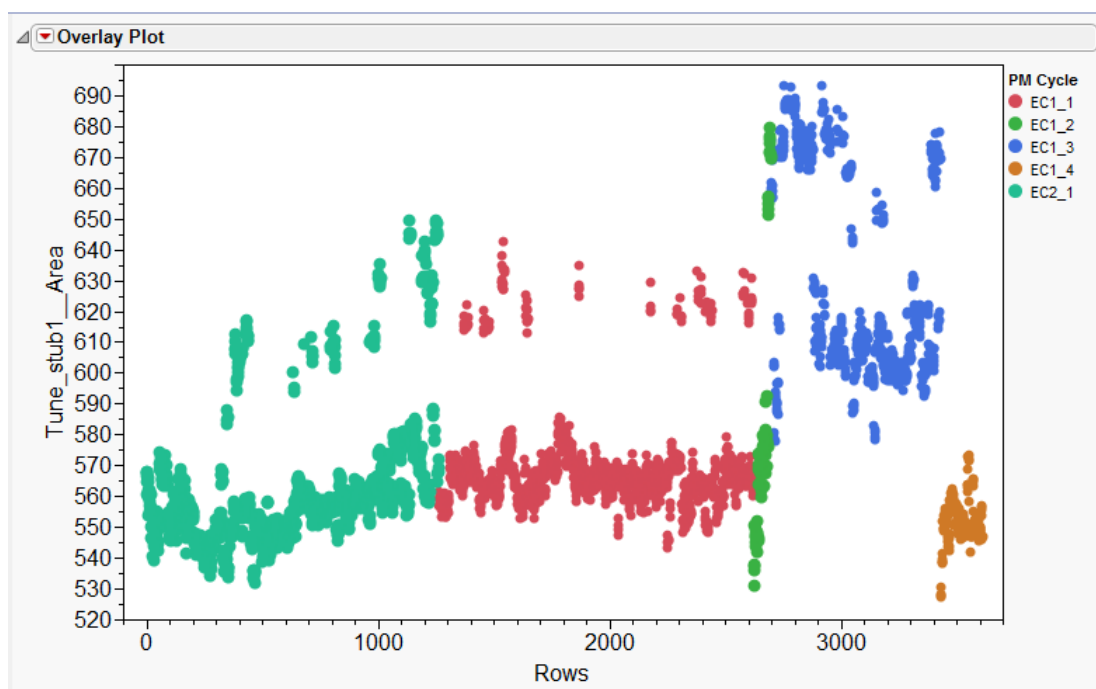


Figure 6-2: The position of the microwave tuning stub1 for 4000 wafers spanning multiple maintenance cycles is displayed.

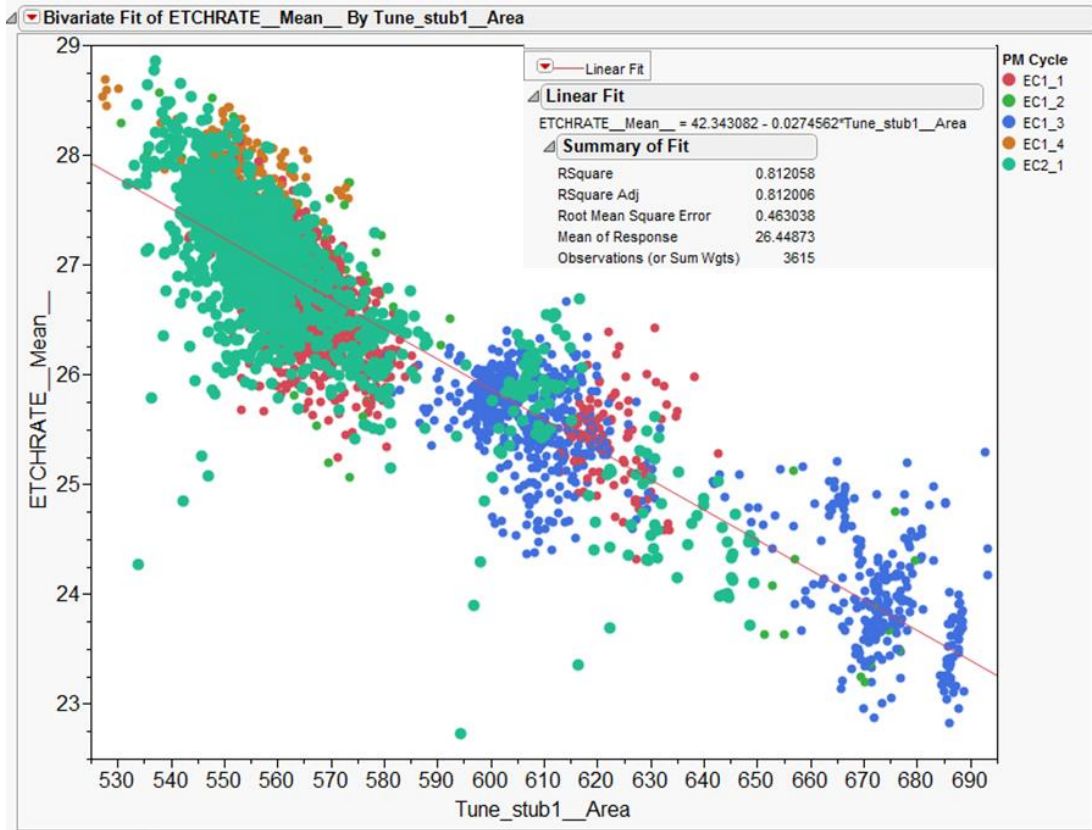


Figure 6-3: This figure shows the correlation between etch rate in the tuning stub position over multiple PM cycles for etch chamber 1&2 (EC1, EC2)

The objectives of this chapter is to study the relationship between the process chambers electrical parameters and the plasma parameters and their impact on the etching process. In order to change the electrical impedance of the process chamber in a controlled manner a variable inductor is inserted on the RF return ground path. This experimental setup allowed the electrical parameters of chamber to be changed

in a repeatable manner and plasma and etch rate measurements taken. It is shown that the etch performance of the chamber can be significantly modified by changing the ground path impedance. The electrical parameters are measured using current-voltage probes and electron density measurement is taken with a hairpin probe. Etch rate experiments are completed on two types of wafer. The first are poly silicon wafers which will etch spontaneously in a fluorine plasma without ion bombardment. The second are silicon nitride wafers which need ion bombardment of the surface to break the silicon nitride bonds allowing free fluorine to etch the silicon. The silicon nitride wafers were used in the experiment to study the impact that the electrical parameters had on ion bombardment of the wafer.

6.2 Experimental setup

A capacitively coupled 13.56 MHz RF parallel plate chamber was used to conduct the experiments. Current-voltage probes (VI) from Scientific Systems were installed on the powered and grounded electrodes. A hairpin probe was installed to measure electron density. A variable grounding unit was designed and built that could simulate the comparable of electrical impedance changes induced by maintenance activities in manufacturing. The grounding unit consisted of a variable inductor driven by a stepper motor that could be controlled while the chamber was running RF power. Real-time feedback on the position of the variable inductor was provided by an encoder. This enabled the chamber impedance to be altered in a repeatable fashion while still facilitating sensor measurements during the operation of the chamber.

6.3 The chamber

The RF power is delivered to the top electrode through a matching unit. The top aluminium electrode assembly includes baffle plates through which gas is delivered to the back of the electrode which has over 1000 holes delivering uniform flux of gas into the chamber. This assembly is mounted on a ceramic insulator ring which in turn sits in a cylindrical barrel assembly which can be driven up-and-down by a gap motor drive. The aluminium lower electrode assembly is mounted on ceramic insulator ring and is water cooled.

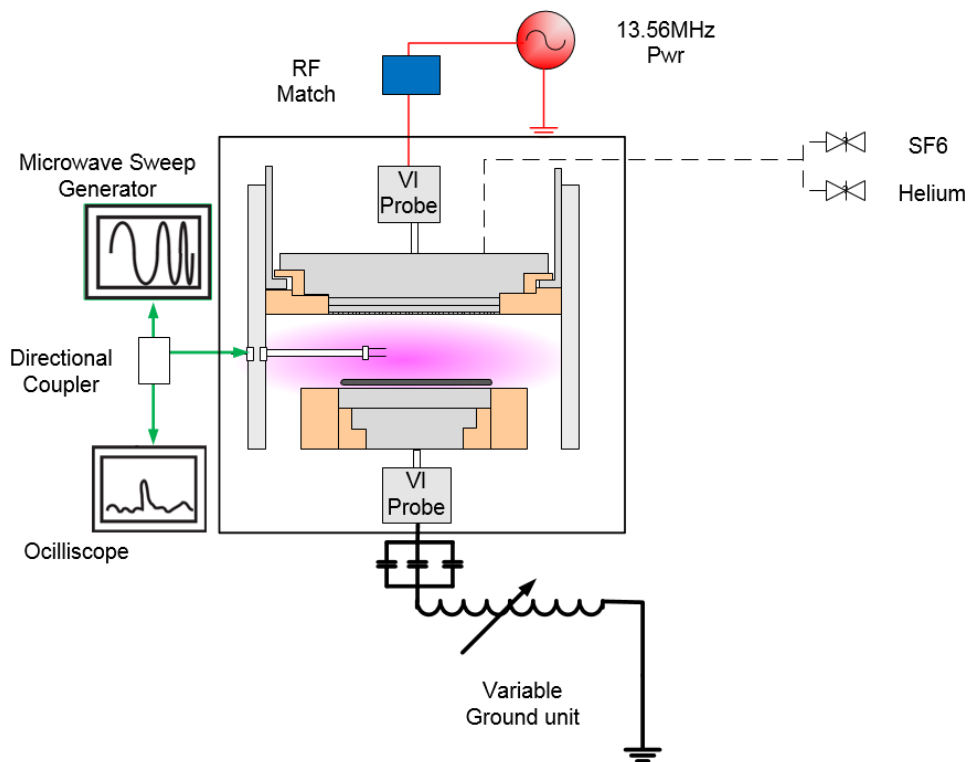


Figure 6-4: Schematic diagram of experimental apparatus.

6.4 Sensor measurements

Two VI probe sensors are used to measure the power delivered to the plasma from the generator and the output of the ground connection to the lower electrode. The first VI sensor was installed in the upper electrode assembly at the pins where the power is delivered to the upper electrode. This VI probe is orientated towards the chamber and measuring the plasma and chamber impedance downstream of the upper electrode. The second VI probe is mounted at the ground connection to the lower electrode such that it is outwardly looking measuring the impedance from the lower electrode to ground. The VI sensors measure root mean square current I_{rms} , potential V_{rms} and phase angle between them, ϕ . The VI probe sensor data collection was managed by a commercially available acquisition system from Lam Research. A hairpin probe collects electron density measurements using an intrusive probe that can make spatial measurements from the centre to the edge of the chamber. DC bias readings were taken from the upper and lower electrodes and measured with a Fluke 113 Digital Multi-meter.

6.5 Variable ground unit

The variable grounding unit consisted of three parallel 25 pF capacitors in series with a variable inductor. The hollow tubed inductor has an internal vane driven by a stepper motor which can be driven to any position using a control box. An encoder records the position of the inductor vane. In figure 6-5, the characteristics of the variable load are displayed. These bench test measurements were taken using a

TE1000 RF Vector Impedance Analyser at 13.56 MHz, while the position of the vane was cycled from 0° to 90° manually over a 60 second run. Initially, with the vane position at 0°, the total impedance of the grounding unit Z_g is 0.5 Ω of which 0.01 Ω is resistive. At 0° the capacitance is dominant, resonating out the effect of the inductor. This is reflected by -80° phase angle at the beginning of the graph. As the vane is rotated from 0° through to 90° the impedance rapidly changes from capacitive to inductive at about 10 s. From there the impedance rises linearly to a maximum of about 80 Ω . The resistive value increases to 1.5 Ω . However, later in the chapter data is presented showing that resistive value is seen to increase up to 5 Ω in some instances. This higher resistive impedance is due to the higher current experienced when in operation on the etcher as opposed to the low current employed by the network analyser. These type of resistive losses are commonly experienced in radiofrequency matches used in semiconductor manufacturing tools and have been documented.

From the results of the impedance analysis of the variable ground unit, the impedance of the inductor can be determined. When the vane is at 0° the total impedance, Z , of the match is ≈ 0 . The three 25pF capacitors are cancelling the effect of the inductor (L). Using equation:

$$Z = R + (2\pi fL - \frac{1}{2\pi fC}) \approx 0 \quad 6.1$$

Where f is the frequency of 13.56 MHz, C is the capacitance and R is the real resistance, the inductance of the coil at position 0 can be calculated to be $1.8 \mu L$ (153Ω) with an additional $0.9 \mu L$ when the vane is rotated to 90° .

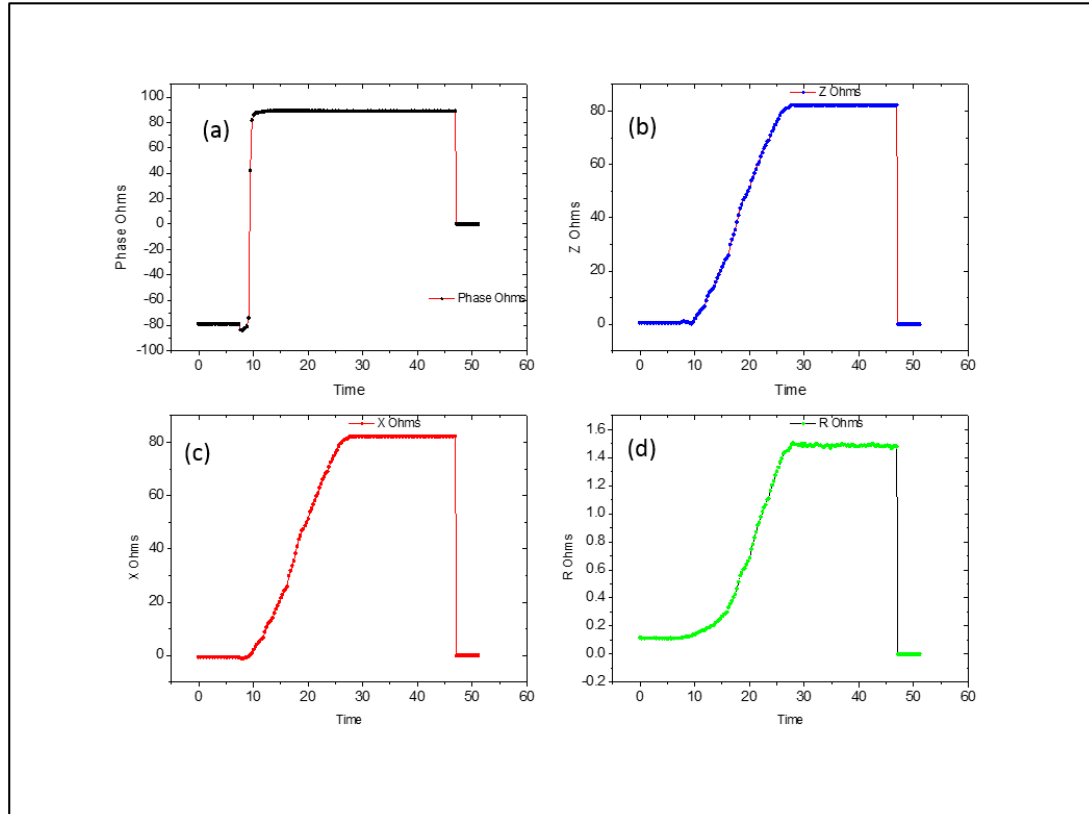


Figure 6-5: The electrical characteristics of the variable ground unit are displayed as the variable vane is moved from zero position to 90° .

6.6 The process

A 100 sccm of SF_6 and 100 sccm of He gas flow is used at 300 mTorr and 300 W for 45 s. The partial pressure of SF_6 at that flow rate is 80 mTorr. The electrode gap spacing is maintained at 5.0 cm. Electrode cooling water is maintained at $20^\circ C$ throughout all experiments. The process is used to etch 200 mm wafers. Wafers are

cycled in with a robotic arm through a load lock which prevents contamination from the atmosphere when wafers are loaded. The wafer is not clamped to the lower ground electrode and no backside helium cooling is provided. Wafers are also unloaded with a robotic arm through an exit load lock. The process is controlled with a microcomputer which ensures gas flows and pressure setpoints have been achieved before power is turned on. Polysilicon and silicon nitride substrates are etched using the same recipe. Before the wafers are etched, the film thickness is measured with an ellipsometer at 49 points evenly spaced across the wafer. After processing, the same points are measured again and the etch rate determined.

6.7 The experiment

Three sets of experiments were initially completed. The first involve nine polysilicon wafers etched as the lower grounding impedance was varied from 0 to 60 Ω . The same experiment was completed for the silicon nitride wafers. The experiment was repeated using polysilicon and silicon nitride wafers again with electron density measurements being taken. It was not possible to use the same wafers for the etch rate and electron density measurements due to the fact that the intrusive probe masked the surface of the wafers during the etch process and hence would impact the removal of material from the wafer film. The impact that the by-products of the etch process have on the electron density needed to be measured.

6.8 Results

6.8.1 Etch rate, electron density

Parameters presented are measured as a function of varying ground impedance, Z_g as measured by the VI probe on the lower electrode.

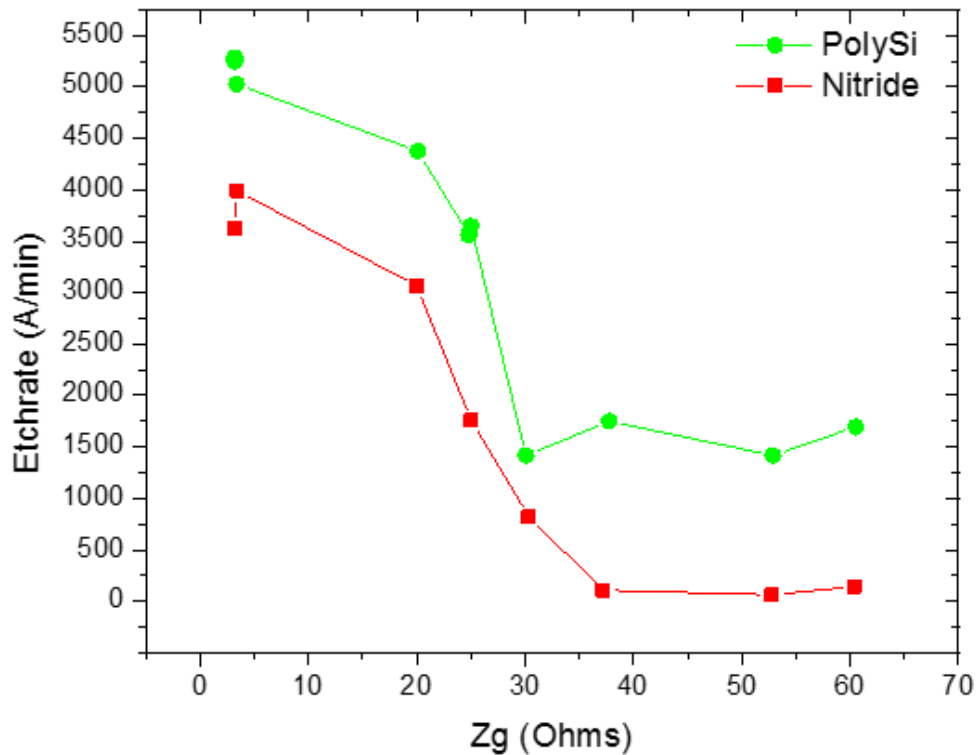


Figure 6-6: Etch rate results for polysilicon and silicon nitride etch rate versus lower ground impedance changes.

The etch rate of both the polysilicon and the silicon nitride wafers are dramatically affected as the lower ground impedance is increased. As the lower impedance is increased from 20 to 30 Ω , the plasma is observed to change mode, from being confined between the two electrodes to expanding to fill the whole chamber. This mode change expansion also affects the etch rate. Once the plasma has expanded to

the walls at 30 Ω , the etch rate of the polysilicon wafers no longer decreases, whereas the silicon nitride wafers etch rate drops to zero. The etching mechanism of silicon nitride involves a sputtering process in which an ion flux is required to break the silicon nitride bonds allowing free fluorine to spontaneously react with the silicon. The etching of polysilicon will be enhanced with ion bombardment but will continue etching in the absence of the ion bombardment as free fluorine will spontaneously react with the silicon surface.

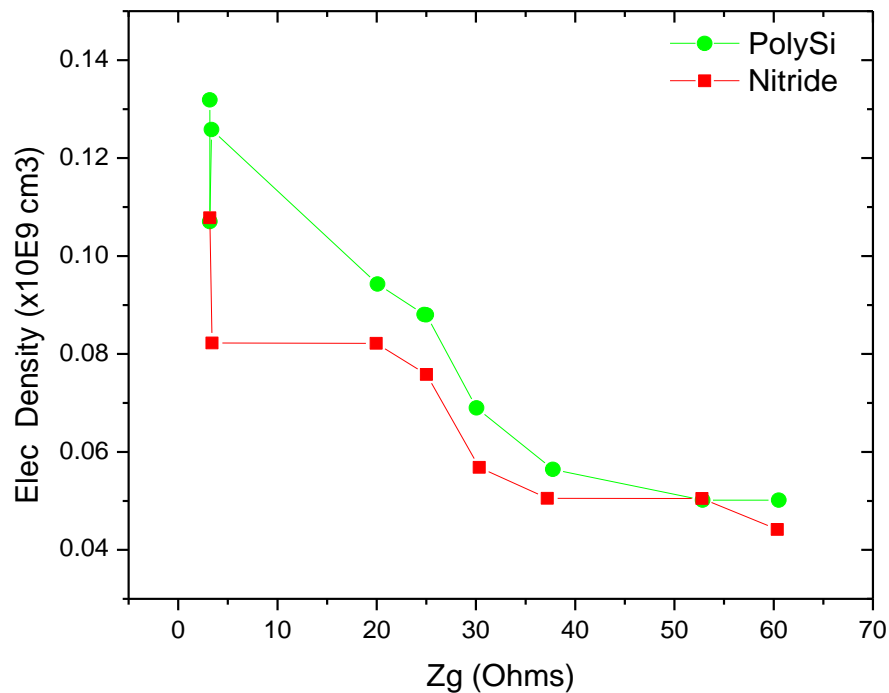


Figure 6-7: Electron density variation with grounding impedance changes for polysilicon and silicon nitride wafers.

Electron density measurements shown in Figure 6-7 also correlate with etch rate and show a rapid reduction in n_e as the impedance is increased and the plasma eventually expands to the wall. The electron density of the silicon nitride process is lower than that of the polysilicon.

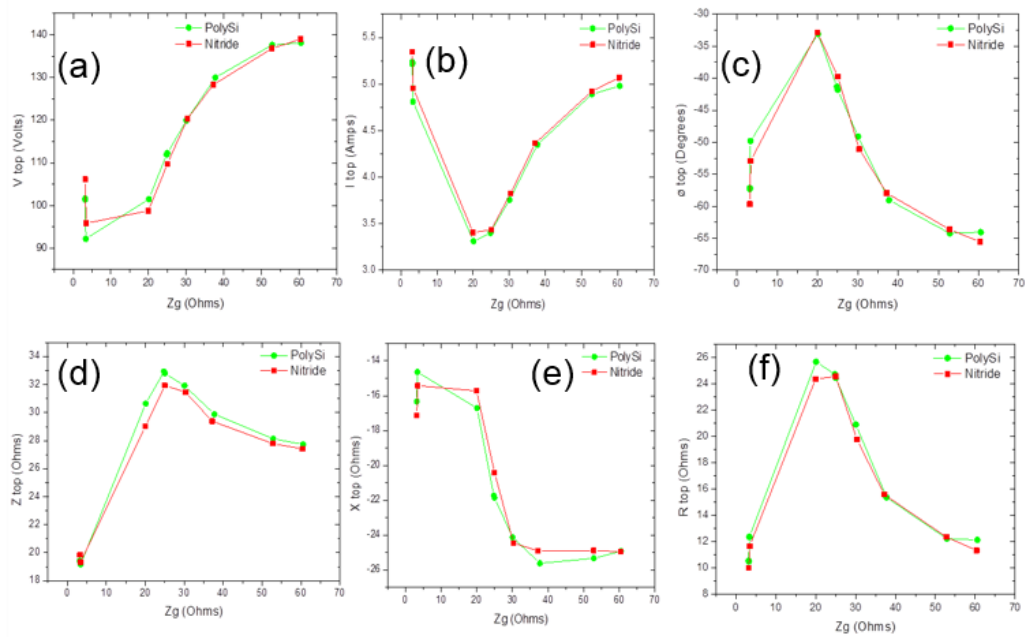


Figure 6-8: Results from the powered electrode VI probe as a function of lower ground impedance.

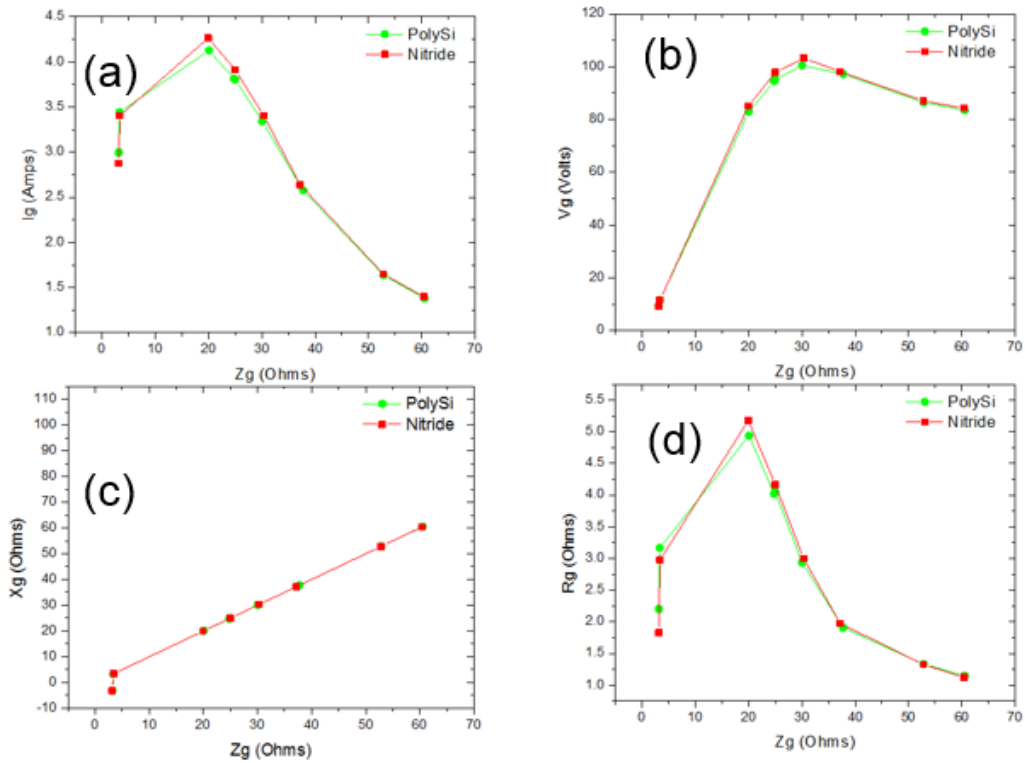


Figure 6-9: Data from the lower electrode VI probe as a function of lower ground impedance.

The VI probe measurements from this experiment are presented in Figure 6-8 and Figure 6-9. The data clearly shows the large mode shift between 20 and 30 Ω ground impedance as the plasma expands to the wall. A detailed investigation of the confined mode 0-30 Z_g is presented in section 6.8.2 .

In the section 6.8.4 experiments are described which help understand what influences the point at which the plasma expands towards the walls.

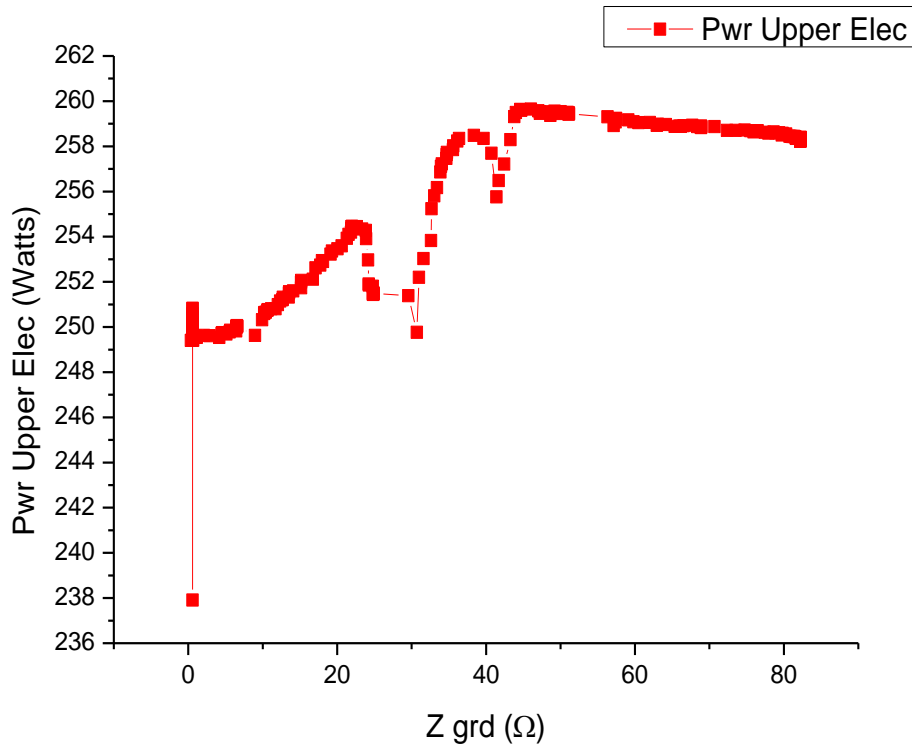


Figure 6-10: Power delivery to the plasma measured at the input to the upper electrode for a RF setpoint of 300Watts to the RF generator with lower ground impedance changes.

The RF power is determined by a set point in the process recipe. This signal is relayed to an RF generator via a 0 to 10 volt analog signal. The RF generator's on board power meter ensures that the output power from the generator matches the set point in the process recipe. Not all the power coming from the RF generator is delivered to the upper electrode and into the plasma. Some of the power is dissipated in the external circuitry. These power losses can be large and variable[62][63]. The RF match unit efficiency varies depending on the operating conditions and the RF current losses. The matching unit needs to provide equal and opposite impedance to the plasma capacitive load and maintain a 50 Ω resistive load to the generator. The

variable load and inductor positions of the match unit change continuously with the different loads presented by the plasma and chamber. The losses are not linear over the entire range of the match unit. In addition, other losses associated with the delivery of power to the upper electrode as well as capacitive leakage to nearby grounding surfaces all contribute to losses, especially at high voltages. In Figure 6-10 the actual delivered power measured by the VI probe is displayed as a function of the changing ground impedance for a fixed 300 W RF setpoint. Losses of up to 50 W are observed.

6.8.2 Electrical behaviour of the confined plasma mode

The data in Figure 6-13 shows detailed measurement of the confined stage of the plasma before expansion to the walls. The etch rate measurements in this experimental run was limited to polysilicon. As stated before, the etch rate negatively changes as the lower impedance is increased. The drop in etch rate begins very rapidly after 14 Ω . In the 0 to 14 Ω region there is little change in etch rate.

In order to explain the behaviour of the discharge in this experiment, a simplified time average electrical equivalency model was constructed and as shown in Figure 6-11. The electrical characteristics of radiofrequency parallel plate capacitively coupled discharges have been widely studied both experimentally and theoretically [6], [14], [64]–[73].

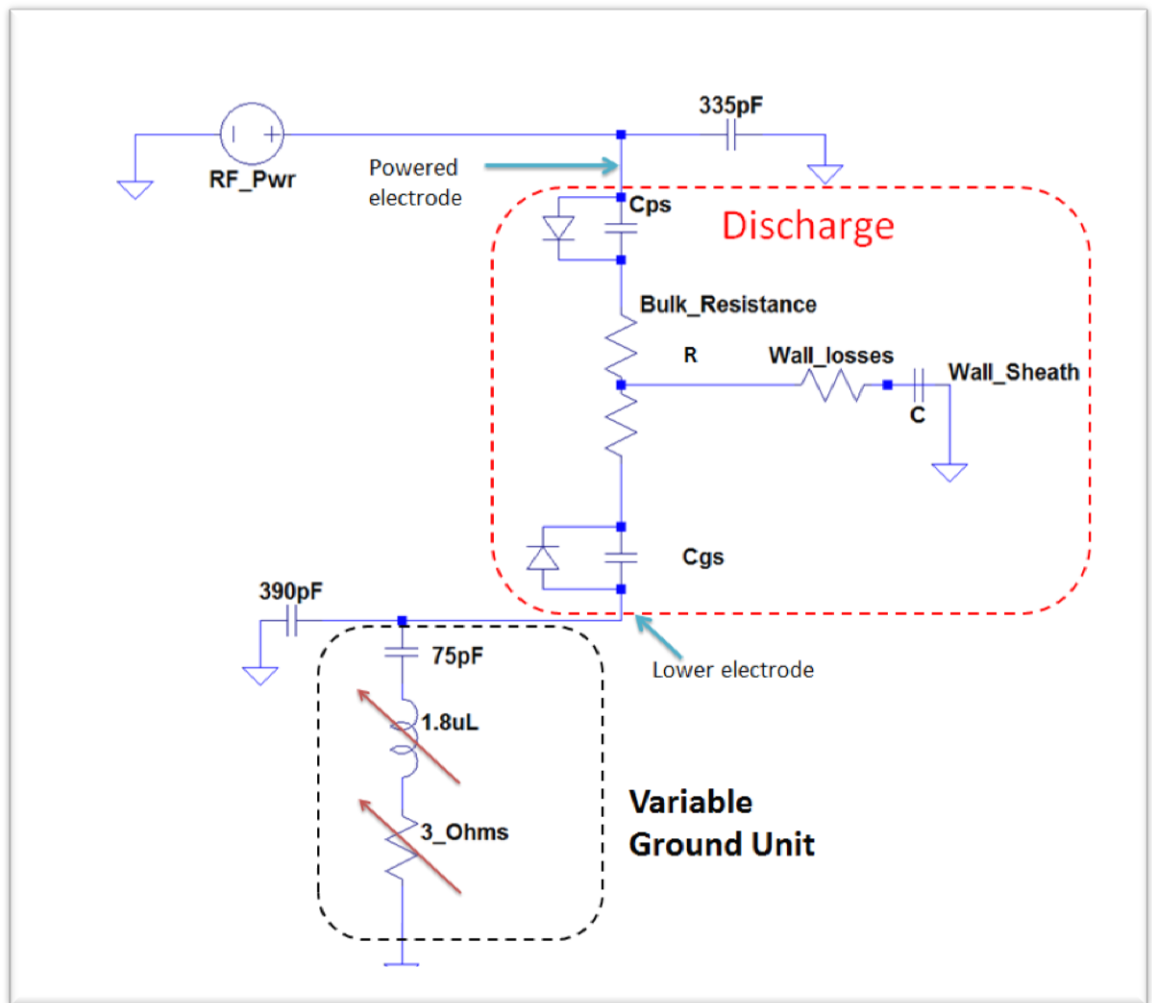


Figure 6-11: Equivalent circuit for simplified electrical model of RF discharge.

A number of assumptions are made as the objective is to capture the basic characteristics and understand the behaviour of the discharge as the lower impedance is changed with respect to the impact these have on the etch rate. The plasma sheaths are considered purely capacitive [69] at 300 mTorr. A number of authors have considered this approach in modelling the electrical characteristics of

the plasma[72]. The resistance of the plasma bulk due to electron-neutral collisions is represented by the bulk resistance in the circuit. The electron diffusion losses towards the chamber walls are represented by a wall losses resistor. This value is considered to be large when the plasma is confined but once the mode shifts to the walls, its resistance drops due to the plasma expansion filling the entire chamber and providing charge carriers facilitating the conduction of current to the walls. The passive wall sheath should have a very high capacitance when the plasma is confined relative to the powered electrode sheath capacitance.

Stray capacitance cannot be ignored. This particular chamber design employs ceramics to insulate the electrodes from the grounding of the chamber housing. As both electrodes are capable of being powered, both are insulated by ceramics rings. To estimate the stray capacitance to ground for the electrode, a small power setpoint of 5.0 watt is delivered to the electrodes and the electrical impedance measured with the VI probes. The electrode gap is increased to 8.0cm and the chamber pressure is reduced to 2.0mTorr with no gas flow. This ensures that no plasma is ignited. The assumption is that the leakage current measured will be capacitively coupled to ground surfaces. Figure 6-12 shows the location of the ground surfaces relative to the powered electrodes and displays the capacitive losses from the analysis of the VI probe data. The resistive losses are in the order of 1Ω .

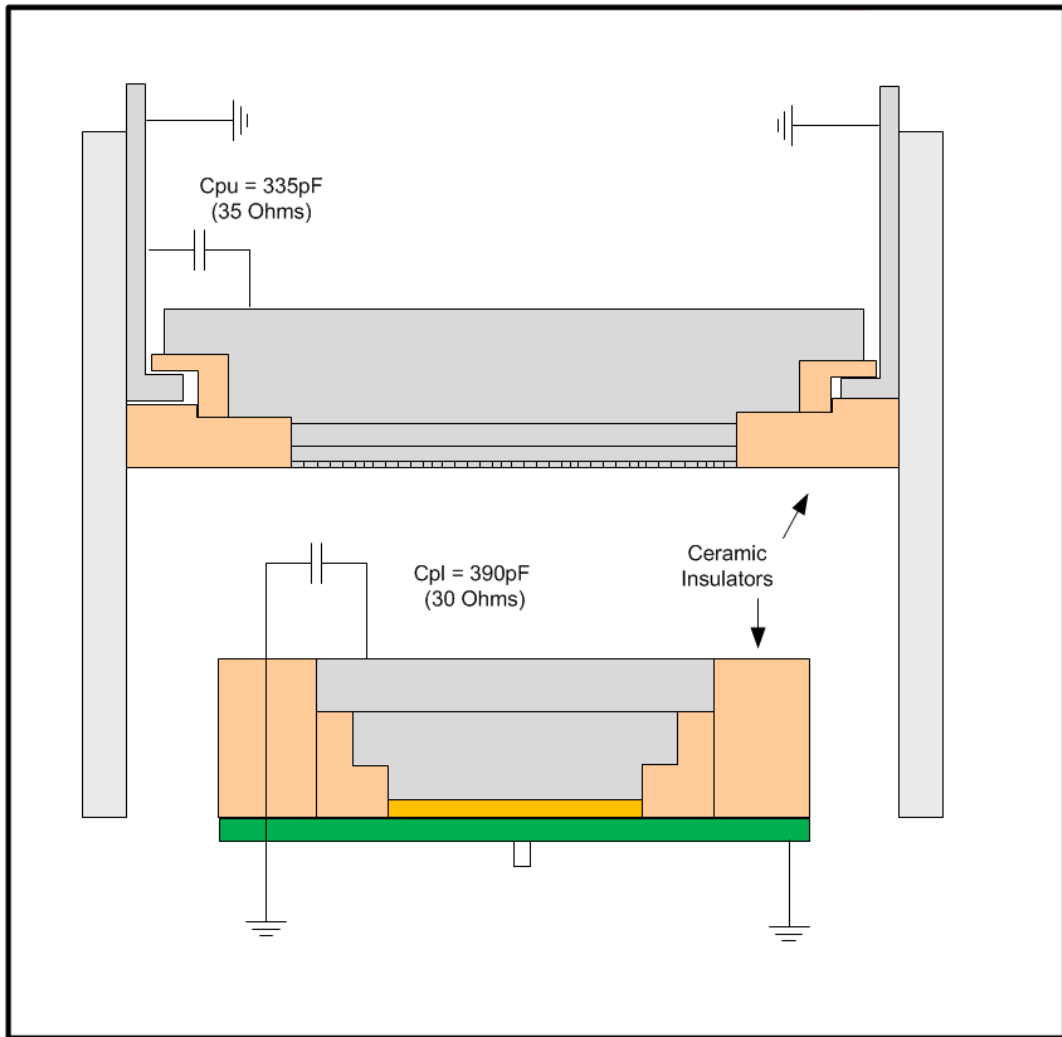


Figure 6-12: Cross section of the RF electrodes showing grounding surfaces and leakage paths. C_{pu} (parasitic capacitance upper electrode) and C_{pl} (lower electrode) are displayed. The actual current paths are not represented in the diagram but the capacitor show to represent the total losses.

Detailed results for the confined plasma mode are presented in Figure 6-13. When the load is varied the power loss in the variable ground unit reaches a maximum of 7.0 watt which is relatively small when compared to the delivered power of 280 W. This is not considered to have a significant effect on the lower etch rate.

The impedance measurement from the VI probe in the upper electrode gives an overall view of the entire impedance of the chamber/plasma combination. From

Figure 6-11 these impedance readings include the variable inductance of the grounding match as well as the capacitance of the two sheaths and the bulk resistance of the plasma. It also includes stray capacitance values between the powered electrode and grounding surfaces in proximity.

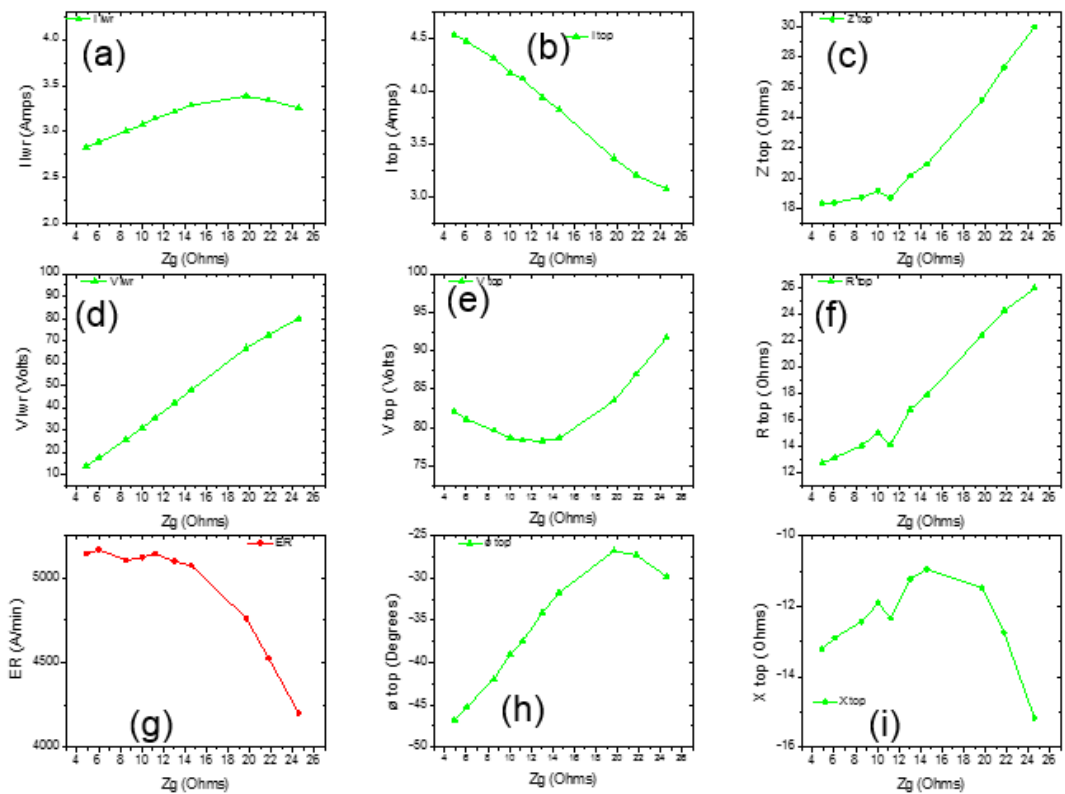


Figure 6-13: The VI probe measurements presenting a detailed mapping of the 0- 25 Ω lower grounding impedance (confined mode).

The current from the upper electrode coupling into the plasma through the powered sheath (I_{top}) decreases from 4.5 A to a minimum of 3.0 A as the variable inductance of the ground Z_g is increased from 0-30 Ω . This decrease in current is in response to the increase in R_{top} . With the power delivery kept constant, the current drops to keep the power constant. The potential V_{top} is influenced by the capacitive X_j impedance of the sheaths. The X_{top} of the circuit drops as the increase in inductance of the lower ground unit resonates out some of the sheath capacitance. This reduction in overall negative reactance X_{top} drives the drop in V_{top} . This imaginary impedance X_{top} is measured from the upper electrode, which includes the two sheaths at the electrodes, the stray capacitance of the upper electrode and lower electrode (which have high values relative to the plasma initially) and the X_g of the variable ground unit. This is reflected in X_{top} and the phase angle measurements in Figure 6-13 which is observed to decrease to a minima of -11 Ω at 14 $Z_g \Omega$. The phase angle which goes from -45 $^\circ$ to -26 $^\circ$ minima at 19 $Z_g \Omega$ ground after which it increases again. The circuit is still dominated by capacitance as the phase angle is still negative. The relationship between the phase angle and R and X_j must be carefully interpreted as the Z_g is increased. The values of R and X_j provide key information regarding the behaviour of the plasma. Figure 6-14 shows how the real and imaginary impedances behave with increasing Z_g . When these two impedances are displayed together it is clear that changes in the resistive properties of the plasma is the predominant impedance change.

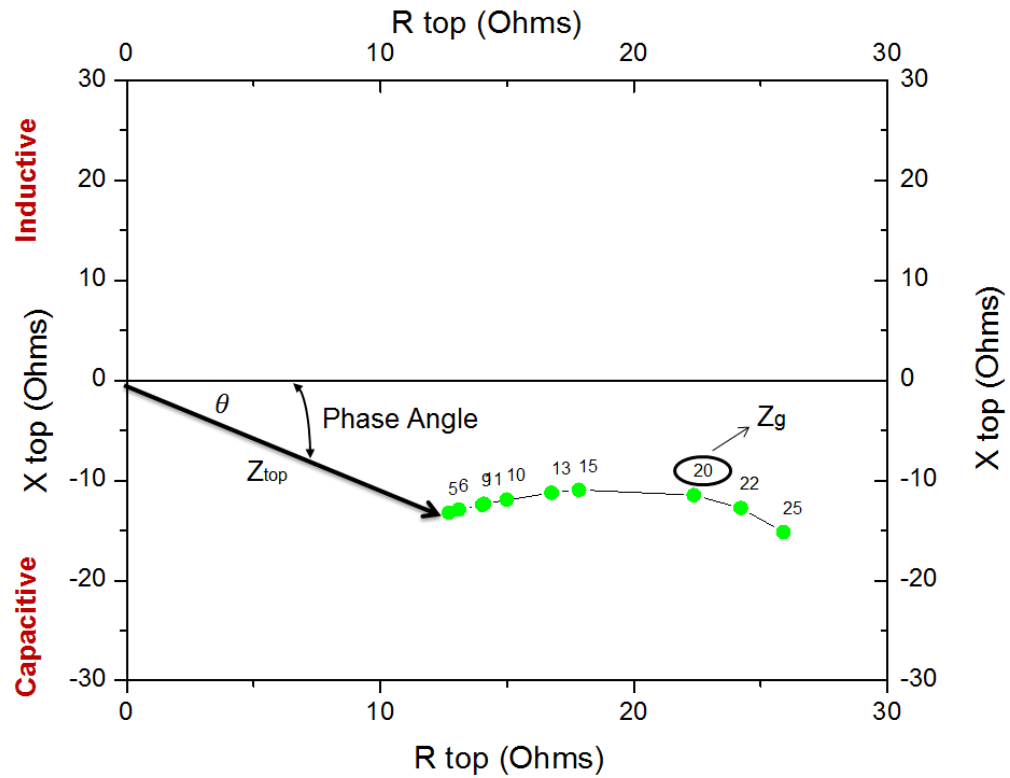


Figure 6-14: Shows the relationship between the real and imaginary impedance. The lower ground impedance is displayed as numbers above each point.

The current through the lower electrode I_{lwr} increases from 2.7 A to a maximum of 3.2 A at 20 Ω lower Z_g . The potential on the upper electrode V_{top} decreases from 82 V to 77 V after a local minimum of 15 Ω Z_g , while the voltage on the ground electrode V_{lwr} , increases from 10-80 V approaching to within 10 V of the powered electrode.

6.8.3 Discussion on confined mode

For the confined mode experiment the current diffusion towards the wall is small and are not considered until the plasma ignites in the entire chamber. The overall

impedance Z_{top} increases slowly from 18-21 Ω as Z_g goes from 0 to 15 Ω . Once Z_g is greater than 15 Ω , Z_{top} begins to increase rapidly. When the components of the total impedance Z_{top} are looked at individually, the resistive component of the circuit R_{top} is also seen to increase with Z_g . One component of this is a small increase in losses in the lower grounding unit, while the other component is the ohmic resistance of the plasma bulk. The imaginary part of the impedance is represented by X_{top} . This reactance decreases from -13 to -9 Ω , the local minimum from where it increases again to -15 Ω . The sheath impedances are not constant and vary with RF current flow through them[72].

When the plasma starts with the Z_g equal to zero, the RF current from the powered electrode travels the path of least resistance to ground through the plasma bulk resistance and lower electrode. Some small current will diffuse towards the walls of the chamber. The distance from the powered electrode to the walls is much greater than to the ground electrode the plasma is contained between the two electrodes. As the ground impedance is increased further it forces more of the current towards the walls and increases the plasma's expansion towards the walls but not all the way to the walls. This is reflected in the increase in the real resistance. This confinement of the plasma is assisted not only by the quenching gas outside the electrode area, but also the reduction in current (I_{top}) driven by the higher resistance and the reduction in V_{top} which will affect the electron heating. This regime continues until, finally, so much current is forced to the walls by the very high impedance of the ground path that there are enough high energy electrons to create and sustain a discharge all the

way to the walls and the resistance is observed to drop dramatically due to the high availability of charge carriers.

The voltage, V_{lwr} , on the lower electrode increases with the increasing ground impedance ultimately approaching within 10 Volts of the plasma potential. This reduction in the potential between the plasma potential and electrode reduces the ion flux to the wafer surface ultimately to near zero when the plasma expands. This hypothesis is supported by the etch rate results in Figure 6-6 where the etch rate of silicon nitride, which is highly dependent on ion bombardment to break the tightly bonded Si_3N_4 lattice, drops to zero indicating no significant ion flux to the wafer surface.

The current, I_g , measured by the VI probe in the lower ground circuit increases (Figure 6-13) with the ground impedance. The circuit below the lower electrode consists of the variable inductor in series with the three 25 pF capacitors in parallel with the 390 pF stray capacitance to ground. This becomes a resonance circuit as the inductor begins resonating with the stray capacitance. The oscillating voltage on the lower electrode, which has increased with the Z_g , drives this resonant circuit. The DC bias measured on the lower electrode in Figure 6-15 also increases rapidly and approaches 0 V as electrons are no longer attracted by any potential between the lower electrode and the plasma potential. Again, the loss of this DC bias also reduces any attraction ions might have to the wafer surface.

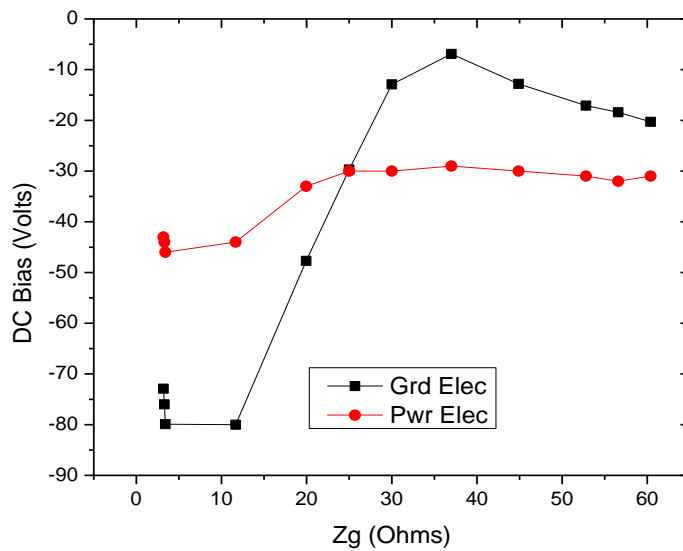


Figure 6-15: DC bias readings for both upper powered electrode and ground electrode as function of ground impedance changes.

6.8.4 Plasma expansion to the wall

As the lower ground impedance is increased above 20 Ω , the majority of current is forced to the walls. However, since the plasma has not expanded to the walls the availability of charge carriers to conduct the current to the walls is very low resulting in a very high resistive impedance. In order to establish a discharge outside of the electrode area, there needs to be a sufficient quantity of high energy electrons to initiate and sustain a discharge in the entire chamber. In the SF₆/He discharge, two mechanisms work against this process of creating additional electrons to initiate the discharge. Firstly, the very high ionization potential of helium of 24.6 eV means that few electrons have sufficiently high energy for this ionization processes. Secondly, collisions of electrons with SF₆ further reduces density of electrons due to electron

attachment. Both these mechanisms serve to quench the discharge from expanding beyond the electrode area until electric fields are high enough to sustain high energy electrons. However, as the voltage in the lower electrode approaches that of the plasma potential, the electric field gradient shifts away from the lower electrode towards the walls [74]. This modified electric potential drives more of the current towards the walls and increases the ionization at the edge of the plasma facilitating the expansion of the discharge towards the walls. The resultant reduction in resistance facilitates more current to flow towards the walls allowing the plasma to expand further. This process reaches a critical point where the specific density and temperature (EEDF) of the electrons overcomes the loss mechanism and the plasma expands all the way to the walls. This sudden transition can be clearly seen in the electrical measurements in Figure 6-16. The reactance X_{top} shows the most dramatic shift with a large increase in impedance from -12 to -18Ω when the ground impedance reaches 25Ω . This dramatic shift occurs because the current has now established a lower resistive path to ground through the plasma to the walls as opposed to the lower electrode's circuit. The inductive component of the lower electrode circuit no longer dominates the imaginary impedance and its impact in resonating with the capacitance of the sheaths no longer serves to reduce the overall imaginary impedance. The inclusion of the wall sheath capacitance in the circuit also serves to drive X_{top} lower. This is seen most predominantly on the X_{top} versus R_{top} graph in Figure 6-16. The real resistance of the circuit begins to drop due to the availability of charge carriers in the bulk plasma which now stretches all the way to the walls, the overall current I_{top} begins to increase again.

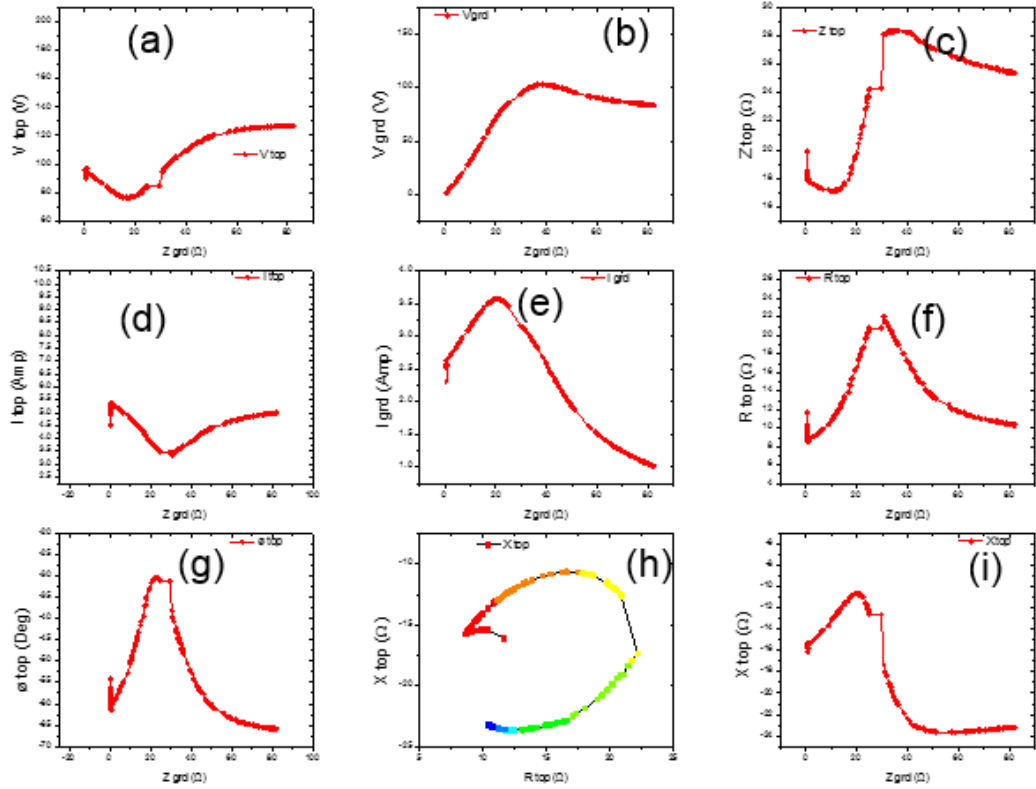


Figure 6-16: The current voltage characteristics of the discharge as the ground path impedance is increased from 0 to 80 Ω and the plasma expands all the way to walls.

The turning point where the plasma suddenly expands to the walls was investigated under different operating conditions. The graph of X_{top} versus R_{top} is an effective way of displaying the expansion point.

Figure 6-17 displays the electrical characteristics with changing RF power. All other process recipe setpoints were unchanged. At the RF power of 200 W run, the plasma expansion is delayed until the ground impedance reaches 25 Ω and the expansion change is dramatic, whereas at 600 Watts the plasma can easily expand to the wall and the transition is less pronounced. The electron density measured with the hairpin probe shows an increases in n_e with RF power. The increase in electron density with

higher power overcomes the quenching mechanisms and hence can strike the discharge outside of the electrode area [13] more easily.

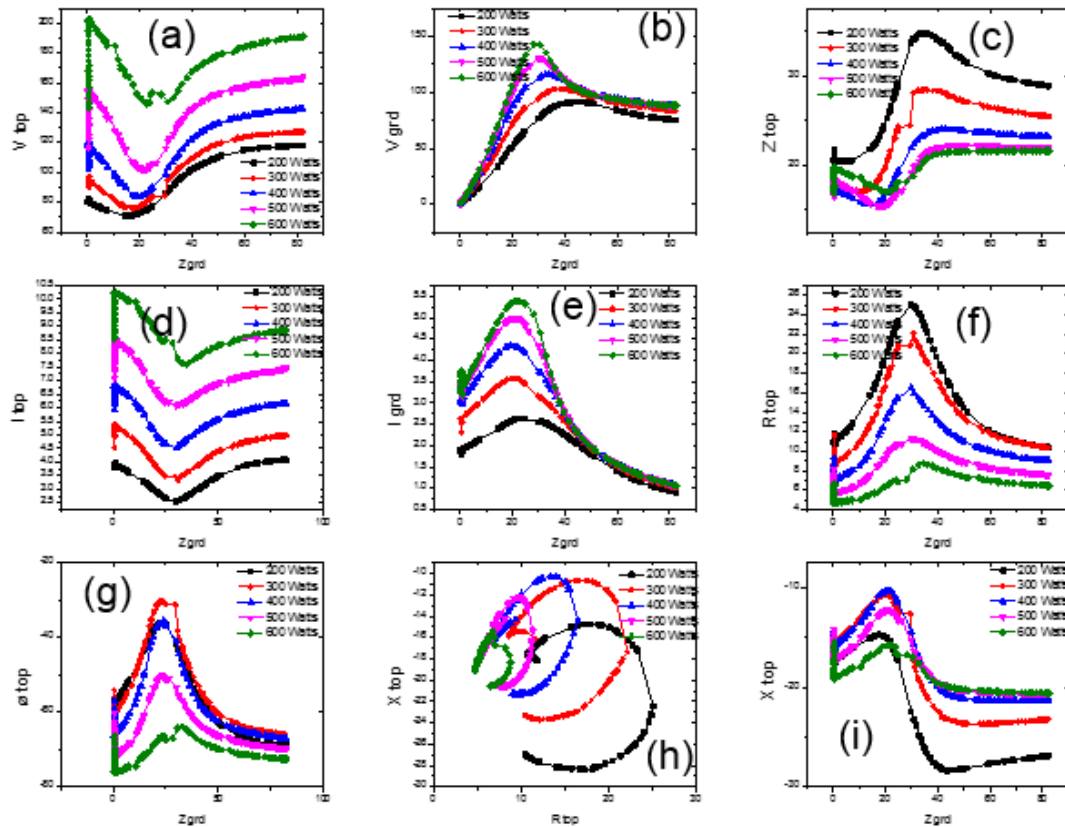


Figure 6-17: The current voltage characteristics of the discharge as the ground path impedance is increased all the way to 80 Ω , the plasma expands all the way to walls for RF power changes from 200-600Watts.

In Figure 6-18 the effect of pressure is shown. At 125 mTorr the larger mean free path resulting in higher electron temperature, T_e . In this regime the plasma can expand easily to the walls as the probability of an electron colliding before reaching the walls is lower, hence, it is able to initiate a discharge outside the electrode area more effectively. The effect of changing the lower ground impedance at low pressure is less dramatic than at higher pressures when a plasma is contained by the

quenching mechanisms. As the pressure is increased the resistive impedance of the discharge increases as the electrons collision rate increases.

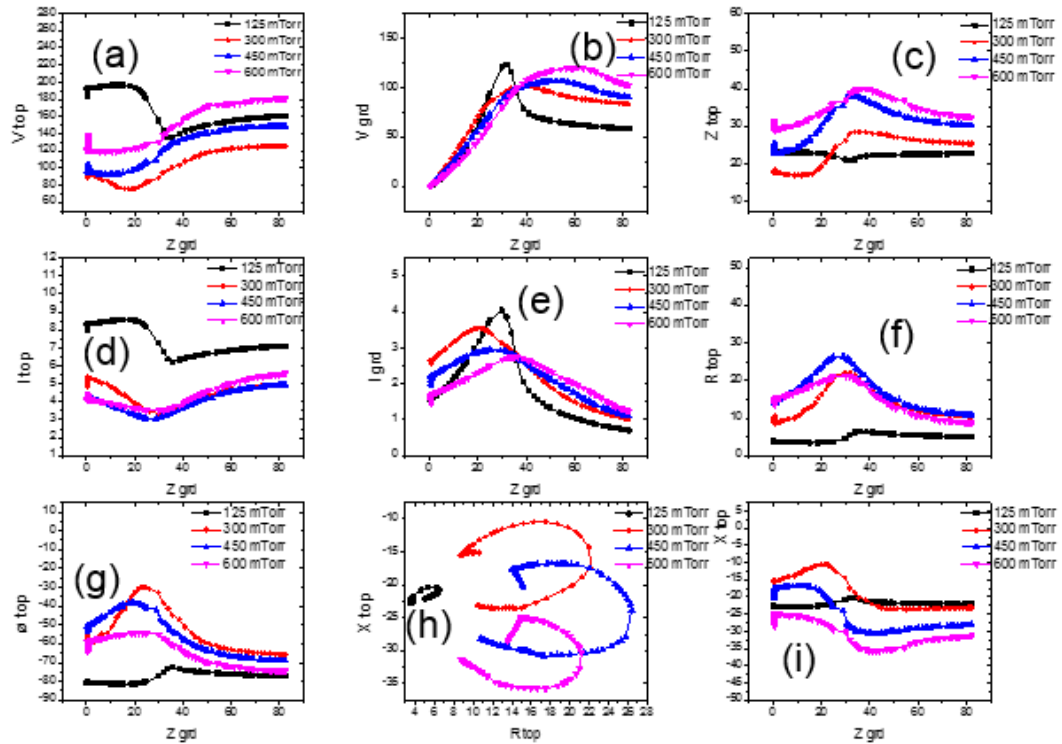


Figure 6-18: The current voltage characteristics of the discharge as the ground path impedance is increased all the way to 80 Ω , the plasma expands all the way to walls for pressure setting 125-600mTorr.

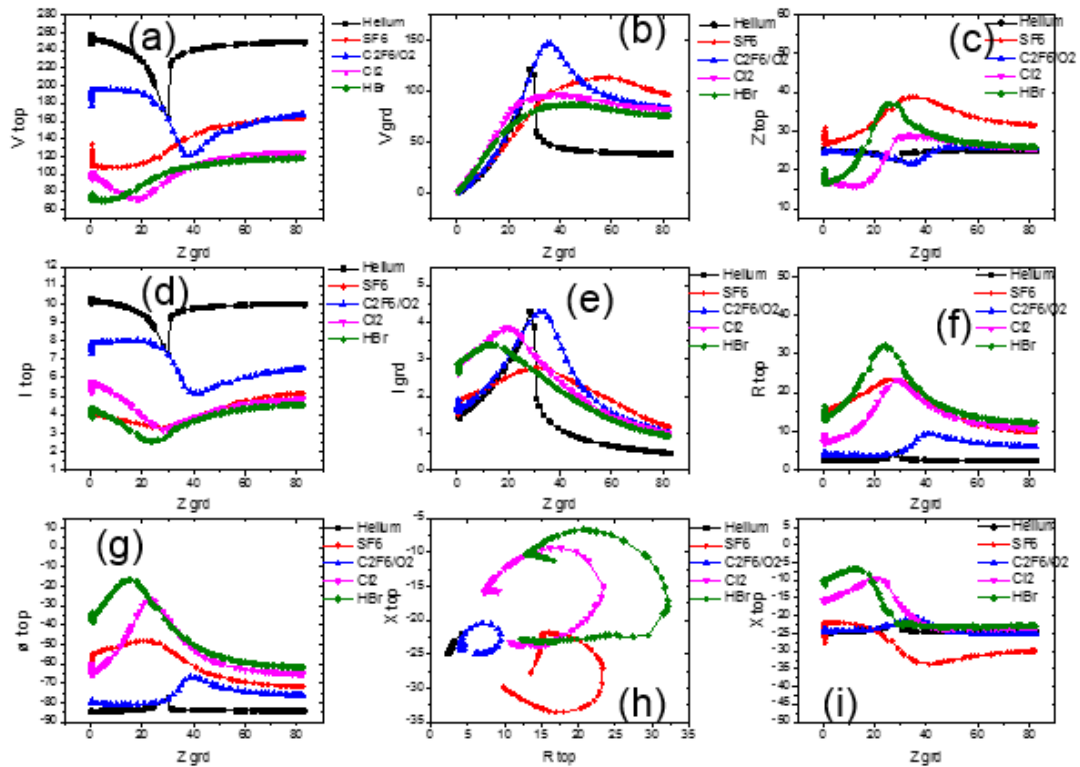


Figure 6-19: The current voltage characteristics of the discharge as the ground path impedance is increased all the way to 80 Ω the plasma expands all the way to walls for different gas mixtures.

A number of different process chemistries are presented in Figure 6-19. In this experiment each gas was tested individually over a range of ground path impedances. Helium which has a very small cross-section for ionization and requires high energy Te electrons to ionize the discharge, which manifests, in high electrode voltages and currents and low resistance. This type of discharge is easily able to expand to the walls resulting in very little impact in switching from the lower electrode grounding to the expanded mode grounding on the chamber walls. However, the expansion mode switch is much more dramatic for helium. In comparison, HBr, which has an ionization threshold of 11.8 eV, is more readily ionized than helium, but is also electronegative and absorbs electrons due to electron attachment. In the HBr

discharge the expansion to the wall is much more gradual and less pronounced. The C_2F_6/O_2 discharge does not expand to the walls until the ground path exceeds 40Ω .

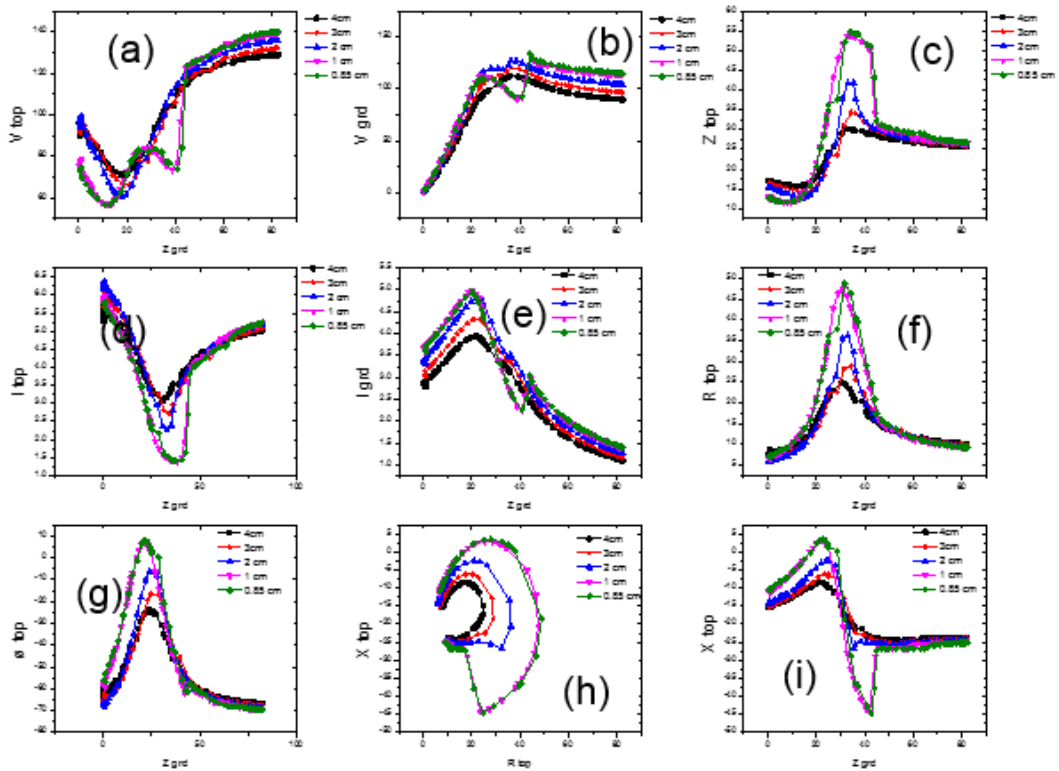


Figure 6-20:The current voltage characteristics of the discharge as the ground path impedance is increased all the way to 80Ω as the plasma expands all the way to walls for gaps changes from 4-0.85 cm.

The process chosen for all experiments in the chapter was at an electrode spacing of 5.0 cm, this is purely to facilitate the insertion of the hairpin probe into the discharge for the electron density measurements. Typically, manufacturing processes on this type of hardware typically run with a very low gap of less than 1 cm. The process uniformity from the centre to the edge of the wafer is better for low gap settings. In Figure 6-20 the results of five gap settings are presented. For normal operating mode with the ground impedance at zero, the main effect of changing the gap is seen in

V_{top} and a reduction in the capacitive impedance. This result suggests a reduction in the sheath thickness as the gap decreases.

As the ground path resistance is increased for gap settings of less than 1 cm it reaches a point where the phase angle goes to zero as the inductor fully resonates the capacitance of the sheaths while the plasma is in a confined mode. The electrical circuit becomes inductive for a short time. The plasma has a very high resistance of up to 48Ω in this regime. With the very low gap between the two electrodes, expansion to the wall is delayed significantly due to the very low diffusion of current between the small spacing of the electrodes.

6.9 Conclusion

In this chapter an investigation was conducted on the impact the chamber's hardware has on electrical characteristics and etch rate performance. The impact that the chamber's electrical characteristics has on etch rate was studied by introducing a variable inductor in the RF ground path. Changing this ground impedance significantly affected the etch rate performance of the process chamber. It was found that the overall electrical characteristics of the discharge and chamber combination dramatically impacted the plasma parameters of an industrial plasma etcher. The impact on the chamber impedance has on the electron density and the ion energy bombarding the wafer is significant enough to change the etch performance of the chamber. While many of the experiments were performed at a large gap of 5 cm, electrical changes were far more sensitive at low gap spacing compared to large gap spacing. Since this is where industrial processes normally operate, it is anticipated

that even small changes to the electrical characteristics of the chamber have a significant impact on process repeatability as observed in production. In particular, it assesses the impact that routine maintenance has on process stability as a result of electrical differences before and after maintenance activity. For example, there is considerable movement allowable in the centring of the upper electrode assembly in the gap barrel. It has been shown in other studies that etch rate performance can be modulated by positioning of the upper electrode relative to the grounding walls. Electrical impedance measurements have been used post maintenance to measure the electrical integrity of the chamber. A plasma impedance test in argon discharge has been used to fingerprint electrical characteristics of the chamber before committing to conditioning and etch rate monitoring post maintenance. This technique is also being used for chamber to chamber matching. In particular, inert discharges can be used to fingerprint and compare the electrical impedances of chambers across a fleet of tools. Using an inert plasma decouples the effect of the plasma chemistry and/or wall conditioning which may contribute to chamber differences. While the process recipe calls for a certain amount of RF power to be delivered from the RF generator, the way the power is coupled into the plasma and the impact the real and imaginary impedances have on the resultant RF voltage and current can dramatically affect the etching process.

Chapter 7

Conclusion and further work

7.1 Virtual metrology

Virtual metrology modelling of plasma etch processes has been demonstrated in this thesis. Research in virtual metrology has examined many different statistical approaches to modelling industrial processes but no clear advantageous approach has emerged. The conclusion of this work completed in this thesis is that the measurement of the process accurately, with the appropriate sensors, is fundamental to being able to predict metrology. In particular, the sensors need to be able to measure the variability in the process that is responsible for the physical and chemical variation that is driving the variation in the physical dimensions of the etched features. If this can be achieved to a high level, with passive sensors that don't perturb the process, then any number of statistical approaches can build correlations between the measured variability of the process and the resultant variation in metrology. There are still limitations in the ability to predict metrology from sensor data when the process deviates outside of the learnt behaviour. This problem was dealt with in the workflow design in Chapter 5.3, where, the outlier detector can act as a go no-go to allow the prediction of metrology.

Metrology will always be needed in order to construct an initial model and for periodic retraining. Virtual metrology does offer the opportunity to significantly reduce the amount of metrology needed, especially in a high-volume manufacturing fab where significant savings could be made by reducing the metrology

measurements particularly in operations where on target metrology is not necessary. However, the most important finding of this research lies in the value of the diagnostics that the modelling approach provides. The ranking of the variables most responsible for the variation in the data (principal component analysis) and those most correlated to the variation in metrology is key information for process engineers. Combining this list of variables with engineering know how and designing of experiments, the root cause of process variability can be determined.

In modern processes, the dimensions of device structures measured at the metrology operations are influenced by multiple upstream process steps. This makes the metrology more convoluted with contributions of each of the different process steps to the variation observed in the metrology. In this case, combining sensor data from each process operation with the final metrology becomes a very powerful diagnostic capability in which the modelling approach can rank the important variables that are most correlated to the variation metrology. This insight into the integrated manufacturing problems seen in many fabs provides critical information to engineers to develop control strategies to minimize the variation.

Knowing the correlation between the sensor variables and the metrology presents a significant advantage over unsupervised fault detection where the distribution of all the variables is monitored with statistical limits. The implementation of fault classification in the semiconductor industry has relied on teaching fault patterns to create a library and comparing incoming wafers to those fault patterns. This approach requires significant overhead in teaching faults to build the library and maintaining

and managing libraries adds complexity and cost. Transferring libraries from chamber to chamber has not been completely successful.

The next level of value is in process diagnostics which was discussed earlier. Tool/chamber matching can be achieved by building independent models for each chamber in order to determine key variables driving the variation in metrology in each chamber. With the same process running on both chambers, these key variables should be the same in all chambers. If this approach is applied to multiple chambers running the same processes where a “rogue” chamber’s process performance can be compared to good chambers.

The requirement of better control of etch plasma processes is becoming more and more important as device feature sizes are reduced. More and more process control is being implemented in semiconductor factories. Run to run process control requires a model to know how the output of a process (metrology) is related to the process recipe setpoint. The controller uses downstream metrology results and modifies recipe inputs to keep a process on a target. One or two recipe variables are used to offset variation in the process chamber performance. Run to run process control is also used to mitigate any incoming variation in metrology. Since controller uses the past performance of the process chamber it is very dependent on the fast availability of metrology from the previous wafers that ran on the chamber to update the EEMA (effective weight moving average). The ability to predict metrology at the end of every wafer process and feed this data to the EEMA offers a distinct advantage to a run to run controller as it increases the availability of metrology enabling the run to

run controller to mitigate variation (drift) and achieve on target metrology more effectively.

However, there are still a number of key technical challenges that need to be overcome for large-scale industrial adoption of this technique as an alternative to classical metrology measurements.

7.2 Equipment hardware diagnostics

Chapter 6 demonstrated the impact that the electrical characteristics of the chamber hardware can have on the process performance. Maintenance activities in the semiconductor fab where chambers are disassembled for cleaning have a negative impact on the repeatability of the process performance. There is a significant risk associated with performing intrusive but necessary maintenance which can affect the chamber's process performance. There is a significant advantage in having electrical measurements of the process chamber hardware using impedance measurements. The obvious and most practical measurements involve VI probes or other RF tuning characteristics which can establish an electrical baseline from which to compare before and after maintenance. Another approach, not discussed in this thesis investigated was the use of frequency domain reflectometry [75]. This technique involves the injection of a sweeping 100 Hz to 4 GHz signal into the etcher and the measurement of the reflections. A unique fingerprint of the reflection points of the hardware can be measured and used to build a baseline. Running argon only discharges can decouple the complex interactions that electronegative and reactive gases have on the impedance measurements. This technique has been very successful at generating electrical fingerprints of the chambers hardware that can be used to

evaluate the impact of maintenance and chamber to chamber matching. The impedances of the chamber with no plasma (very low RF power) can also be used to baseline the chamber hardware's stray impedances.

7.3 Process control- Further work

As the semiconductor process becomes more difficult, even run to run controllers cannot keep processes on target. The requirement to control the process real-time is fast becoming a needed reality. The ability to control etch rate in real time using a predictive control schema was demonstrated to be very effective at mitigating the effect of disturbances to the RF ground path[76][77]. A virtual metrology model was used to estimate the etch rate real-time from the VI probe measurements of the plasma. This data was fed real-time into a control schema which then mitigated any shift in etch rate by controlling the RF generator's power output. Disturbances were introduced by changing the lower ground impedance, as detailed in chapter 6, which have been shown to have a significant impact on the etch rate. This control schema is very effective at compensating for these impedance changes on the etch rate by adjusting the RF power in real-time. These results demonstrate that large disturbances to the process can be rejected by the controller.

This real-time virtual metrology model does require training over a wide process parameter space and the sensors need to have very good correlation to the variation in metrology. This approach offers the ability to retrain the models from production wafers and improve over time. The control model can react to changes very quickly and can handle a lot of variation in processing conditions. Additional work would

need to be completed to evaluate this approach and its suitability for high-volume manufacturing. In particular, the introduction of multiple disturbances, including wall effects, and how that would impact a controller's ability to keep the etch rate on target would need to be studied.

A second approach to real time process control is to control the individual plasma [78] parameters and species densities in real-time. Multivariable closed loop control is being investigated and has shown very promising results. The real challenge is to adapt and harden these techniques so that they are robust enough for industrial use.

- [1] I. Langmuir, "Oscillations in ionized gases" *Phys. Rev.*, vol. 14, pp. 627–637, 1929.
- [2] K. Kohler, J. Coburn, and D. Horne, "Plasma potentials of 13.56- MHz rf argon glow discharges in a planar system" *J. Appl. Phys.*, 1985.
- [3] Robertus Johannes Maria Mathilde Snijkers, "Snijkers 1993 PhD thesis - The sheath of an RF plasma_ measurements and simulations of the ion energy distribution" Eindhoven University of Technology, 1993.
- [4] Michael A. Liebermann and Allan J. Lichtenberg, *Principles of plasma discharges and materials processing*. Wiley Interscience, 1994.
- [5] D. Gahan, B. Dolinaj, and M. B. Hopkins, "Retarding field analyzer for ion energy distribution measurements at a radio-frequency biased electrode." *Rev. Sci. Instrum.*, vol. 79, no. 3, p. 033502, 2008.
- [6] E. Kawamura, A. Wu, M. Lieberman, and A. Lichtenberg, "Stochastic heating in RF capacitive discharges" 2006.
<http://www.eecs.berkeley.edu/~lieber/EmiKHeating27Apr05.pdf>
- [7] M. a. Lieberman and V. a. Godyak, "From Fermi acceleration to collisionless discharge heating" *IEEE Trans. Plasma Sci.*, vol. 26, no. 3, pp. 955–986, Jun. 1998.
- [8] F. Julian, "Electron heating in capacitively coupled radio frequency discharges, PhD Thesis" University of Bochum, 2009.
- [9] J. V. Scanlan, "Langmuir probe measurements in 13.56 MHz discharges, PhD Thesis" Dublin City University.
- [10] M. Sugawara, *Plasma Etching, Fundamentals and Applications*. Oxford University Press, 1998.
- [11] B. Chapman, *Glow Discharge Processes*. John Wiley & Sons, 1980.
- [12] V. Vahedi, "Modeling and Simulation of RF Discharges Used for Plasma Processing, PhD Thesis" Harvard, 1993.
- [13] Z. Navrátil, P. Dvořák, O. Brzobohatý, and D. Trunec, "Determination of electron density and temperature in a capacitively coupled RF discharge in neon by OES complemented with a CR model" *J. Phys. D. Appl. Phys.*, vol. 43, no. 50, p. 505203, Dec. 2010.
- [14] A. J. Lichtenberg, V. Vahedi, M. A. Lieberman, and T. Rognlien, "Modeling electronegative plasma discharges" *J. Appl. Phys.*, vol. 75, no. 5, p. 2339, 1994.

- [15] M. Turner and M. Hopkins, "Anomalous sheath heating in a low pressure rf discharge in nitrogen" *Phys. Rev. Lett.*, vol. 69, no. 24, pp. 3511–3514, 1992.
- [16] M. Klick, W. Rehak, and M. Kammeyer, "Plasma diagnostics in rf discharges using Non Linear resonance effects" *Jpn. J. App. Phys.*, vol. 36, 1997.
- [17] J. Tanaka and G. Miya, "Spatial profile monitoring of etch products of silicon in HBr/Cl/O/Ar plasma" *J. Vac. Sci. Technol. A Vacuum, Surfaces, Film.*, vol. 25, no. 2, p. 353, 2007.
- [18] D. L. Flamm, "Mechanisms of silicon etching in fluorine- and chlorine-containing plasmas" *Pure Appl. Chem.*, vol. 62, no. 9, pp. 1709–1720, 1990.
- [19] D. L. Flamm and V. M. Donnelly, "The design of plasma etchants" *Plasma Chem. Plasma Process* vol. 1, no. 4, pp. 317–363, 1981.
- [20] S. Sivakumar, "Lithography Challenges for 32nm Technologies and Beyond" *2006 Int. Electron Devices Meet.*, pp. 1–4, 2006.
- [21] M. El kodadi, S. Soulan, M. Besacier, and P. Schiavone, "Resist trimming etch process control using dynamic scatterometry" *Microelectron. Eng.*, vol. 86, no. 4–6, pp. 1040–1042, 2009.
- [22] Y. Zhang, G. S. Oehrlein, and F. H. Bell, "Fluorocarbon high density plasmas . VII . Investigation of selective SiO₂ -to-Si₃N₄ high density plasma etch processes" *J. Vac. Sci. Technol. A*, vol. 14, no. July 1995, pp. 2127–2137, 1996.
- [23] M. Schaepkens and G. S. Oehrlein, "Selective SiO₂ to Si₃N₄ etching in inductively coupled fluorocarbon plasmas : Angular dependence of SiO₂ and Si₃N₄ etching rates" *J. Vac. Sci. Technol. A*, pp. 3281–3286, 1998.
- [24] M. Schaepkens, T. E. F. M. Standaert, N. R. Rueger, P. G. M. Sebel, G. S. Oehrlein, and J. M. Cook, "Study of the SiO₂ to Si₃N₄ etch selectivity mechanism in inductively coupled fluorocarbon plasmas and a comparison with the SiO₂-to-Si mechanism" *J. Vac. Sci. Technol. A Vacuum, Surfaces, Film.*, vol. 17, no. 1, p. 26, 1999.
- [25] L. Chen, L. Xu, D. Li, and B. Lin, "Mechanism of selective Si₃N₄ etching over SiO₂ in hydrogen-containing fluorocarbon plasma" *Microelectron. Eng.*, vol. 86, no. 11, pp. 2354–2357, Nov. 2009.
- [26] M. Matsui, T. Tatsumi, and M. Sekine, "Relationship of etch reaction and reactive species flux in C₄F₈/Ar/O₂ plasma for SiO₂ selective etching over Si and Si₃N₄" *J. Vac. Sci. Technol. A Vacuum, Surfaces, Film.*, vol. 19, no. 5, p. 2089, 2001.

- [27] R. Westerman and D. Johnson, "Endpoint detection methods for time division multiplex etch processes" in *Micromachining and Microfabrication Process Technology XI*, 2006.
- [28] N. MacGearailt, "Endpoint via NMACG" Internal Report, Intel Ireland 1998.
- [29] M. Darnon, C. Petit-Etienne, E. Pargon, G. Cunge, L. Vallier, P. Bodart, M. Haas, S. Banna, T. Lill, and O. Joubert, "Synchronous Pulsed Plasma for Silicon Etch Applications" *ECS Trans.*, vol. 27, no. 1, pp. 717–723, 2010.
- [30] J. P. Chang and H. H. Sawin, "Notch formation by stress enhanced spontaneous etching of polysilicon" *J. Vac. Sci. Technol. B Microelectron. Nanom. Struct.*, vol. 19, no. 5, p. 1870, 2001.
- [31] H. G. Kosmahl, "Plasma Acceleration with Microwaves near Cyclotron Resonance" *J. Appl. Phys.*, vol. 38, no. 12, p. 4576, 1967.
- [32] Y. Gotoh and T. Kure, "Microwave Plasma Etching" *Jpn. J. Appl. Phys.*, vol. 34, pp. 2132–2136, 1995.
- [33] Y. Yoshizako, M. Taniguchi, and Y. Ishida, "Microwave power source apparatus for microwave oscillator comprising means for automatically adjusting progressive wave power and control method therefor" *US Pat. 5,399,977*, 1995.
- [34] F. Chen, "High Density Plasma Sources" US Patent 4,778,561, 1995.
- [35] R. L. Kinder and M. J. Kushner, "Consequences of mode structure on plasma properties in electron cyclotron resonance sources" *J. Vac. Sci. Technol. A Vacuum, Surfaces, Film.*, vol. 17, p. 2421, 1999.
- [36] R. L. Kinder and M. J. Kushner, "Simulations of ECR processing systems sustained by azimuthal microwave TE_(0n) modes" *25th Anniv. IEEE Conf. Rec. - Abstr. 1998 IEEE Int. Conf. Plasma Sci. (Cat. No.98CH36221)*, 1998.
- [37] "Semiconductor Equipment and Materials International"
<http://www.semi.org>.
- [38] N. MacGearailt, "Endpoint of <0.5 % open area with a VI sensor, Internal Report, Lam Ireland" 1998.
- [39] N. Dewan, "Analysis and modelling of the impact of plasma RF harmonics in semiconductor plasma processing, PhD Thesis" Dublin City University, 2001.
- [40] M. B. Hopkins and J. F. Lawler, "Plasma diagnostics in industry" *Plasma Phys. Control. Fusion*, vol. 42, no. 12B, pp. B189–B197, Dec. 2000.

- [41] R. L. Stenzel, "Microwave resonator probe for localized density measurements in weakly magnetized plasmas" *Rev. Sci. Instrum.*, vol. 47, no. 5, p. 603, 1976.
- [42] N. a Campbell and W. R. Atchley, *The geometry of cacnonical variate analysis*, vol. 30. Syst. Zool, 1981, pp. 268–280.
<http://sysbio.oxfordjournals.org/>
- [43] "PCA Diagram"
<http://web.media.mit.edu/~tristan/phd/dissertation/chapter5.html>.
- [44] <http://umetrics.com/>.
- [45] J. E. Jackson, "A Users Guide to principle components" 1991
<http://onlinelibrary.wiley.com/doi/10.1002/0471725331.fmatter/pdf>.
- [46] "Private Correspondance with Dr. Eugene Tuv"
- [47] J. Conway, S. Kechkar, N. O' Connor, C. Gaman, M. M. Turner, and S. Daniels, "Use of particle-in-cell simulations to improve the actinometry technique for determination of absolute atomic oxygen density" *Plasma Sources Sci. Technol.*, vol. 22, p. 045004, 2013.
- [48] H. M. Katsch, A. Tewes, E. Quandt, A. Goehlich, T. Kawetzki, and H. F. Döbele, "Detection of atomic oxygen: Improvement of actinometry and comparison with laser spectroscopy" *J. Appl. Phys.*, vol. 88, p. 6232, 2000.
- [49] E. de la Cal, D. Tafalla, and F. L. Tabares, "Characterization of He/CH₄ dc glow discharge plasmas by optical emission spectroscopy, mass spectrometry, and actinometry" *J. Appl. Phys.*, vol. 73, no. 2, p. 948, 1993.
- [50] "National Institute of Standards and Technology Atomic Spectra Database" :
www.nist.gov
- [51] A. Le Gouil, E. Pargon, G. Cunge, O. Joubert, and B. Pelissier, "Chemical analysis of deposits formed on the reactor walls during silicon and metal gate etching processes" *J. Vac. Sci. Technol. B Microelectron. Nanom. Struct.*, vol. 24, no. 5, p. 2191, 2006.
- [52] S. Bouchoule, L. Vallier, G. Patriarche, T. Chevolleau, and C. Cardinaud, "Effect of Cl₂- and HBr-based inductively coupled plasma etching on InP surface composition analyzed using in situ x-ray photoelectron spectroscopy" *J. Vac. Sci. Technol. A Vacuum, Surfaces, Film.*, vol. 30, no. 3, p. 031301, 2012.
- [53] F. Cheng, "Design and Implementation of a Virtual Metrology System" in *IEEE Conference on Automation Science and Engineering*, 2005.

- [54] P. C. P. Chen, S. Wu, J. L. J. Lin, F. Ko, H. Lo, J. Wang, C. H. Yu, and M. S. Liang, "Virtual metrology: a solution for wafer to wafer advanced process control" *ISSM 2005, IEEE Int. Symp. Semicond. Manuf. 2005*, pp. 155–157, 2005.
- [55] T. Wünsche, M. Rudolph, and J. Zimpel, "Virtual Metrology to Measure Mass Loss at Deep Trench Processes Motivation to Measure the Mass Loss during the Deep Trench Etch Process" 2007. http://www.adp-dresden.de/papers/AECAPC_Europe_2007_Virtual Metrology.ppt
- [56] F. Y. Wang, "Virtual Metrology-A Solution for Wafer to Wafer Process Monitoring And Throughput Enhancement" pp. 1–12. *ISSM 2005, IEEE International Symposium on Semiconductor Manufacturing, 2005*
- [57] T. Lin, M. Hung, R. Lin, and F. Cheng, "A Virtual Metrology Scheme for Predicting CVD Thickness in" *IEEE Int. Conf. Robot. Autom.*, no. May, pp. 1054–1059, 2006.
- [58] E Ragnoli , N MacGearailt, Sean Mcclone, "EmanueleRagnoliIntelConference2009" in *Intel Ireland Research Conference, Dublin, Ireland, 2009*.
- [59] T. W. Kim and E. S. Aydil, "Effects of Chamber Wall Conditions on Cl Concentration and Si Etch Rate Uniformity in Plasma Etching Reactors" *J. Electrochem. Soc.*, vol. 150, no. 7, p. G418, 2003.
- [60] M. Kogelschatz, G. Cunge, N. Sadeghi, and O. Joubert, "Characterisation of layers deposited on reactor walls by plasma etching" *Contributions to Plasma Physics Conference 2004*.
- [61] G. Cunge, B. Pelissier, O. Joubert, R. Ramos, and C. Maurice, "New chamber walls conditioning and cleaning strategies to improve the stability of plasma processes" *Plasma Sources Sci. Technol.*, vol. 14, no. 3, pp. 599–609, Aug. 2005.
- [62] F. Bose, "Characterization of plasma etch processes using measurements of discharge impedance" *J. Vac. Sci. Technol. B Microelectron. Nanom. Struct.*, vol. 12, no. 4, p. 2805, Jul. 1994.
- [63] J. G. Langan, S. E. Beck, B. S. Felker, and S. W. Rynders, "The role of diluents in electronegative fluorinated gas discharges" *J. Appl. Phys.*, vol. 79, no. 8, p. 3886, 1996.
- [64] B. Andries, "Electrical characterization of radio-frequency parallel-plate capacitively coupled discharges" *J. Vac. Sci. Technol. A Vacuum, Surfaces, Film.*, vol. 7, no. 4, p. 2774, Jul. 1989.

- [65] E. At, “Detailed Investigations of the Sheath Dynamics and Elementary Processes in Capacitively Coupled RF Plasmas, PhD Thesis” University of Greifswald, 2009.
- [66] V. a. Godyak and N. Sternberg, “Dynamic model of the electrode sheaths in symmetrically driven rf discharges” *Phys. Rev. A*, vol. 42, no. 4, pp. 2299–2312, 1990.
- [67] M. Grapperhaus and M. Kushner, “A semianalytic radio frequency sheath model integrated into a two-dimensional hybrid model for plasma processing reactors” *J. Appl. Phys.*, vol. 81, no. January, pp. 569–577, 1997.
- [68] H. R. Koenig and L. I. Maissel, “Application of rf discharges to sputtering” *IBM J. Res. Dev.*, vol. 44, no. 1.2, pp. 106–110, Jan. 2000.
- [69] K. Köhler, J. W. Coburn, D. E. Horne, E. Kay, and J. H. Keller, “Plasma potentials of 13.56-MHz rf argon glow discharges in a planar system” *J. Appl. Phys.*, vol. 57, no. 1, p. 59, 1985.
- [70] Y. D. Lee and J. J. Oh, “Dynamic model and electrical characteristics for rf-biased electronegative plasma sheath” *IEEE Trans. Plasma Sci.*, vol. 30, no. 3, pp. 1320–1330, Jun. 2002.
- [71] M. Lieberman, “Analytical solution for capacitive RF sheath” *Plasma Sci. IEEE Trans.*, vol. 16, no. 6, pp. 638–644, 1988.
- [72] J. S. Logan, “Control of RF Sputtered Film Properties” *IBM J. Res. Dev.*, vol. 14, no. 2, p. 172, 1970.
- [73] M. a. Sobolewski, “Electrical optimization of plasma-enhanced chemical vapor deposition chamber cleaning plasmas” *J. Vac. Sci. Technol. B Microelectron. Nanom. Struct.*, vol. 16, no. 1, p. 173, Jan. 1998.
- [74] K. L. Steffens and M. a. Sobolewski, “Planar laser-induced fluorescence of CF₂ in O₂/CF₄ and O₂/C₂F₆ chamber-cleaning plasmas: Spatial uniformity and comparison to electrical measurements” *J. Vac. Sci. Technol. A Vacuum, Surfaces, Film.*, vol. 17, no. 2, p. 517, 1999.
- [75] M. Hopkinson, C. Jin, H. Liu, and R. Airey, “1.34 μm GaInNAs quantum well lasers with low room-temperature threshold current density” vol. 42, no. 1, pp. 0–1, 2006.
- [76] S. a. Lynn, N. MacGearailt, and J. V. Ringwood, “Real-time virtual metrology and control of etch rate in an industrial plasma chamber” *Proc. IEEE Int. Conf. Control Appl.*, pp. 1658–1663, 2012.

- [77] MacGearailt, “Opportunities for APC/AEC in 450mm and beyond” in *APC/AEC Europe*, 2012.
- [78] B. Keville, Y. Zhang, C. Gaman, A. M. Holohan, S. Daniels, and M. M. Turner, “Real-time control of electron density in a capacitively coupled plasma” *J. Vac. Sci. Technol. A Vacuum, Surfaces, Film.*, vol. 31, p. 031302, 2013.

Conference Proceeding and Journal Publications

Etch Rate Prediction using OES – A Virtual Metrology case study

E.Ragnoli, S.McLoone, J.Ringwood and N.Macgearailt

Proceedings of Intel European Research and Innovation Conference

2009.

Etch Rate Prediction using OES –A Virtual Metrology case study

E.Ragnoli, S.McLoone, N.Macgearailt

Technical Report Electronic Engineering Department NUI Maynooth,

June 2009.

Identifying key process characteristics and predicting Etch Rate from
High Dimensionality Datasets

E.Ragnoli, S.McLoone, J.Ringwood and N.Macgearailt

Proceedings of ASMC 2009.

Model Structure Improvement for Virtual Metrology in Plasma Etch

S.Lynn, J.Ringwood, N.Macgearailt, E.Ragnoli and S.McLoone

Proceedings of ASMC 2009.

Plasma diagnostics through five prominent oxygen triplets

V.Milosavljevic, E.Ragnoli, S.Daniels, N.Macgearailt, S.McLoone and

J.Ringwood in Proceedings of GEC 2008.

Comparison of NMF and Kernel NMF in applications to OES plasma
etching datasets

E.Ragnoli, S.McLoone, J.Ringwood and N.Macgearailt Proceedings of

Intel Innovation Forum 2008.

Virtual Metrology for Plasma Etching

S.Lynn, J.Ringwood, N.Macgearailt, E.Ragnoli and S.McLoone in
Proceedings of Intel Innovation Forum 2008.

Matrix Factorisation Techniques for Endpoint Detection in Plasma
Etching

E.Ragnoli, S.McLoone, J.Ringwood and N.Macgearailt in
Proceedings of Association of Semiconductor Manufacturing
Conference
2008.

**Improved fluid simulations of radio-frequency plasmas using energy
dependent ion mobilities**

Arthur Greb, Kari Niemi, Deborah O'Connell, Gerard J. Ennis, Niall
MacGearailt, Timo Gans
Physics of Plasmas 05/2013; 20(5). DOI:10.1063/1.4804280

**Phase-resolved optical emission spectroscopy for an electron
cyclotron resonance etcher**

Vladimir Milosavljevic, Niall MacGearailt, Stephen Daniels, Miles M.
Turner, P. J. Cullen

Journal of Applied Physics 04/2013; 113(16). DOI:10.1063/1.4802440

Real-time virtual metrology and control for plasma etch

Shane A. Lynn, Niall MacGearailt, John V. Ringwood

Journal of Process Control 04/2012; 22(4):666–676.

DOI:10.1016/j.jprocont.2012.01.012

Global and Local Virtual Metrology Models for a Plasma Etch Process

Shane A Lynn, John Ringwood, Niall Macgearailt

IEEE Transactions on Semiconductor Manufacturing . 01/2012; 25.

DOI:10.1109/TSM.2011.2176759

Gaussian process regression for virtual metrology of plasma etch.

Shane Lynn, John Ringwood, Niall MacGearailt

Department of Electronic Engineering, National University of Ireland,

Maynooth, Ireland

07/2010; DOI:10.1049/cp.2010.0485 In proceeding of: Signals and

Systems Conference (ISSC 2010), IET Irish

An analysis of noise on optical emission Spectroscopy measurements

Beibei Ma, Sean McLoone, John Ringwood, Niall MacGearailt
07/2010; DOI:10.1049/cp.2010.0510 In proceeding of: Signals and
Systems Conference

A role of low pressure plasma discharge on etch rate of SiO₂ dummy
wafer

Vladimir Milosavljevic, Andrijana Zekic, Dusan Popovic, Niall
Macgearailt, Stephen Daniels

American Physical Society, 62nd Annual Gaseous Electronics
Conference, October 20-23, 2009, abstract #URP.024

Selecting signature optical emission spectroscopy variables using sparse
principal component analysis

B. Ma, S. McLoone, J. Ringwood, N. Macgearailt

Dept. of Electron. Eng., Nat. Univ. of Ireland, Maynooth

01/2009; DOI:10.1109/ICCITECHN.2008.4803104 In proceeding of:
Computer and Information Technology, 2008. ICCIT 2008. 11th
International Conference on

Prediction of Vacuum Pump Degradation in Semiconductor Processing

Shane W Butler, John V Ringwood, Niall Macgearailt

Department of Electronic Engineering, National University of Ireland,

Maynooth, Ireland; * Intel Ireland, Leixlip, Co. Kildare, Ireland

V. Milosavljeviæ, E. Ragnoli, S. Daniels, N. Macgearailt, S. McLoone
and J. Ringwood, Plasma diagnostic through the five prominent oxygen
triplets, 61th Gaseous Electronics Conference, 14-OCT-08 - 17-OCT-08,
Dallas, Texas, USA

E. Ragnoli, V. Milosavljeviæ, S. Daniels, N. Macgearailt, S. McLoone
and J. Ringwood, Plasma diagnostic through the five prominent oxygen
triplets, 19th Annual IEEE/SEMI® Advanced Semiconductor
Manufacturing Conference, 05-MAY-08 - 07-MAY-08, Boston,
Massachusetts, USA

Frequency domain reflectometry of plasma chambers

V.J. Law, N. Macgearailt, P. Cunningham

Vacuum 03/2007; 81(8):958-968. DOI:10.1016/j.vacuum.2006.11.004

Visualization of a dual-frequency plasma etch process

V J Law, N Macgearailt

Measurement Science and Technology (Impact Factor: 1.44). 01/2007;

18(3):645. DOI:10.1088/0957-0233/18/3/014

Frequency domain reflectometry of Hitachi ECR plasma-tool

V.J. Law, N. Macgearailt

Electronics Letters (Impact Factor: 1.04). 02/2006;

DOI:10.1049/el:20063219

Source: IEEE Xplore

Impact of low pressure plasma discharge on etch rate of SiO₂ wafer

Dusan Popovic, Vladimir Milosavljevic, Andrijana Zekic, Niall

Macgearailt, Stephen Daniels

American Physical Society, 51st Annual Meeting of the APS Division of

Plasma Physics, November 2-6, 2009, abstract #NP8.037

The measurement and control of process variation in High Volume

Manufacturing semiconductor Fabs

12th EMEA Academic Forum, Budapest, Hungary-. MacGearailt. 2007.

The challenges of plasma processing in high volume factories - Invited

The 9th Technological Plasmas Workshop was held at the University of Manchester on 5–6 January 2012

Plasma Process Control in the Semiconductor Industry Invited

VACUUM SYMPOSIUM UK October 2012, Ricoh Arena Coventry

Challenges of plasma nano-fabrication in the semi-conductor industry

Invited

ICPIG 2011 Conference

Opportunities for APC/AEC in 450mm and beyond.

Semicon Europa 2012

APC/AEC Grenoble 2012

Metrology Aware Fault Detection And Process Diagnostics

APC Europe 2011